J. Nanoanalysis., 11(1): 616-635, Winter 2024

Synthesis of Resin-based Composites Containing Cellulose Nanocrystal and Nano-amorphous Calcium Phosphate for Orthodontic Adhesive Uses

Nasrin Shahmiri[1], Nahid Hassanzadeh Nemati[1]*, Ahmad Ramazani Saadatabadi[2], Massoud Seifi[3]

[1] *Department of Biomedical Engineering, Science and Research Branch, Islamic Azad University, Tehran, Iran.*
[2] *Department of Chemical & Petroleum Engineering, Sharif University of Technology, Tehran, Iran.*
[3] *Department of Orthodontics, School of Dentistry, Shahid Beheshti University of Medical Sciences, Tehran, Iran.*

ABSTRACT

ARTICLE INFO

Article History:

Received 2024-05-25
Accepted 2024-11-23
Published 2024-02-15

Keywords:

composite resin,
orthodontic bonding,
white spot lesion,
cellulose nanocrystal,
amorphous calcium phosphate.

White spot lesions (WSLs) commonly develop around orthodontic brackets. Amorphous calcium phosphate (ACP) is known for its remineralizing properties, which can help prevent WSLs. However, the incorporation of ACP may compromise the mechanical strength of the material. This study focuses on the development of experimental orthodontic adhesives incorporating cellulose nanocrystal (CNC) and amorphous calcium phosphate (ACP) to evaluate their bond strength and mineral release properties. The experimental resin formulation included BisEMA, TEGDMA, 4-META, camphorquinone, and DMAEM. Adhesive disks underwent characterization through FE-SEM, EDS, and XRD techniques. The release of minerals was quantified using ICP-OES. The shear bond strength (SBS) was evaluated immediately after bonding metal brackets to bovine incisors. Adhesives containing various fractions of ACP (15%, 20%, and 40%) exhibited sustained release of calcium and phosphorus over a 30-day period. The incorporation of ACP and CNC contributed to a reduction in adhesive cytotoxicity. The adhesive formulation with 40% ACP + 5% CNC showed the lowest SBS, whereas the adhesive with 15% ACP + 5% CNC demonstrated suitable bond strength for orthodontic applications. Addition of 20% CNC to the experimental resin positively impacted bracket bond strength. Likewise, 20% ACP improved shear bond strength. However, the combination of 5% CNC with ACP did not significantly affect bond strength. ACP nanoparticles show promise for integration into experimental orthodontic adhesives containing BisEMA, TEGDMA, 4-META, CQ, and DMAEM. The synergistic use of ACP with CNC remains a topic of debate and warrants further investigation.

How to cite this article
Shahmiri N., Hassanzadeh Nemati N., Ramazani Saadatabadi A., Seifi M., Synthesis of Resin-based Composites Containing Cellulose Nanocrystal and Nano-amorphous Calcium Phosphate for Orthodontic Adhesive Uses. J. Nanoanalysis., 2024; 11(1): 616-635.

*Corresponding Author Email: *nahid_hasanzadeh@yahoo.com*

INTRODUCTION

Tooth enamel, which is composed of long apatite crystals [1], can experience demineralization around orthodontic brackets, leading to the formation of white spot lesions (WSLs) [2]. WSLs are frequently observed in orthodontic patients [3]. To mitigate the risk of WSLs, researchers are exploring the use of remineralizing agents [4]. One approach involves enriching orthodontic adhesive with nanoparticles that contain minerals like calcium (Ca), phosphorus (P), and fluoride (F). These nanoparticles have the potential to inhibit tooth demineralization and promote remineralization, effectively preventing the occurrence of WSLs [5-8].

Polymer-ceramic composites are widely utilized as biomaterials for the repair of bone and tooth defects [9-11]. These versatile materials find applications in dental implants, dental composites, and orthodontic adhesives [12-14]. Specifically, resin-based composites are commonly employed in orthodontic treatments [15]. The incorporation of calcium phosphate into composite structures imparts bioactivity to these materials [16]. While previous studies have predominantly focused on the use of crystalline forms of calcium phosphates in dental applications [17], there has been a shift towards exploring the potential of Amorphous Calcium Phosphate (ACP) in dental resins [18-20]. As a result, several toothpastes based on ACP have been introduced to the market [17]. The dental composites containing small amounts of ACPs have the ability to release significant quantities of Ca and P due to the large surface area of ACPs. This characteristic allows for more fillers to be incorporated into the resin, thus reinforcing its structure [19]. However, it should be noted that an excessive amount of ACP in the adhesive can lead to a reduction in bond strength [7, 8]. For instance, Zhang et al. [7] successfully developed an orthodontic cement by incorporating 40% ACP, which not only exhibited sufficient ion release but also demonstrated adequate shear bond strength (SBS) for orthodontic applications. Their formulation consisted of nano-sized ACP mixed with a resin matrix comprising HEMA, BisGMA, and PMGDM-EBPADMA [7]. However, it is important to note that the use of HEMA as a monomer in dental resins can lead to a weakening of the polymer mechanical properties since HEMA cannot form cross-links [21]. Additionally, HEMA has been found to increase toxicity due to the metabolization of methacrylic acid [22]. The safety of Bis-GMA is also a subject of controversy due to the release of bisphenol-A [23], and these systems are prone to hydrolytic and enzymatic degradation, which can further reduce the strength of bracket bonds [17]. To address these concerns, other monomers such as Bis-EMA (which has a low viscosity), TEGDMA (which exhibits high water sorption properties), and DMAEM (which offers better biocompatibility) can be utilized in dental resins [24]. For example, Aleesa et al. [6] synthesized an orthodontic adhesive containing BisEMA, TEGDMA, DMAEM, Camphorquinone, 4-META, and bioactive glass, which demonstrated long-term release of fluoride, calcium, and phosphate ions while maintaining a satisfactory bracket bond [6]. It should be noted that the resin matrix composition of orthodontic adhesives plays a crucial role in bracket bond strength [7], necessitating the selection of appropriate monomers.

Studies have indicated that orthodontic adhesives containing ACP nanoparticles can achieve acceptable bracket bonding [7, 8, 25]. However, other studies have reported that orthodontic adhesives incorporating ACP exhibit lower bond strength compared to conventional adhesives [14, 26, 27]. The aggregation of ACP particles may contribute to the reduction in mechanical properties of the composite [27, 28]. It has been observed that the inclusion of more than 40% ACP in the adhesive leads to minimal bond strength despite maximum ion release [8]. To overcome this challenge, the combination of ACP with reinforcing fillers can help optimize the bracket bond without sacrificing ion release. In previous studies, barium boroaluminosilicate glass particles measuring 1.4 µm have been used as reinforcing agents in tandem with ACP [8, 18, 19]. Another potential reinforcing agent is cellulose nanocrystals (CNCs), which are needle- shaped nanoparticles known for their high modulus of elasticity and dimensional stability. The longitudinal tensile modulus of CNCs (145 GPa) exceeds that of Kevlar (130 GPa), suggesting that CNCs have the potential to enhance the mechanical performance of the composite material [29-31]. Wang et al. [32] have reported that CNC/ZnO nanohybrids influence the mechanical properties of dental resin composites. However, more research is needed to fully understand the impact of CNC on the physical characteristics of dental resins [33].

Cellulose/calcium phosphate hybrids have been identified as potential materials for dental repair [34]. Recent advancements in nanotechnology offer new possibilities for eradicating WSLs. One promising approach involves incorporating nanoparticles into adhesives to facilitate the regeneration of tooth enamel [35]. However, it is crucial to develop an orthodontic adhesive that can release mineralizing ions while maintaining sufficient bond strength. Limited research exists on the use of CNC in dental adhesives or the combination of ACP and CNC. In this study, experimental orthodontic adhesives were formulated with ACP as a bioactive filler and CNC as a reinforcing filler to investigate the release of minerals and the bond strength of the bracket. The study aimed to test the following hypotheses: (1) The presence of CNCs influences the bond strength of the experimental adhesive. (2) The presence of ACPs influences the bond strength of the experimental adhesive. (3) The combination of ACPs and CNCs influences the bond strength of the experimental adhesive. (4) The experimental adhesive containing ACP releases Ca and P. (5) The experimental adhesive, which includes ACP with CNC, releases Ca and P.

EXPERIMENTAL

Preparation of the fillers

CNC was synthesized using the acid hydrolysis method as outlined in previous works [36, 37]. The process involved grinding Whatman filter paper and subjecting it to hydrolysis with sulfuric acid. Cold water was used to halt the hydrolysis reaction, followed by removal of the supernatant from the settled solution. The resulting white slurry underwent centrifugation and dialysis. The CNC suspension was sonicated, filtered, and then stored at 4 °C. Prior to freeze-drying, the suspension underwent additional rounds of sonication and filtration. Initially, the suspension was frozen at –80 °C for 24 hours and subsequently dried for 72 hours. The resulting CNC powder was characterized using DLS, AFM, and FE-SEM techniques. Amorphous calcium phosphate (ACP) nanoparticles with a particle size below 150 nm (BET) were procured from Sigma-Aldrich and utilized without further modification.

Preparation of the resin

The resin was prepared utilizing specific monomers detailed in Table 1, based on previous studies [6, 38]. All monomers, sourced from Sigma-Aldrich, were directly used as received. The monomers were accurately weighed and transferred into an aluminum foil-wrapped bottle. A magnetic stirrer was employed to mix all components for 30 minutes at room temperature to ensure a homogeneous blend. The light-sensitive mixture was shielded from light exposure.

Production and characterization of the adhesive disks

The adhesive disks were fabricated following previous studies [6, 38]. The resin and fillers (ACP, CNC) were manually mixed using a spatula. This adhesive mixture was filled into a metal mold measuring 10 mm in diameter and 1 mm in thickness. Acetate films were positioned above and below the mold, sandwiched between two glass slides. Gravity and pressure were utilized, with 200g weights placed on the glass slides to facilitate the escape of air bubbles and excess adhesive. Each side of the assembly was then cured with an LED light source (GuilinWoodpecker Medical Instrument, LED.D) for 20 seconds per side (40 seconds total). The adhesives were formulated based on previous studies [6, 8, 18-20, 39], yielding the following compositions:

R1: resin (control)
R2: resin + 20% CNC
R3: resin + 15% ACP + 5% CNC
R4: resin + 20% ACP
R5: resin + 40% ACP + 5% CNC

Orthodontic adhesive disks were prepared (Fig. 1), with R1 representing an unfilled resin, designated as the control group. The adhesive disks were characterized using FE-SEM, EDS, and XRD.

Table 1 Methacrylate monomers and the polymerization-initiating components in the experimental resin based on previous studies [6, 38]

Resin Component	Chemical name	Acronym	Content (mass%)
Base monomer	Ethoxylated bisphenol A glycol dimethacrylate	Bis-EMA	42.25
Diluent monomer	Triethylene glycol dimethacrylate	TEGDMA	55
Adhesion promoter monomer	4-methacryloxyethyl trimellitate anhydride	4-META	2
Light cure initiator monomer	Camphorquinone	CQ	0.5
Co-initator & accelerator monomer	Dimethylamino ethyl methacrylate	DMAEM	0.25

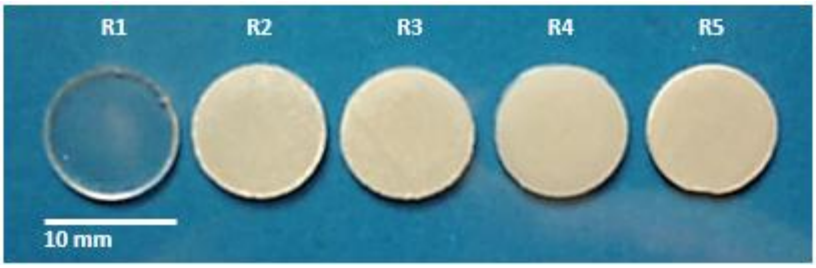

Fig. 1 Experimental adhesive disks: R1 (unfilled resin), R2 (20% CNC), R3 (15% CNC+ 5%ACP), R4 (20% ACP), R5 (40% ACP+5% CNC)

Measurement of Ca and P release

Following a previous study [40], seven disks were prepared for each experimental group. Disks were immersed in 11 ml deionized water within centrifuge tubes, and stored at 37 °C, as described in previous studies [6, 41-43]. The tubes were sealed, and after 30 days, the release of Ca and P was quantified via inductively coupled plasma optical emission spectroscopy (ICP-OES, Spectro, ARCOS).

Cytotoxicity test

Human gingival fibroblast cells (HGF, CELL No. IBRC C10459) were sourced from the Iranian Biological Resource Center and cultured following previous protocols [44-46]. These cells were maintained in Dulbecco's Modified Eagle Medium (DMEM) and cultivated in a standard incubator. In line with previous methodologies [45, 47], one composite disk measuring 10 mm in diameter and 1 mm in height were fabricated for each experimental group. The top and bottom surfaces of the disks were cured for 20 seconds, followed by UV sterilization of each side of the disks for 30 minutes (totaling 1 hour). Disks were eluted in a culture medium with a surface/volume ratio of 1.25 cm^2/mL [45, 46, 48]. The eluates were incubated for 24 hours, after which the disks were removed, and the extracts were filtered for MTT assay. HGF cells were seeded at a concentration of 1×10^4 cells/mL in a microplate and cultured in the incubator. Subsequently, the cell cultures were exposed to the composite extract, and cytotoxicity levels were evaluated after 24 hours. The MTT solution was introduced into the culture plate, and the cells were incubated. After discarding the supernatant, the formazan crystals were dissolved, and the optical density (OD) was measured at 570 nm. Cell viability was calculated using the formula: (OD of test group / OD of control cells) × 100 [49]. The cytotoxicity outcomes were categorized as severe (≤30%), moderate (30–60%), mild (60–90%), and non-cytotoxic (>90%) based on established criteria [44, 46, 50-52].

Shear bond strength (SBS) and adhesive remnant index (ARI)

Fifty bovine incisors, sourced from a local slaughterhouse (East Livestock Industrial Slaughterhouse, Sari, Iran), were utilized in the study (Fig. 2a). The teeth underwent de-tissueing to remove soft tissues (Fig. 2b) before being embedded in cold-cure acrylic (Acropars Cold-Cure Acrylic, Iran) (Fig. 2c). Based on previous studies [53], ten teeth were assigned to each group for testing different adhesives. Mandibular incisor orthodontic brackets were affixed to the teeth, with all bonding procedures performed by a single operator. The teeth were initially polished using aluminum oxide paste (Dentonext, Iran) and etched with 37% phosphoric acid gel (Condac 37 - FGM, Brazil). A thin layer of adhesive was applied to the mesh of the stainless-steel bracket (IMD, China), which was then positioned near the center of tooth. The adhesive was light-cured for 10 seconds on each side (total of 40 seconds) and immediately subjected to shear force testing using a Universal Testing Machine (Koopa TB-5T, Iran) (Fig. 3) at a crosshead rate of 0.5 mm/min. The maximum force required for bracket detachment was recorded in Newton and converted to MPa [54]. Post-debonding, each tooth was analyzed under a stereomicroscope (Dewinter Technologies) to assess the Adhesive Remnant Index (ARI) based on established criteria [55, 56], specifically:

0: no residual resin on the tooth
1: < 50% resin remaining on the tooth
2: ≥ 50% resin remaining on the tooth
3: 100% resin remaining on the tooth

Statistical analysis

Data analysis was conducted utilizing IBM SPSS Statistics 20 software. Group comparisons were performed using the Kruskal-Wallis test, while pairwise comparisons were assessed using the Mann-Whitney U test [53]. The difference was considered significant when $P \leq 0.05$.

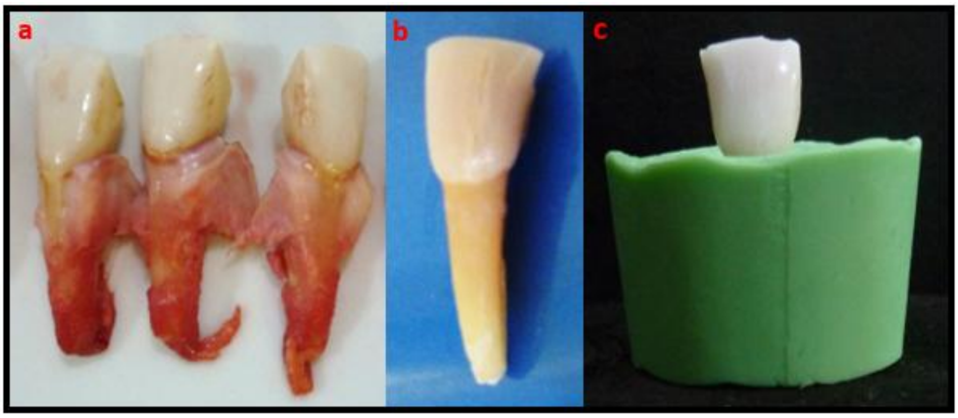

Fig. 2 Preparation of bovine teeth: a) Extraction of mandibular incisors, b) Removal of soft tissue, c) Embedding tooth in cold-cure acrylic

Fig. 3 Placement of tooth for shear bond strength test

RESULTS AND DISCUSSIONS

Characterization of the CNCs

The CNC powder underwent characterization using DLS, AFM, and FE-SEM techniques. The average length of the CNCs was found to be 105.06 ± 7.38 nm based on DLS analysis (Fig. 4).

The morphology of the CNC powder was visualized in Fig. 5a, showing the presence of CNCs. The AFM image in Fig. 5b confirmed the needle-like shape of the CNCs. The FE-SEM image at 500x magnification (Fig. 6a) revealed the flake-like structure of the CNC powder. At a higher magnification of 50000x, the typical rod and needle shapes of the CNCs were observed, providing evidence for successful CNC synthesis (Fig. 6b).

Characterization of the adhesive disks

The FE-SEM image of disk R1 (unfilled resin) is presented in Fig. 7. It also displays the presence of needle-shaped CNCs in the composite as evidenced by the image of disk R2 (20% CNC). Disks R3, R4, and R5 containing nano-ACP showed the presence of spherical ACP nanoparticles, although they were observed to be agglomerated within the matrix (Fig. 7). Elemental composition analysis of disk R1 using EDS revealed the highest amounts of carbon

and nitrogen. This is attributed to the absence of fillers in disk R1, which consisted solely of resin monomers (Table 2). Disk R5 (40% ACP + 5% CNC) had the highest filler content, and EDS analysis confirmed the elevated levels of calcium and phosphorus in this disk (Table 2). Disk R2 (20% CNC) exhibited the highest amount of oxygen due to the presence of CNCs, which are rich in oxygen (Table 2). Comparatively, disk R4 (20% ACP) contained higher amounts of calcium and phosphorus than disk R3 (15% ACP + 5% CNC) (Table 2). These EDS findings validate the elemental composition consistency of the adhesive disks with their primary theoretical formulation.

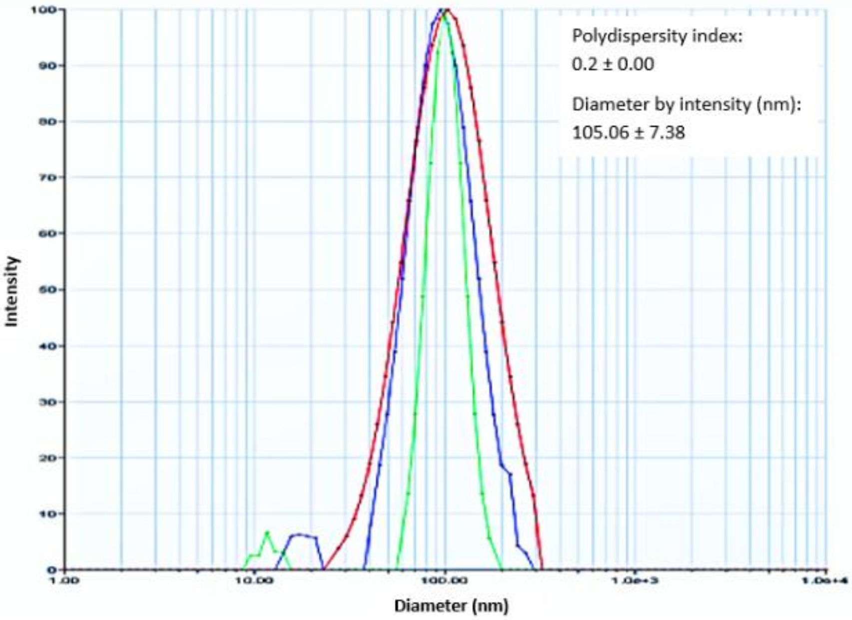

Fig. 4 Size distribution of CNCs obtained from DLS; (Red: first run, Green: second run, Blue: third run)

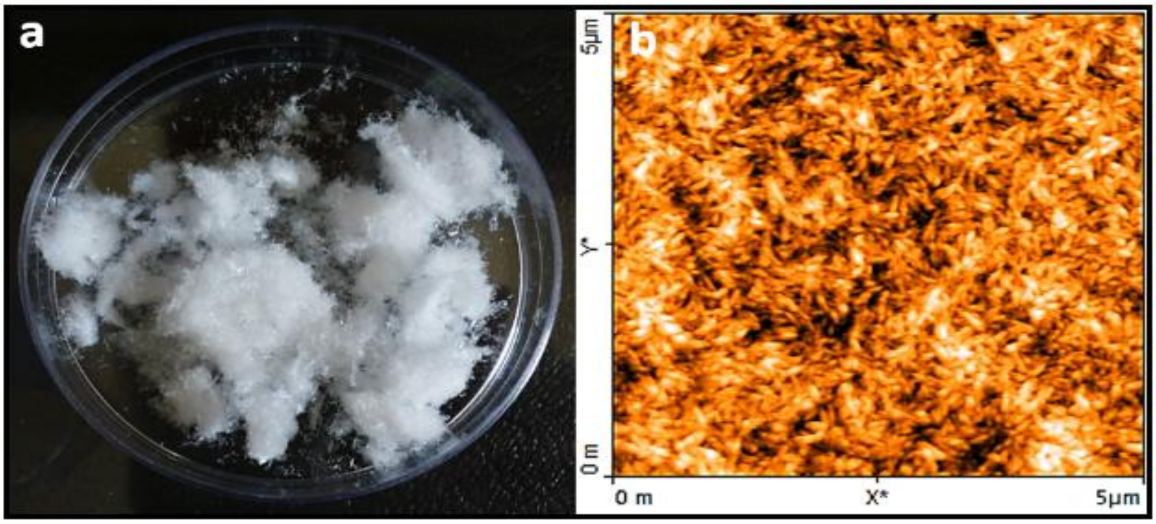

Fig. 5 a) Dry powder of CNC, b) Corresponding AFM image

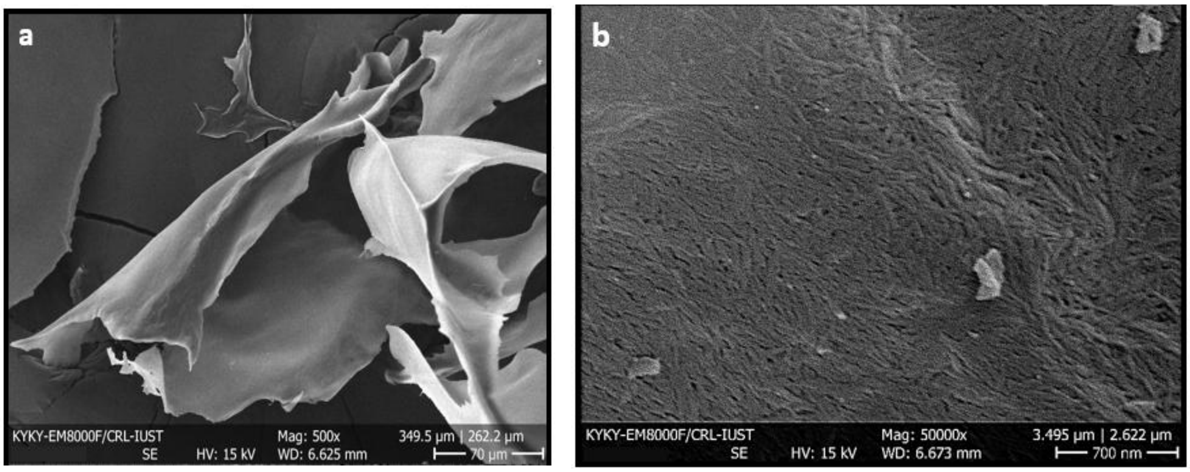

Fig. 6 FE-SEM image of CNC powder: a) 500x magnification, b) 50000x magnification

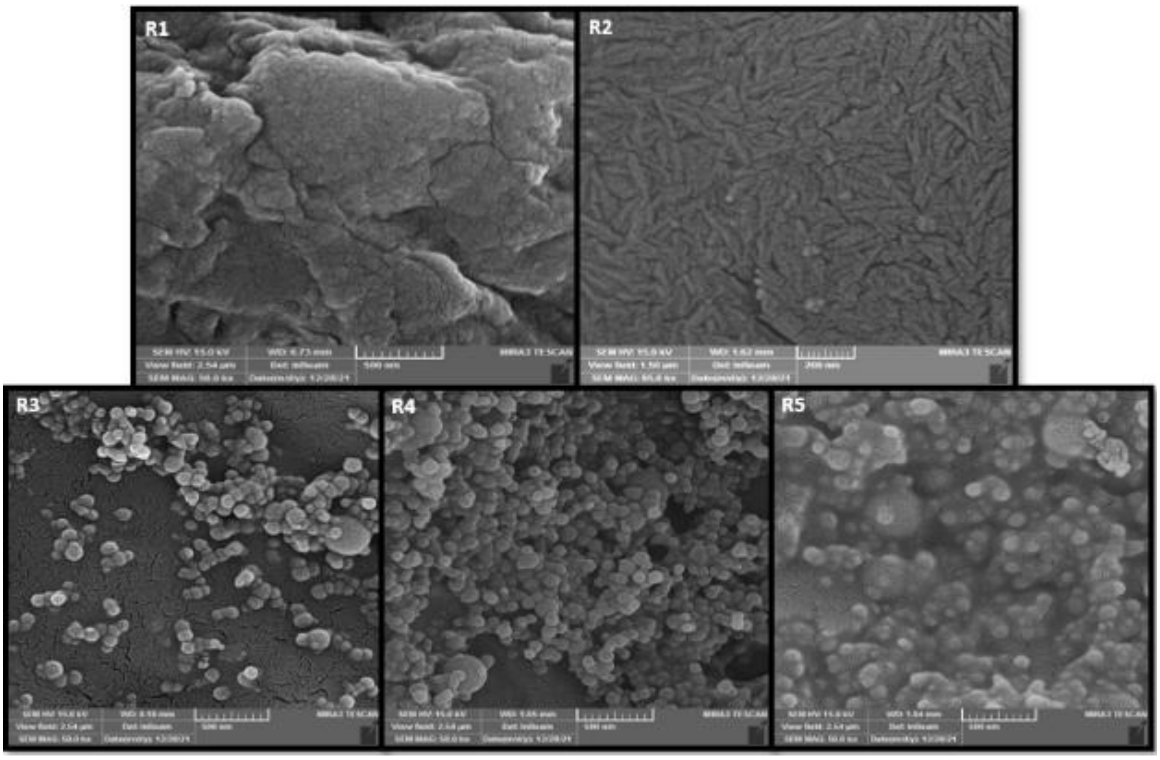

Fig. 7 FE-SEM images of the adhesive disks: R1 (unfilled resin), R2 (20% CNC), R3 (15% CNC + 5% ACP), R4 (20% ACP), R5 (40% ACP + 5% CNC)

Table 2 The elements of the adhesive disks based on EDS analysis
Wt: weight, AT: atomic, R1 (unfilled resin), R2 (20% CNC), R3 (15% CNC + 5% ACP), R4 (20% ACP), R5 (40% ACP + 5% CNC)

Elements	C		O		N		Ca		P	
	Wt%	AT%	Wt%	AT%	Wt%	AT%	Wt%	AT%	Wt%	AT%
R1	62.81	68.92	33.37	27.49	3.82	3.59	-	-	-	-
R2	56.12	63.10	43.57	36.78	-	-	-	-	-	-
R3	54.83	62.49	40.75	34.86	1.57	1.54	1.45	0.49	1.33	0.59
R4	51.85	60.13	41.81	36.40	1.57	1.56	2.36	0.82	2.33	1.05
R5	35.30	47.01	41.70	41.70	1.26	1.44	11.74	4.68	9.82	5.07

The XRD analysis of the disks is presented in Figure 8. The scans were conducted within the 2ϴ range of approximately 10-90°. In the XRD pattern of disk R1, two humps can be observed in the 2ϴ range of about 10-50°, indicating the presence of the amorphous phase of the resin [57] (Fig. 8). These humps are also visible in the other four disks, albeit with lower intensity. Disk R2 (20% CNC) exhibits a prominent crystalline peak at 2ϴ=22.68°, along with smaller peaks at 2ϴ=14.75° and 2ϴ=16.71°, confirming the presence of CNC based on previous studies [58, 59] (Fig. 8). The XRD pattern of ACP is characterized by two broad humps in the 2ϴ range of 20° to 60° [60-62]. In this context, a hump is somewhat visible in disk R3 (15% ACP + 5% CNC) within the 2ϴ range of approximately 25-35°, and with lower intensity in disks R4 (20% ACP) and R5 (40% ACP + 5% CNC), indicating the presence of ACP. The peak at 2ϴ=22.91° in the pattern of disk R3 confirms the presence of CNC. Likewise, the peak at 2ϴ= 22.60° confirms the presence of CNC in disk R5. The patterns of disks R3, R4, and R5 exhibit two crystalline peaks at approximately 2ϴ=26° and 3 2ϴ=40°, which may be attributed to the crystallization of ACP particles. Premature crystallization poses a significant challenge in handling ACP particles, as studies have shown that ACP powder can transform into crystalline hydroxyapatite within a few hours at room temperature [63, 64]. ACP tends to crystallize rapidly under both wet and dry conditions [63, 65]. However, the XRD patterns of disks R3, R4, and R5 do not align with crystalline phases such as apatite or octacalcium phosphate, suggesting that the ACP particles were not fully crystallized. Overall, the XRD patterns (Fig. 8) are consistent with the components of the adhesive disks.

Mineral release

The adhesive disks were evaluated for the release of Ca and P following a 30-day immersion period (Fig. 9). Disk R5 (40% ACP + 5% CNC) demonstrated the highest Ca and P release compared to Disk R3 (15% ACP + 5% CNC) and Disk R4 (20% ACP), with statistically significant differences (P = 0.002). Moreover, Disk R4 exhibited a greater Ca release than Disk R3, with a significant difference (P = 0.048). Similarly, the P release from Disk R4 surpassed that of Disk R3, with a statistically significant difference (P = 0.035) (Fig. 9).

Adhesive R5 (40% ACP + 5% CNC) demonstrated higher calcium (Ca) and phosphorus (P) release when compared to R3 (15% ACP + 5% CNC) and R4 (20% ACP) (Fig. 9), a finding consistent with previous studies [7, 8, 17, 20]. Skrtic et al. [66] highlighted the critical role of filler quantity in determining ion release capacity, noting a significant increase in Ca and P release at specific ACP content thresholds (0.37 to 0.40) [66]. In this study, there was a sharp escalation in Ca and P release as ACP content rose from 0.15 to 0.40 (Fig. 9). Higher ACP content in adhesives promotes water and ion diffusion by enhancing interface availability [8]. The nano-sized ACPs, with their extensive surface area and strong water affinity, facilitate rapid mineral release [7, 17, 19]. ACP content exceeding 40% was deemed impractical in this study as it resulted in overly dry adhesives. While the Ca and P release from adhesives R3 (15% ACP + 5% CNC) and R4 (20% ACP) did not exhibit significant levels, it provides valuable insights into mineral release from the experimental resin. Aleesa et al. [38] highlighted that a composite containing bioactive glass in a neutral solution has a subdued reaction but can induce apatite precipitation in Ca and PO_4 ion-enriched solutions. Given that disk R5 (40% ACP + 5% CNC) released the highest levels of Ca and P (Fig. 9), it holds promise for apatite formation in neutral solutions. ACPs are known to transition from volatile states to crystalline CaPs in solutions, suggesting potential tooth mineral regeneration through ACP composites [17, 67]. Therefore, the mineral loss of teeth can be regenerated by the use of ACP composites [68, 69]. It is postulated that ACP/CNC particle distribution was uneven in this study. During the water absorption and ion release process, the filler-resin matrix interfaces were subject to unpredictable spatial variations [70].

In this study, triethylene glycol dimethacrylate (TEGDMA) was introduced into the resin to regulate viscosity, boasting a degree of hydrophilicity leading to water absorption. On the other hand, ethoxylated bisphenol A glycol dimethacrylate (Bis-EMA) exhibited lower viscosity and hydrophilicity [71, 72]. Polymerization was initiated using a free radical mechanism involving camphoroquinone (CQ), with an accelerator like dimethylaminoethyl methacrylate (DMAEM) included [73-75]. The ion release kinetics from the adhesive disks (R3-R5) were chiefly influenced by the TEGDMA monomer content, as its hydrophilic nature aids water absorption, ion diffusion, and potentially internal mineral saturation [17, 22, 73-75]. Moreover, the experimental adhesives featured 4-methacryloxyethyl trimellitate anhydride (4-META), which may enhance the composite-to-tooth bond by acting as a chelator of calcium ions and improving enamel surface wetting [76, 77], potentially impacting calcium release.

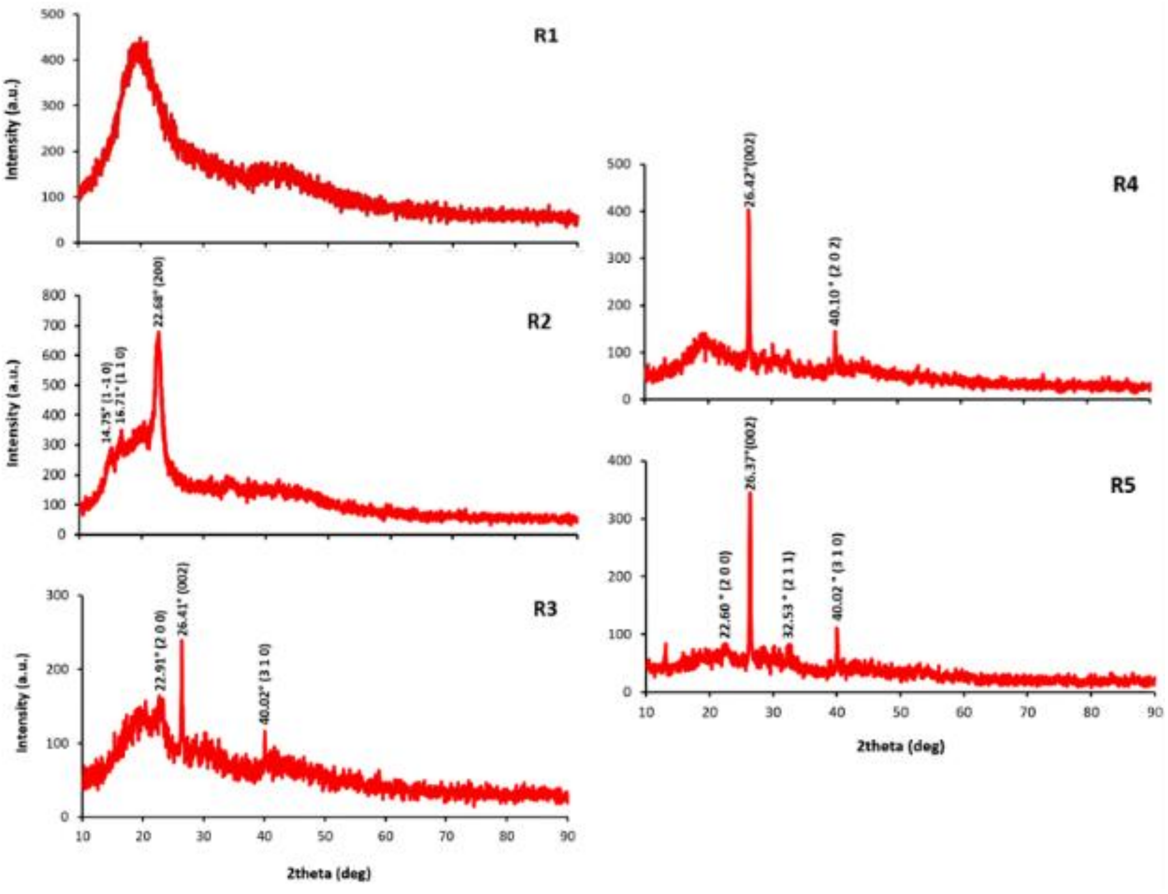

Fig. 8 XRD patterns of the adhesive disks: R1 (unfilled resin), R2 (20% CNC), R3 (15% CNC + 5%ACP), R4 (20% ACP), R5 (40% ACP + 5% CNC)

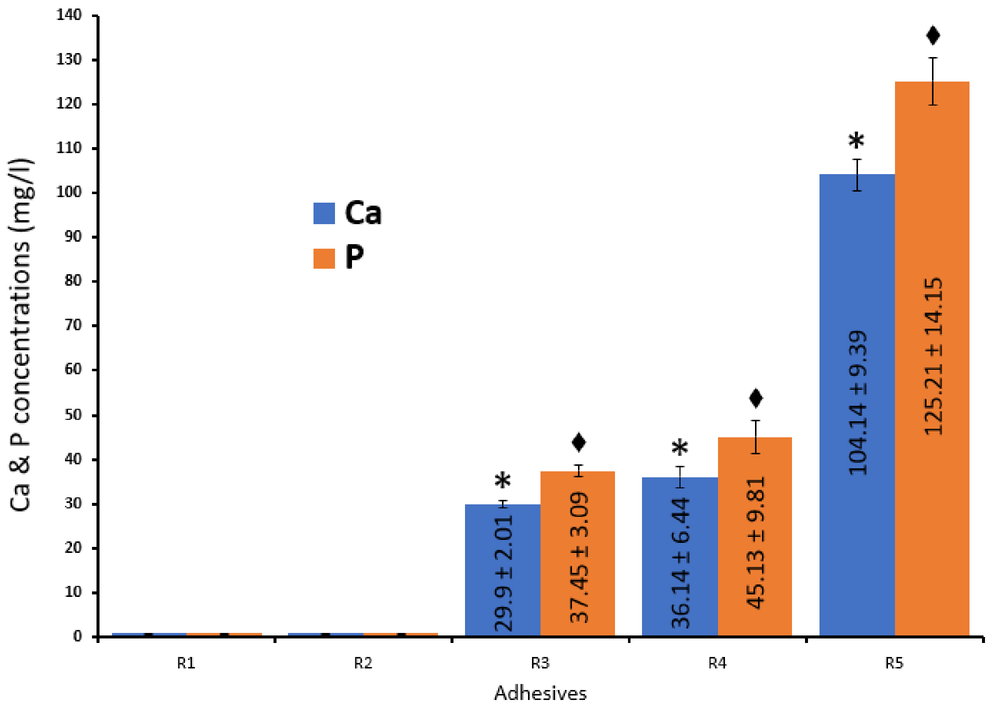

Fig. 9 Average Ca and P release (Mean ± SD) from adhesive disks after 30 days. Symbols (*♦) indicate pairwise significant differences between groups ($P < 0.05$). R1 (unfilled resin), R2 (20% CNC), R3 (15% CNC + 5% ACP), R4 (20% ACP), R5 (40% ACP + 5% CNC)

Cell viability

Cell viability was lower for all adhesive disks in contrast to the pure medium, with statistical significance ($P = 0.05$), except for disk R4 (20% ACP) (Fig. 10). This suggests that disk R4 displayed superior biocompatibility among the adhesive disks. Notably, the cell viability post-exposure to disk R1 (unfilled resin) was 61.3 ± 0.8%, indicating mild toxicity. In comparison, adhesive R2 (20% CNC) demonstrated a cell viability of 86.9%, signaling low toxicity attributed to cellulose nanocrystals (Fig. 10).

In Fig. 11, the appearance of HGF cells post-exposure to the composite extracts is depicted. Mediums R1 (unfilled resin) and R2 (20% CNC) showcased more cells with spherical shapes, implying a distinct cellular response compared to mediums R3 (15%ACP+5%CNC), R4 (20%ACP), and R5 (40%ACP+5%CNC), where cells exhibited predominantly polygonal and spread shapes similar to those in the pure medium (Fig. 11a). The presence of polygonal and spread cell shapes in mediums R3, R4, and R5 signifies the biocompatibility of ACP nanoparticles, as evidenced by cellular morphology akin to that of healthy cells. The microscopic observations align with the Elisa reader outcomes (Fig. 10 & 11). To mitigate toxicity, nanoparticles were incorporated into the resin, although further research is warranted to confirm the safety of cellulose nanocrystals (CNC) for clinical applications. Menezes-Silva et al. [78] successfully enhanced the biocompatibility of commercial glass ionomer cement (GIC) by incorporating CNC.

SBS & ARI assessment

Significant differences were observed in the mean SBS of the control adhesive (R1: unfilled resin) compared to other experimental groups ($P < 0.05$) (Fig. 12), suggesting diverse adhesive performances. No substantial difference was noted in the bond strength between adhesive R2 (20% CNC) and R3 (15% ACP + 5% CNC) ($P = 0.199$) (Fig. 12). While the mean SBS of adhesive R4 (20% ACP) exceeded that of R2 (20% CNC), the distinction was not statistically significant

(*P*= 0.096) (Fig. 12). Adhesive R5 (40% ACP + 5% CNC) demonstrated the lowest SBS among the groups, with a statistically significant difference ($P < 0.01$), indicative of a weaker bond when compared to other formulations.

In terms of bonding strength, the composite resin displayed a range of 2 to 13 MPa with metal brackets in previous studies [79]. Adhesive R1 (pure resin) demonstrated a reasonably strong bond strength of approximately 10 MPa, indicating that Bis-EMA and TEGDMA in combination form a robust bond with enamel (Fig. 12). The mechanical functionality of adhesives R3 (15% ACP + 5% CNC), R4 (20% ACP), and R5 (40% ACP + 5% CNC) containing ACP is predominantly influenced by the irregular distribution of ACP clusters rather than the composition of the resin [17, 80]. Skrtic et al. [70] integrated Zr-ACP particles into dental resin, with a median particle diameter of 8.6 ± 2.4 µm. They suggested that reducing the size of ACP particles enhances the interaction between ACP and resin, thereby improving the mechanical strength of the composite [70]. In this study, nano-sized ACP particles (<150 nm) were utilized, potentially impacting the shear bond strength (Fig. 12). Furthermore, Skrtic et al. [66] noted that amorphous calcium phosphate could weaken the filled polymer compared to the unfilled polymer. The inherent aggregation of ACP particles weakens ACP/resin interactions, leading to the destabilization of the filler/polymer interface and reduced mechanical strength [17, 27, 62], limiting the use of ACP-based composites to non-stress-bearing applications like fissure sealants [14, 17, 69, 80]. Unexpectedly, adhesives R3 (15% ACP + 5% CNC) and R4 (20% ACP) exhibited higher shear bond strength than the unfilled resin (R1) in this study (Fig. 12). This enhanced strength in adhesives R3 and R4 (Fig. 12) can be attributed to the incorporation of nano-sized ACP and CNC. Nano-ACPs offer a larger surface area, providing more room within the polymer matrix for incorporating reinforcing fillers and enhancing mechanical properties [8]. However, adhesive R5 (40% ACP & 5% CNC) displayed an SBS of approximately 6 MPa, the minimum acceptable bond strength that could result in premature bracket debonding during treatment [8] (Fig. 12). It is hypothesized that the heterogeneous ACP/CNC fillers could not establish a close interlocking network with the experimental resin. Optimal CNC content within the resin can create a permeated network, as seen with the incorporation of 20% CNC (R2), yielding a suitable shear bond strength (Fig. 12). Past research has demonstrated that CNC can effectively enhance the mechanical properties of dental resins [32, 81]. Sabir et al. [81] successfully enhanced the mechanical properties of dental adhesive by incorporating CNC. Likewise, Moradian et al. [82] discovered that incorporating bacterial CNC into resin-modified glass ionomer cement (RMGICs) can improve shear bond strength properties.

There were no substantial differences in ARI values between the control adhesive (R1) and the other experimental groups ($P > 0.05$) (Fig. 13), suggesting similar patterns of adhesive residue distribution post-bond failure.

The performance of composites is influenced by the type of filler, filler quantity, and resin composition [83]. An effective adhesive must not only endure the functional stresses in the oral cavity but also safeguard oral tissues from damage [84]. The high Adhesive Remnant Index (ARI) scores observed in this study (Fig. 13) could impact the enamel post-orthodontic treatment. A higher amount of adhesive remnant necessitates additional enamel polishing to eliminate the adhesive residue after bracket debonding [85]. Nonetheless, there is conflicting information in the literature regarding ARI scores. A greater presence of adhesive remnants on the enamel suggests bracket debonding occurs at the bracket/adhesive interface, preventing enamel chipping and fracturing [85-88]. In our investigation, the elevated ARI scores across all adhesives correlated with increased bond strength, with the exception of adhesive R5 (Fig. 12 & 13). A high ARI score (2 & 3), indicative of greater bond strength, could be advantageous in orthodontic applications [85, 88, 89].

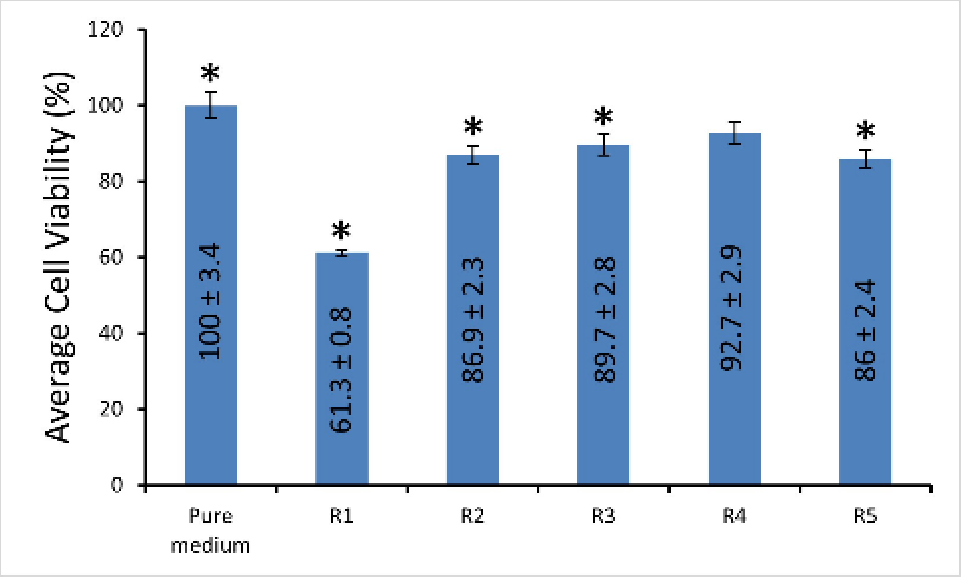

Fig. 10 Results of MTT assay after 24 h. Symbol (*) denotes significant differences between pure medium (untreated cells) and adhesive disks ($P = 0.05$). R1 (unfilled resin), R2 (20% CNC), R3 (15% CNC + 5% ACP), R4 (20% ACP), R5 (40% ACP + 5% CNC)

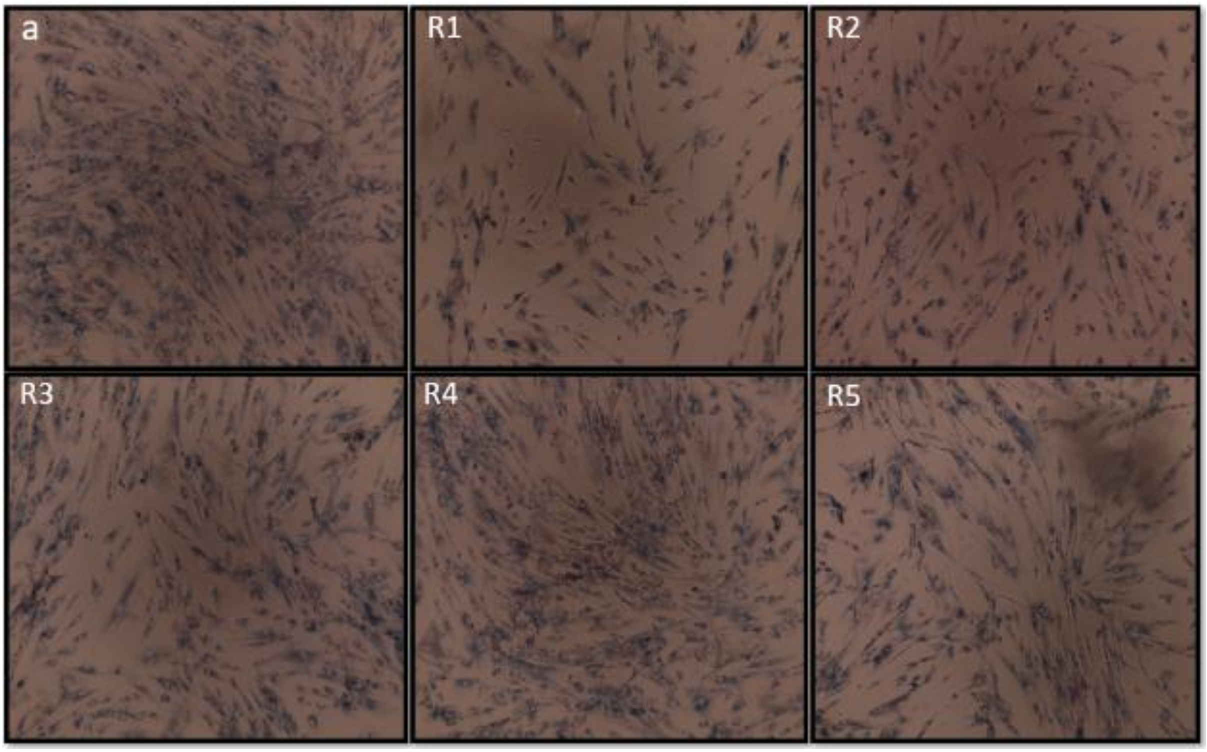

Fig. 11 Optical micrographs of HGF cells post exposure to extracts from adhesive disks. a) Pure medium (untreated cells), R1 (unfilled resin), R2 (20% CNC), R3 (15% CNC + 5% ACP), R4 (20% ACP), R5 (40% ACP + 5% CNC)

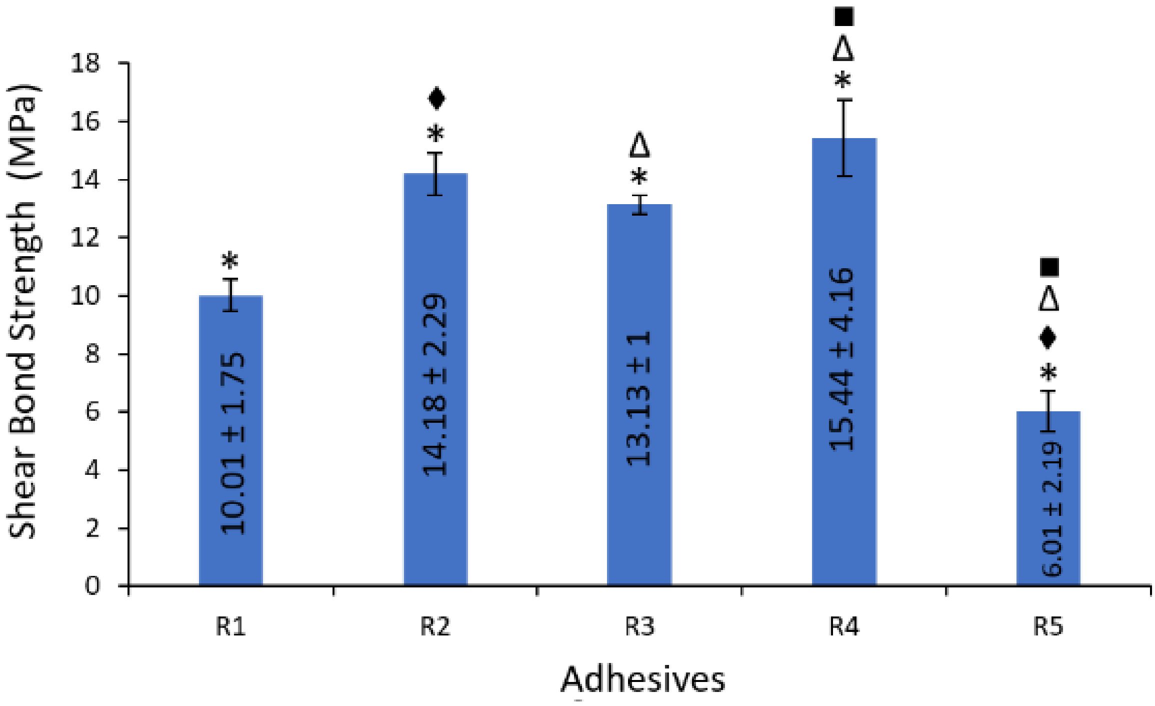

Fig. 12 Shear bond strength (Mean ± SD) of experimental adhesives. Symbol (*) indicates significant differences between R1 (control) and other groups ($P < 0.05$). Symbols (♦Δ■) represent pairwise significant differences between groups ($P < 0.05$). R1 (unfilled resin), R2 (20% CNC), R3 (15% CNC + 5% ACP), R4 (20% ACP), R5 (40% ACP + 5% CNC)

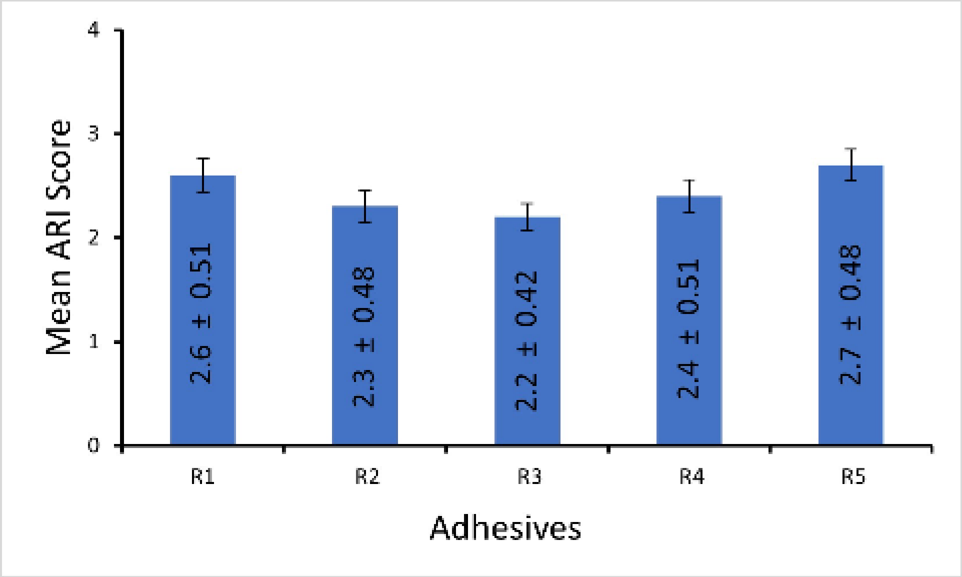

Fig. 13 Average ARI (Adhesive Remnant Index) score (Mean ± SD) based on adhesive remnants on tooth after bracket debonding. R1 (unfilled resin), R2 (20% CNC), R3 (15% CNC + 5% ACP), R4 (20% ACP), R5 (40% ACP + 5% CNC)

CONCLUSION

The effects of incorporating ACP and CNC into an experimental resin were investigated for orthodontic use. The adhesive R2, which contained 20% CNC, had a suitable shear bond strength for orthodontic applications. Adhesive R4, which contained 20% ACP, released calcium and phosphorus and also provided acceptable shear bond strength. Adhesive R3, a combination of 15% ACP and 5% CNC, released calcium and phosphorus but had a lower shear bond strength compared to R4. Adhesive R5, with 40% ACP and 5% CNC, had the highest mineral release but the lowest shear bond strength. The incorporation of ACP into the experimental resin showed promise for orthodontics and prevention of white spot lesions (WSLs). However, the addition of 5% CNC alongside ACP did not significantly affect the bracket bond strength. Further experiments are needed to confirm the therapeutic benefits of ACP and the mechanical properties of CNC in resin-based orthodontic adhesives.

CONFLICT OF INTEREST

The authors declare that they have no conflicts of interest.

FUNDING

This research did not receive any specific grant from funding agencies in the public, commercial, or not-for-profit sectors.

REFERENCES

1. Pandya M and Diekwisch T. Enamel biomimetics—fiction or future of dentistry. Int J Oral Sci 2019; 11:8.
2. Bishara S and Ostby A. White Spot Lesions: Formation, Prevention, and Treatment. Semin Orthod 2008; 14:174-182.
3. Twomley J, Yu Q, Ballard R, Armbruster P and Xu X. Formulation and characterization of antibacterial orthodontic adhesive. Dental Press J Orthod 2019; 24:73-9.
4. Walsh LJ and Healey DL. Prevention and caries risk management in teenage and orthodontic patients. Aust Dent J 2019; 64:S37-S45.
5. Nam HJ, Kim YM, Kwon YH, Kim IR, Park BS, Son WS, Lee SM and Kim YI. Enamel Surface Remineralization Effect by Fluorinated Graphite and Bioactive Glass-Containing Orthodontic Bonding Resin. Materials 2019; 12:1308.
6. Al-eesa NA, Wong FSL, Johal A and Hill RG. Flouride containing bioactive glass composite for orthodontic adhesives - ion release properties. Dent Mater 2017; 33:1324-29.
7. Zhang L, Weir MD, Chow LC, Reynolds MA and Xu HHK. Rechargeable calcium phosphate orthodontic cement with sustained ion release and re-release. Sci Rep 2016; 6:36476.
8. Xie X, Wang L, Xing D, Qi M, Li X, Sun J, Melo MAS, Weir MD, Oates TW, Bai Y and Xu HHK. Novel rechargeable calcium phosphate nanoparticle-filled dental cement. Dent Mater J 2019; 38:1-10.
9. Haghani N, Hassanzadeh Nemati N, Khorasani MT and Bonakdar S. Fabrication of polycaprolactone/heparinized nano fluorohydroxyapatite scaffold for bone tissue engineering uses. Int J Polym Mater Polym Biomater 2023.
10. Hassanzadeh Nemati N and Mirhadi SM. Study on polycaprolactone coated hierarchical meso/macroporous Titania scaffolds for bone tissue engineering. Int J Eng 2022; 35:1887-1894.
11. Lee JH, Kim HW and Seo SJ. Polymer-Ceramic Bionanocomposites for Dental Application. J Nanomater 2016; 2016:3795976.
12. Greenberg AR and Kamel I. Polymer-ceramic composite for tooth-root implant. J Biomed Mater Res 1976; 10:777-788.

13. Xie C, Zhang JF and Li S. Polymer Infiltrated Ceramic Hybrid Composites as Dental Materials. Oral Health Dent Stud 2018; 1:2.
14. Dunn WJ. Shear bond strength of an amorphous calcium-phosphate–containing orthodontic resin cement. Am J Orthod Dentofacial Orthop 2007; 131:243-7.
15. Wang WN and Meng CL. A study of bond strength between light-and self-cured orthodontic resin. Am J Orthod Dentofacial Orthop 1992; 101:350-4.
16. Rahnejat B, Hassanzadeh Nemati N, Sadrnezhaad SK and Shokrgozar MA. Promoting osteoblast proliferation and differentiation on functionalized and laser treated titanium substrate using hydroxyapatite/β-tricalcium phosphate/silver nanoparticles. Mater Chem Phys 2023; 293:126885.
17. Bienek DR, Giuseppetti AA and Skrtic D. Amorphous Calcium Phosphate as Bioactive Filler in Polymeric Dental Composites, in Calcium Phosphates - From Fundamentals to Applications. IntechOpen 2019.
18. Melo MAS, Weir MD, Rodrigues LKA and Xu HHK. Novel calcium phosphate nanocomposite with caries-inhibition in a human in situ model. Dent Mater 2013; 29:231-240.
19. Xu HHK, Moreau JL, Sun L and Chow LC. Nanocomposite containing amorphous calcium phosphate nanoparticles for caries inhibition. Dent Mater 2011; 27:762-9.
20. Chen C, Weir MD, Cheng L, Lin N, Lin-Gibson S, Chow LC, Zhou X and Xu HHK. Antibacterial activity and ion release of bonding agent containing amorphous calcium phosphate nanoparticles. Dent Mater 2014; 30:891-901.
21. Par M, Tarle Z, Hickel R and Ilie N. Real-time curing characteristics of experimental resin composites containing amorphous calcium phosphate. Eur J Oral Sci 2018; 126:426-432.
22. Durner J, Walther UI, Zaspel J, Hickel R and Reich FX. Metabolism of TEGDMA and HEMA in human cells. Biomaterials 2010; 31:818-823.
23. Yin M, Liu F and He J. Preparation and characterization of Bis-GMA free dental resin system with synthesized dimethacrylate monomer TDDMMA derived from tricyclo[5.2.1.0(2,6)]-decanedimethanol. J Mech Behav Biomed Mater 2016; 57:157-163.
24. Pratap B, Gupta RK, Bhardwaj B and Nag M. Resin based restorative dental materials: characteristics and future perspectives. Jpn Dent Sci Rev 2019; 55:126-138.
25. Xie XJ, Xing D, Wang L, Zhou H, Weir MD, Bai YX and Xu HH. Novel rechargeable calcium phosphate nanoparticle containing orthodontic cement. Int J Oral Sci 2017; 9:24-32.
26. Foster JA, Berzins DW and Bradley TG. Bond strength of an amorphous calcium phosphate- containing orthodontic adhesive. Angle Orthod 2008; 78:339-344.
27. Zhao J, Liu Y, Sun WB and Zhang H. Amorphous calcium phosphate and its application in dentistry. Chem Cent J 2011; 5:40.
28. Schumacher GE, Antonucci JM, O'Donnell JN and Skrtic D. The use of amorphous calcium phosphate composites as bioactive basing materials: their effect on the strength of the composite/adhesive/dentin bond. J Am Dent Assoc 2007; 138:1476-1484.
29. Yang Y, Chen Z, Zhang J, Wang G, Zhang R and Suo D. Preparation and Applications of

the Cellulose Nanocrystal. Int J Polym Sci 2019; 2019:1767028.

30. Sturcova A, Davies GR and Eichhorn SJ. The elastic modulus and stress-transfer properties of tunicate cellulose whiskers. Biomacromolecules 2005; 6:1055-1061.
31. Lahiji RR, Reifenberger R, Raman A, Rudie A and Moon RJ. Characterization of Cellulose Nanocrystal Surfaces by SPM. NSTI-Nanotech 2008; 2:704-7.
32. Wang Y, Hua H, Li W, Wang R, Jiang X and Zhu M. Strong antibacterial dental resin composites containing cellulose nanocrystal/zinc oxide nanohybrids. J Dent 2019; 80:23-9.
33. Leite A, Viotto H, Nunes T, Pasquini D and Pero A. Cellulose nanocrystals into Poly(ethylmethacrylate) used for dental application. Polímeros 2022; 32:e2022006.
34. Salama A. Cellulose/calcium phosphate hybrids: New materials for biomedical and environmental applications. Int J Biol.Macromol 2019; 127:606-617.
35. Luminiţa Cosma L, Şuhani RD, Mesaroş A and Eugenia Badea M. Current treatment modalities of orthodontically induced white spot lesions and their outcome – a literature review. Med Pharm Rep 2019; 92:25-30.
36. Shahmiri N, Hassanzadeh Nemati N, Ramazani Saadatabadi A and Seifi M. Cellulose Nanocrystal (CNC) Synthesis: An AFM Study. J Nanostruct 2021; 11:684-697.
37. Shahmiri N, Hassanzadeh Nemati N, Ramazani Saadatabadi A and Seifi M. The effect of acid/cellulose ratio on the quality of Cellulose Nanocrystal (CNC) suspension. J Nanoanalysis 2022.
38. Al-eesa NA, Johal A, Hill RG and Wong FSL. Flouride containing bioactive glass composite for orthodontic adhesives__ Apatite formation properties. Dent Mater 2018; 34:1127-1133.
39. Xu HHK, Weir MD, Sun L, Takagi S and Chow LC. Effects of Calcium Phosphate Nanoparticles on Ca-PO4 Composite. J Dent Res 2007; 86:378-383.
40. Chanachai S, Chaichana W, Insee K, Benjakul S, Aupaphong V and Panpisut P. Physical/Mechanical and Antibacterial Properties of Orthodontic Adhesives Containing Calcium Phosphate and Nisin. J Funct Biomater 2021; 12:73.
41. Pires-de-Souza FCP, Moraes PC, Garcia LFR, Aguilar FG and Watanabe E. Evaluation of pH, calcium ion release and antimicrobial activity of a new calcium aluminate cement. Braz Oral Res 2013; 27:324-330.
42. Ghazvini SA, Tabrizi MA, Kobarfard F, Baghban AA and Asgary S. Ion release and pH of a new endodontic cement, MTA and Portland cement. Int Endod J 2009; 4:74-8.
43. Galal M, Zaki DY, Rabie MI, El-Shereif SM and Hamdy TM. Solubility, pH change, and calcium ion release of low solubility endodontic mineral trioxide aggregate. Bull Natl Res Cent 2020; 44:42.
44. Pourhajibagher M, Ghorbanzadeh R, Salehi-Vaziri A and Bahador A. In Vitro Assessments of Antimicrobial Potential and Cytotoxicity Activity of an Orthodontic Adhesive Doped with Nano-Graphene Oxide. Folia Med 2022; 64:110-116.
45. Bationo R, Rouamba A, Diarra A, Beugré-Kouassi MLK, Beugré JB and Jordana F. Cytotoxicity evaluation of dental and orthodontic light-cured composite resins. Clin Exp Dent 2021; 7:40-48.
46. Beltrami R, Colombo M, Rizzo K, Cristofaro AD, Poggio C and Pietrocola G. Cytotoxicity of Different Composite Resins on Human

Gingival Fibroblast Cell Lines. Biomimetics 2021; 6:26.

47. Lee SM, Yoo KH, Yoon SY, Kim IR, Park BS, Son WS, Ko CC, Son SA and Kim YI. Enamel Anti-Demineralization Effect of Orthodontic Adhesive Containing Bioactive Glass and Graphene Oxide: An In-Vitro Study. Materials(Basel) 2018; 11:1728.

48. Cao T, Saw TY, Heng BC, Liu H, Yap AUJ and Ng ML. Comparison of different test models for the assessment of cytotoxicity of composite resins. J Appl Toxicol 2005; 25:101-108.

49. Vande Vannet B, Mohebbian N and Wehrbein H. Toxicity of used orthodontic archwires assessed by three-dimensional cell culture. Eur J Orthod 2006; 28:426-432.

50. Goldberg M. In vitro and in vivo studies on the toxicity of dental resin components: A review. Clin Oral Investig 2008; 12:1-8.

51. Geurtsen W, Lehmann F, Spahl W and Leyhausen G. Cytotoxicity of 35 dental resin composite monomers/additives in permanent 3T3 and three human primary fibroblast cultures. J Biomed Mater Res 1998; 41:474-480.

52. Al-Hiyasat AS, Darmani H and Milhem MM. Cytotoxicity evaluation of dental resin composites and their flowable derivatives. Clin Oral Investig 2005; 9:21-5.

53. Blanchard AB, Mon HH, Wang Y, Chapple A, Dupree P, Ballard R and et al. Formulation and characterization of experimental orthodontic adhesive containing antibacterial dimethacrylate DABCO monomers: An in vitro study. Int orthod 2022; 20:100706.

54. Tavares SW, Consani S, Nouer DF, Magnani MB, Nouer PR and Martins LM. Shear bond strength of new and recycled brackets to enamel. Braz Dent J 2006; 17:44-8.

55. Schaneveldt S and Foley TF. Bond strength comparison of moisture-insensitive primers. Am J Orthod Dentofac Orthop 2002; 122:267-273.

56. Tessore E, Mazzotta L and Fortini A. Evaluation of shear bond strength and adhesive remnant index of orthodontic brackets bonded directly or indirectly with adhesive resin cements to bovine enamel. J Dent Health Oral Disord Ther 2017; 8:521-6.

57. Li A, Cui Y, Gao S, Li Q, Xu L, Meng X, Dong Y, Liu X and Qiu D. Biomineralizing Dental Resin Empowered by Bioactive Amphiphilic Composite Nanoparticles. ACS Appl Bio Mater 2019; 2:1660-66.

58. Trilokesh C and Uppuluri KB. Isolation and characterization of cellulose nanocrystals from jackfruit peel. Sci Rep 2019; 9:16709.

59. Abiaziem CV, Williams AB, Inegbenebor AI, Onwordi CT, Ehi-Eromosele CO and Petrik LF. Isolation and characterisation of cellulose nanocrystal obtained from sugercane peel. Rasayan J Chem 2020; 13:177-187.

60. Vecbiskena L, Gross A, Riekstina U and Yang TCK. Crystallized nano-sized alpha-tricalcium phosphate from amorphous calcium phosphate: microstructure, cementation and cell response. Biomed Mater 2015; 10:025009.

61. Ramalingam M, Young MF, Thomas V, Sun L, Chow LC, Tison CK, Chatterjee K, Miles WC and Jr CGS. Nanofiber scaffold gradients for interfacial tissue engineering. J Biomater Appl 2012; 27:695-705.

62. Zhao J, Liu Y, Sun WB and Yang X. First detection, characterization, and application of amorphous calcium phosphate in dentistry. J Dent Sci 2012; 7:316-323.

63. Esposti LD, Markovic S, Ignjatovic N, Panseri S, Montesi M, Adamiano A, Fosca M,

Rau JV, Uskokovic V and Iafisco M. Thermal crystallization of amorphous calcium phosphate combined with citrate and fluoride doping: a novel route to produce hydroxyapatite bioceramics. J Mater Chem B 2021; 9:4832–4845.

64. Dorozhkin SV. Amorphous calcium (ortho)phosphates. Acta Biomater 2010; 6:4457-4475.

65. Boskey AL and Posner AS. Conversion of amorphous calcium phosphate to microcrystalline hydroxyapatite. A pH-dependent, solution-mediated, solid-solid conversion. J Phys Chem 1973; 77:2313–17.

66. Skrtic D, Antonucci JM and Eanes ED. Improved properties of amorphous calcium phosphate fillers in remineralizing resin composites. Dent Mater 1996; 12:295-301.

67. O'Donnell JNR, Antonucci JM and Skrtic D. Illuminating the role of agglomerates on critical physicochemical properties of amorphous calcium phosphate composites. J Compos Mater 2008; 42:2231-2246.

68. Skrtic D, Antonucci JM and Eanes ED. Amorphous Calcium Phosphate-Based Bioactive Polymeric Composites for Mineralized Tissue Regeneration. J Res Natl Inst Stand Technol 2003; 108:167-182.

69. Yan J, Yang H, Luo T, Hua F and He H. Application of Amorphous Calcium Phosphate Agents in the Prevention and Treatment of Enamel Demineralization. Front Bioeng Biotechnol 2022; 10:853436.

70. Skrtic D and Antonucci JM. Dental composites based on amorphous calcium phosphate-resin composition/physicochemical properties study. J Biomater Appl 2007; 21:375-393.

71. Moszner N and Salz U. New developments of polymeric dental composites. Prog Polym Sci 2001; 26:535-576.

72. Sankarapandian M, Shobha H, Kalachandra S, Mcgrath J and Taylor D. Characterization of some aromatic dimethacrylates for dental composite applications. J Mater Sci Mater Med 1997; 8:465-8.

73. Stansbury JW. Curing dental resins and composites by photopolymerization. J Esthet Restor Dent 2000; 12:300-308.

74. Yoshida K and Greener E. Effects of two amine reducing agents on the degree of conversion and physical properties of an unfilled light-cured resin. Dent Mater 1993; 9:246-251.

75. Yoshida K and Greener E. Effect of photoinitiator on degree of conversion of unfilled light-cured resin. J dent 1994; 22:296-9.

76. Chang JC, Hurst TL, Hart DA and Estey AW. 4-META use in dentistry: a literature review. J Prosthet Dent 2002; 87:216-224.

77. Leung Y and Morris MD. Characterization of the chemical interactions between 4-MET and enamel by Raman spectroscopy. Dent Mater 1995; 11:191-5.

78. Menezes-Silva R, Pereira FV, Santos MH, Soares JA, Soares SMCS and Miranda JLD. Biocompatibility of a New Dental Glass Ionomer Cement with Cellulose Microfibers and Cellulose Nanocrystals. Braz Dent J 2017; 28:172-8.

79. Haydar B, Sarikaya S and Cehreli ZC. Comparison of shear bond strength of three bonding agents with metal and ceramic brackets. Angle Orthod 1999; 69:457-462.

80. Skrtic D, Antonucci JM, Eanes ED and Eidelman N. Dental composites based on hybrid and surface-modified amorphous

calcium phosphates. Biomaterials 2004; 25:1141-50.

81. Sabir M, Muhammad N, Siddiqui U, Khan AS, Syed MR, Rahim A, Liaqat S, Shah A. T, Sharif F, Khan MA and Din IU. Effect of nanocrystalline cellulose/silica-based fillers on mechanical properties of experimental dental adhesive. Polym Bull 2022; 80.
82. Moradian M, Jafarpour D, Saadat M and Tahmasebi F. The effect of bacterial cellulose nanocrystals on the shear bond strength of resin modified glass ionomer cement to dentin. J Clin Exp Dent 2021; 13:e784-8.
83. Antonucci JM, Giuseppetti AA, O'Donnell JNR, Schumacher GE and Skrtic D. Polymerization stress development in dental composites: Effect of cavity design factor. Materials 2009; 2:169-180.
84. Chaudhari PK, Goyal L, Rana SS, Dhingra K and Kshetrimayum N. Nanocomposites and nanoionomers for orthodontic bracket bonding. Applications of Nanocomposite Materials in Dentistry, Elsevier. 2019.
85. Henkin FDS, Macêdo EDODD, Santos KDS, Schwarzbach M, Samuel SMW and Mundstock KS. In vitro analysis of shear bond strength and adhesive remnant index of different metal brackets. Dental Press J Orthod 2016; 21:67-73.
86. Leão Filho JCB, Braz AKS, Araujo RE, Tanaka OM and Pithon MM. Enamel quality after debonding: evaluation by optical coherence tomography. Braz Dent J 2015; 26:384-9.
87. Faria-Júnior ÉM, Guiraldo RD, Berger SB, Correr AB, Correr-Sobrinho L, Contreras EFR and Lopes MB. In-vivo evaluation of the surface roughness and morphology of enamel after bracket removal and polishing by different techniques. Am J Orthod Dentofacial Orthop 2015; 147:324-9.
88. Santos LK, Rocha RH, Pereira Barroso AC, Otoni RP, Carvalho de Oliveira Santos C and Fonseca-Silva T. Comparative analysis of adhesive remnant index of orthodontic adhesive systems. South Eur J Orthod Dentofac Res 2021; 8:26-30.
89. Sharma S, Tandon P, Nagar A, Singh GP, Singh A and Chugh VK. A comparison of shear bond strength of orthodontic brackets bonded with four different orthodontic adhesives. J Orthod Sci 2014; 3:29-33

J. Nanoanalysis., 11(1): 636-645, Winter 2024

Modeling and simulation of a conical dielectric probe instrument for skin cancer detection applications

Elnaz Poorreza[1] *, Noushin Dadashzadeh Gargari*[*2]

[1] *Ph. D, Faculty of Electrical engineering, Sahand University of Technology, Tabriz, Iran*
2 Department of Electrical Engineering, Aras Branch, Islamic Azad University, Jolfa, Iran*

ABSTRACT

ARTICLE INFO

Article History:

Received 2024-10-09
Accepted 2024-12-09
Published 2024-02-15

Keywords:

Heat transfer,
Temperature distribution,
Temperature change,
Skin cancer,
Conical dielectric probe,
Microwave.

Conventional techniques for diagnosing skin cancer include shape, size and skin tumor color, bleeding, a disorder in the tumor, and so on. The goal of researchers in this field of study is to find simpler and safer methods for cancer tumor detection. The conical dielectric probe will be an effective instrument for analyzing mankind tissue illnesses like the initial stage of skin cancer. This illness will be incredibly treatable when the tumors are distinguished at the initial stages. The possibility of making a probe to detect the cancerous cells with the least destructive side effect in the early stages was evaluated. Our research examined the input applied frequency variations (35GHz, 45GHz, 65GHz, and 90GHz) according to the microwave-based detection method and compared the obtained results, which are required for a better understanding of heat transfer and necrotic properties in the biological objects. According to the microwave reflection characteristics, developed models and simulations based on the finite element method, by increasing the frequency, the temperature change increases, and the proportion of damaged tissue increases slightly after 10 minutes of millimeter wave exposure.

How to cite this article
Poorreza E., Dadashzadeh Gargari N., Modeling and simulation of a conical dielectric probe instrument for skin cancer detection applications. J. Nanoanalysis., 2024; 11(1): 636-645.

*Corresponding Author Email: *noushindadashzadeh@yahoo.com*

INTRODUCTION

The skin as the outermost layer of the human body acts as the initial barrier against pathogens, chemicals, mechanical damage, and UV light. In addition to its function as a protective obstacle, the skin supports people keep the right internal temperature and allows them to sense the world through nerve endings. The skin as a complex organ, is not a homogenous structure but consists of a number of different layers with different anatomy and function. The three main layers of the skin are the epidermis, dermis, and hypodermis that are divided into several sub-layers. Giving the skin its color and protecting the body from the external environment are the responsibilities of the epidermis layer. The water content is the lowest in the stratum corneum, which is the outermost layer of the skin and part of the epidermis, and hydration increases toward the inner layers [1-4].

Skin cancers are cancer types that result from the skin tissue where other vital organs are protected by this outer layer of the body. They are due to the development and spreading of abnormal cells that have the ability to invade or spread to other parts of the body to make problems in their performance. It can be classified into two categories: melanoma and non-melanoma types. Melanoma is an aggressive skin cancer type because it can spread and invade other organs rapidly [5-9]. The current diagnostic procedure to detect skin cancer is based on a visual analysis involving full-body examination by a qualified physician using dermatoscopy. However, naked-eye observations have drawbacks such as low accuracy and false detections therefore it is regarded as a handicap in the detection process.

Microwaves which are electromagnetic waves with high frequency, have been successfully applied to a wide range of applications, such as dielectric materials evaluations and medical diagnostic and therapy areas [10, 11]. Microwave therapy system is preferred to surgery for most cancer types because it is a non-invasive process [12]. It is one of the standard treatment methods with fewer treatment-related side effects, therefore it is preferred to other methods [13].

Microwave-based detection method has gained increasing attention for early detection and diagnosis of cancer cells before they develop in other organs [14-17]. Electromagnetic measurement has been applied to biological tissue and the discovered difference in dielectric properties between healthy normal tissue and malignant tumor tissue raised the hopes toward the application of microwave for medical diagnostics, especially in cancer tumor detection fields.

Microwave measurement techniques on the skin have been used by numerous researchers for different applications, including the plain determination of the skin permittivity, the evaluation of skin tissue hydration for cosmetic investigation, and the monitoring of wound healing in medicine. Microwave reflectometry with open-ended coaxial probes or rectangular microwave probes has so far been the most commonly used method. Data for the permittivity of skin and skin tumors indicates that there is sufficient contrast between cancer and healthy skin tissue in the microwave band [1]. This contrast is a key factor for determining the healthy cell from the cancerous cell by this type of detection.

In designing a diagnostic system, the spatial resolution, frequency range and depth of sense are the factors that play important role. For those sensors that target the diagnosis or detection of skin cancer cells, a sensing depth in the range of several hundred micrometers up to one millimeter and sub-millimeter spatial resolution is sufficient [1].

Good coupling of the microwave high-frequency signal into biological organs is an important factor for high-sensitivity measurements and diagnostics. When designing a microwave system for medical purposes, there are several aspects that must be considered for better performance of the system [18].

The dielectric properties of skin tissue are directly related to parameters such as water, sodium, and protein content, which varies prominently between normal skin and malignant tumors. The water content for normal skin is around 60.9% and that for the malignant tumors is 81.7% [19]. These variations in water content are detectable in the microwave measurements range. Malignant tissue also has higher sodium content than normal skin, therefore it causes more absorption of water and takes on higher values of permittivity and conductivity. The differences in protein content of normal and up-normal tissue, may result in variations in the relaxation frequency that contributes to differentiation among these tissues in microwave measurements [19]. At microwave frequency ranges, the dielectric properties of normal skin can be distinguished from those of cancer tumors by measuring their reflection properties in early-stage of the tumor. The reflection properties of tissues that are measured by microwave measurement techniques, are directly affected by the dielectric properties of the different materials [19, 20].

In order to optimize the dielectric conical probe design with respect to measurement contrast, a good understanding of the microwave interaction with skin is needed. Several factors are important for use in clinical practical applications. However, before real experimental cancer therapy, there should be basic numerical modeling and simulation. As a result, the modeling of a conical probe is needed for a better and more profound understanding of wave propagation, heat transfer mechanism and the fraction of necrotic tissue.

To date, very few studies have been reported on the simulation of the dielectric conical probe for a skin cancer diagnosis. It motivated us to perform a series of simulations by the finite element method to better realize the probe performance. It is generally a good idea to be aware of how the variation of applied microwave frequency affects the profiles such as the temperature distribution around the tissue which is related to the heat transfer mechanism, the necrotic fraction of tissue and so on.

In this work, the electromagnetic and bio-heat equations are coupled together. Since the working frequency has a great effect on several aspects of the detection, with regard to its special characteristics, the operating frequency of the probe is varied between 35GHz, 45GHz, 65GHz and 90GHz. In the following numerical research, some input data for the microwave conditions, with different frequencies and the contrast between variable frequencies of 35GHz, 45GHz, 65GHz and 90GHz and corresponding results are presented.

MODEL DEFINITION

Parameters, geometry and boundary conditions

The millimeter waves of two microwave frequencies of 35 GHz and 95 GHz are regarded to be very sensitive to the materials with high water content. In this work, the utilization of a low-power 35 GHz, 45GHz, 65GHz, and 90GHz Ka-band millimeter wave and their reflectivity to moisture for non-invasive tumor detection has been carried out. Because skin tumors contain more moisture content in comparison with healthy ones, it results in stronger reflections profiles on this frequency range.

The abnormalities detections by the probe are defined in terms of S-parameters at the locations in which tumor cells exist. By using a 2D axis symmetric simulation model, microwave transition by a circular waveguide and a conically tapered dielectric probe to the target zone, is performed by the finite element method. The temperature changes of the skin tissue and the rate of damaged tissue analysis are conducted in the following section. According to Figure 1, the simulated model containing a circular waveguide, a tapered PTFE dielectric probe, and a phantom, regarding skin chunks. The entire presented model is bounded by an air domain regarding its outermost shell with perfectly matched layers (PML) boundary conditions to be capable of absorbing any radiation from the rod or reflected radiation from the skin phantom area. One terminal of the waveguide terminates with a circular port and is actuated utilizing the dominant TE_{1m} mode.

Here m denotes the azimuthal mode number of this presented 2D axisymmetric model which is regarded as 1 in the Electromagnetic Waves, Frequency Domain physics interface settings. The other terminal of the waveguide is adjoined to a tapered conical PTFE dielectric ($\varepsilon_r = 2.1$) rod. As demonstrated in the figure, the shape of the rod is symmetrical. Therefore, its radius increases from the inside to the outside of the waveguide, therefore for impedance matching purposes, between the two domains of a waveguide and the air, it decreases gradually. The ring-shaped structure in the middle part, makes the rod connected and stabilized on the edge of the waveguide. The ending point of the tapered rod touches the skin phantom and is in direct contact with the skin tissue.

For neglecting any dissipation of the system, the conductivity of the metallic waveguide is regarded to be high value and is modeled as a perfect electric conductor (PEC). With the chosen radius of the proposed waveguide and the applied TE mode to the system, the cut-off frequency is near 29.3 GHz, which is determined by the following equation:

$$f_{cml} = \frac{C_0 P'_{nm}}{2\pi a} \tag{1}$$

C_0 shows the speed of light, p'_{nm} denotes the root derivatives of the Bessel functions $J_n(x)$, m and n shows the mode indices, and a shows the waveguide radius. The value of p'_{11} is considered approximately 1.841. The operating frequencies of the probe, 35 GHz, 45GHz, 65GHz and 90GHz are higher than the waveguide cut-off frequency. The applied microwave is propagating through the waveguide.

As shown in Figure 2, the circular port boundary condition is considered on the inner boundary where the reflection and transmission characteristics of the applied microwave are calculated according to S parameters. In the setting section of the port boundary condition, PEC backing is regarded in the slit boundary condition part. The input power is considered about 1[mw].

Table 1 shows the geometry and operating conditions of the designed dielectric conical probe. As shown in Table 2, the electromagnetic properties of the designed model, are analyzed without a phantom. The complexity, for a healthy phantom then for a phantom containing a skin tumor is added in the next step.

Because the waveguide actuation occurs by low input power, it is expected harmless in this condition. Its influence on necrotic tissue is studied by analyzing Bioheat Transfer as well as temperature, in a 10-minute scale-time.

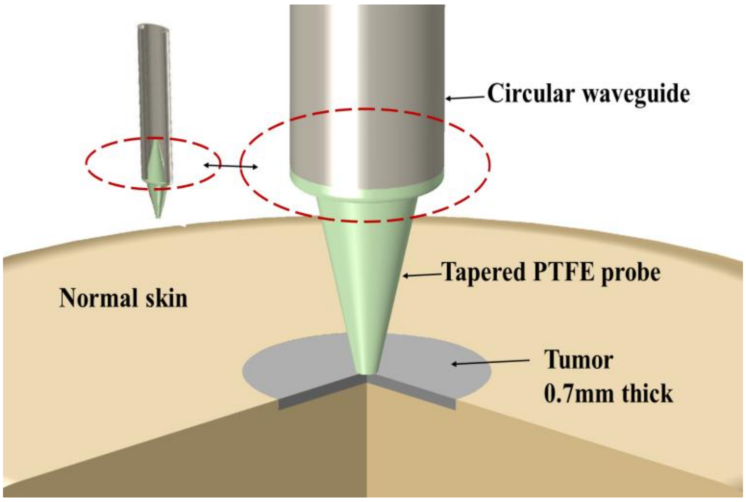

Fig. 1. The zoomed 3D picture of the skin tumor area. The entire dielectric probe model is simulated in a 2D axis symmetric dimension. The calculated S-parameters vary according to the different moisture content in each skin phantom.

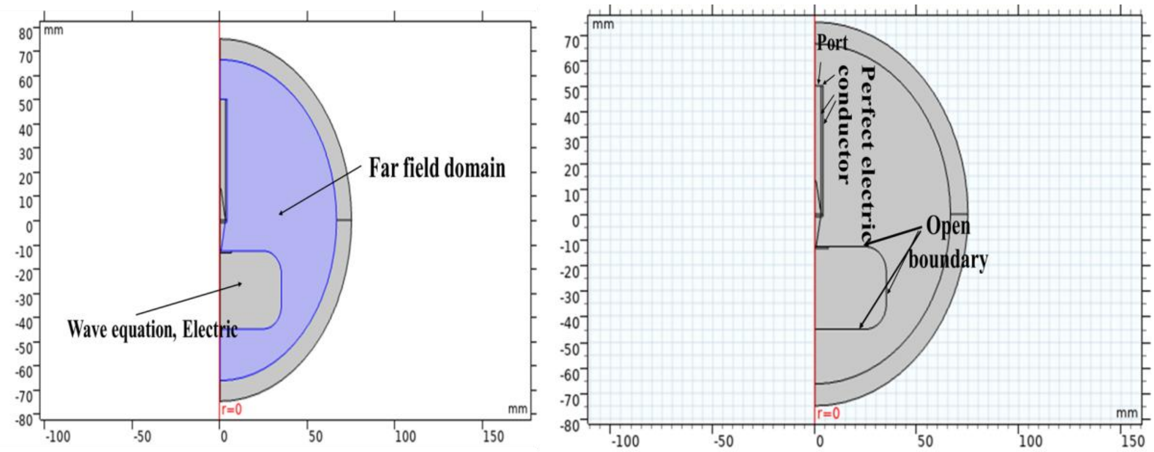

Fig. 2. Boundary conditions of conical probe.

Table 1. Operating conditions.

Name	Expression	Value	Description
f_c	1.841*c_const/2/pi/r1	2.928E10 1/s	Cut-off frequency
f_0	35[GHz],45[GHz], 65[GHz], 90[GHz]	9E10 Hz	Frequency
r_1	0.003[m]	0.003 m	Waveguide radius
lda0	c_const/f0	0.003331 m	Wavelength, free space
l_probe	12.8[mm]	0.0128 m	Tapered probe length
w_1_probe	3[mm]	0.003 m	Tapered probe width1
w_2_probe	0.58[mm]	5.8E-4 m	Tapered probe width2
T_0	34[degC]	307.15 K	Initial skin temperature

Table 2. Material property of the set-up.

Property	Probe only	healthy phantom	tumor
Relative permittivity (imaginary part)	0	10	15
Relative permittivity (real part)	1	5	8

BIOLOGICAL HEAT EXCHANGE

Pennes' bio-heat equation, has been widely applied to solve the biological heat transfer. This equation describes how heat transfer happens inside biological tissue. This equation can be defined as follows [12]:

$$\rho C\frac{\partial T}{\partial t}=\nabla\cdot(k_{th}\nabla T)+\rho_b C_b\omega_b(T_b-T)+Q_{met}+Q_{ext} \tag{2}$$

here, the left side of Eq. (2) indicates the transient term. The first, second, third and fourth terms on the right side, indicate conduction of heat, heat loss by the blood flow, internal heat or metabolic heat source, and external heat source (heat which is created by the applied electric field), respectively. (ρ_b is the blood density, C_b is the specific heat capacity of the blood, ω_b is the blood perfusion rate, T_b is the arterial blood temperature, and K_{th} is the thermal conductivity). The external heat source takes into account the effects of the resistive heat formed by the electromagnetic field which can be defined as [12]:

$$Q_{ext}=\frac{1}{2}\sigma_{Liver}\left|\vec{E}\right|^2 \tag{3}$$

The temperature rise is affected by electrical properties. When microwave waves propagate, their energy is absorbed by the tissue and converted into internal heat generation, raising the temperature of the tissue. In our study, since the probe is outside of the skin tissue, the second and third term in Eq. (2) is zero (C_b, ω_b and ρ_b are zero). T_b is considered 310.15[K].

SIMULATION RESULTS:

Figure 3 shows the real part of the electric field E_r excited from one end of the waveguide with a tumor phantom. As the figure shows, by increasing the Frequency from 35GHz to 90GHz, the density of wave fronts increases. The maximum electric field with red color, varies between 150 to 300 (V/m). When the tissue is not considered, the entire field passes and at the end of the conical probe it gradually diverges. But when the tissue is considered, the reflection of electromagnetic waves is observed. This field is in the form of spherical wave fronts and is stronger near the tip of the waveguide.

is the temperature parameter. In other words, this model is based on the temperature difference between the environment and the surface of the tissue (k (T0-T). Because the temperature of tissue which contains a tumor is higher than the temperature of tissue without a tumor, this temperature change is a good help to the diagnosis and the location of the tumor.

Temperature change on the surface of the phantom with the tumor area is depicted in Figure 4. Since the low input power of the waveguide port is considered around 1 mW, the temperature change is within 0.05 °C even after 10 minutes of millimeter wave exposure. These temperature variations with tumor cells are larger than in the case without tumor cells. It helps to diagnose the tumor cells from healthy ones. As the frequency increases from 35GHz to 90GHz, the temperature increases and reaches 0.3 °C. The color difference indicates the relatively hotter spot where the temperature is still very close to the initial temperature of 34 °C. It is easily expected that the temperature variation is less than the case with the tumor because the resistive loss should be lower due to the smaller imaginary part of the permittivity of the healthy skin.

According to Figure 5, the damaged tissue ratio is presented. It shows that the influence of the low-power millimeter wave can be neglected. As shown in the figure, the level of necrotic tissue is extremely low even after 10 minutes of microwave exposure. In spite of the fact that the maximum rate of tissue necrosis value increases with increasing frequency from 35GHz to 90 GHz, it is not significant in all cases. It can be seen that by increasing the input frequency, the area of necrosis becomes smaller and does not cover the entire area. Figure 6 shows the resistive losses in the case where the tumor is added in the middle of the center the top of skin surface. The value of resistive losses induced by the temperature, increases with increasing the applied microwave frequency.

The calculated S-parameters show more reflection when the skin with the tumor is considered, according to its higher moisture ingredient, and they are summarized as shown in Table 3.

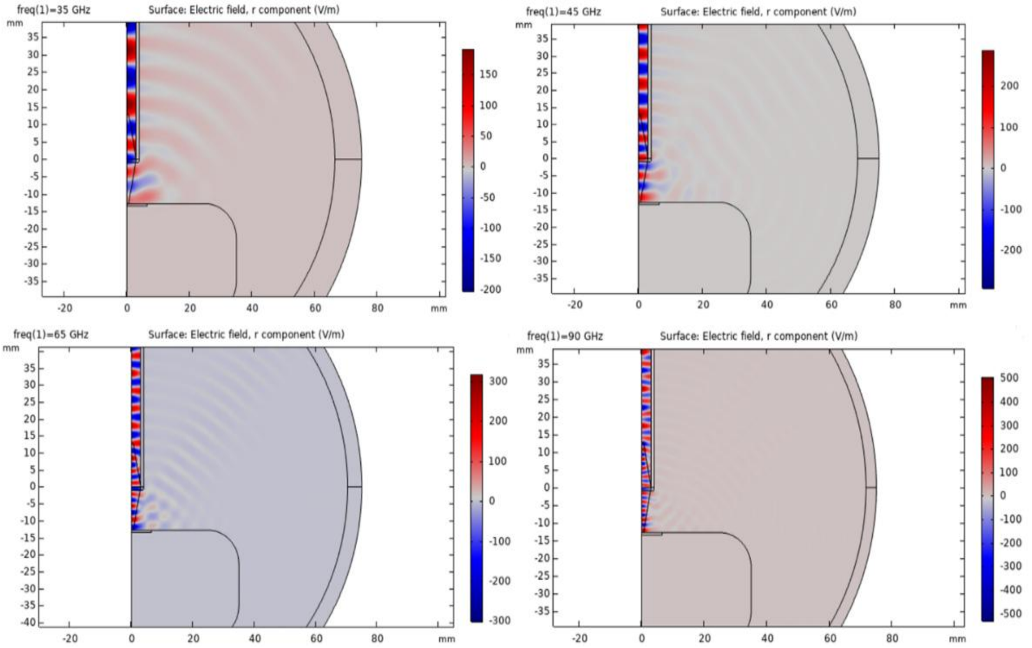

Fig. 3. Wave propagation from the dielectric rod depicted with the E_r component of the E-field.

One of the most important parameters which play a key role in determining and diagnosing skin cancer

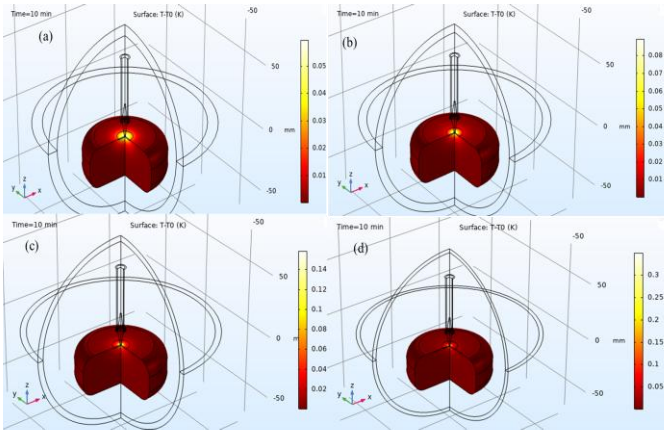

Fig. 4. The temperature profiles after 10 minutes, when the microwave frequency varied from 35[GHz],45[GHz], 65[GHz], 90[GHz].

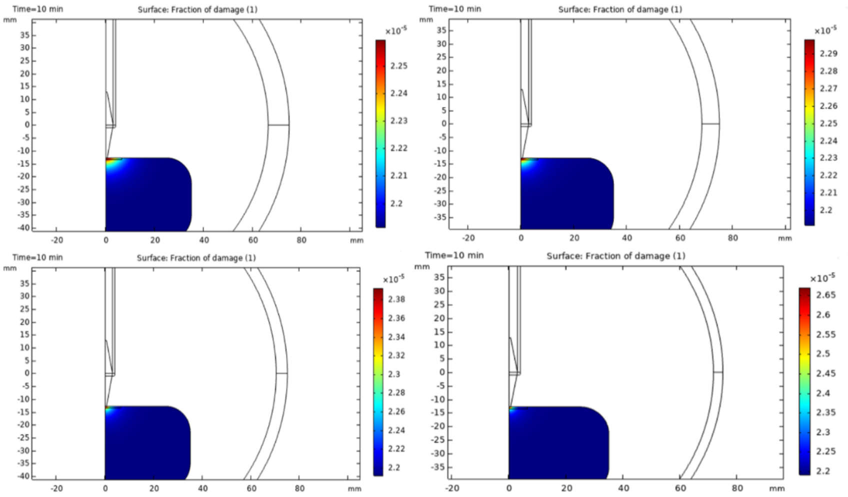

Fig. 5. The level of necrotic tissue after 10 minutes of millimeter wave exposure when the microwave frequency varied from 35[GHz],45[GHz], 65[GHz], 90[GHz].

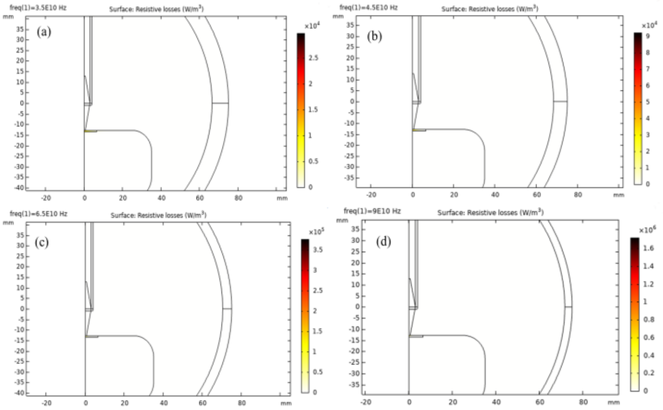

Fig. 6. The resistive losses in the case when the microwave frequency varied from 35[GHz],45[GHz], 65[GHz], 90[GHz].

Table 3. S-Parameter response of the conical probe

	Probe only	With normal Phantom	Tumor added
S11	-29.5 dB	-9.84 dB	-8.97dB

The electromagnetic material properties of skin and tumor at 35 GHz are approximated to show the feasibility of the S-parameter method by detecting the areas with higher moisture content. Figure 7 shows the graphical representations of far-field patterns in the frequency range of 35, 45, 65 and 90 GHz. As it can be seen, the radiation is from the tapered probe toward the top side. From these presented patterns, the location of cancerous tumors can be determined.

In the following section of our work, temperature change of skin tissue at the presence of tumor, at the frequency of 35GHz in times of 0, 1, 3, 5, 8, and 10 minutes were carried out. Figure 8 shows the 3D representation of the growth rate of tissue temperature with time at 0, 1, 3, 5, 8, and 10 minutes at frequency of 35GHz. As it can be clearly seen with the increase of time the amount of temperature increases and it covers the entire tumor area.

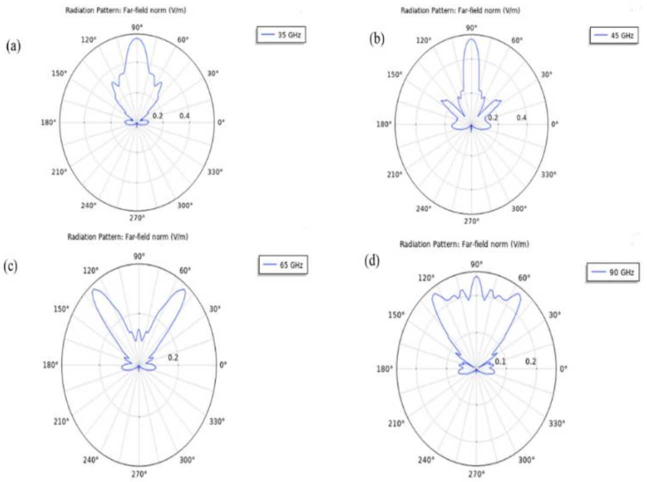

Fig. 7. The Far-field patterns in the frequency range of 35, 45, 65 and 90 GHz indicate the radiation from the tapered probe toward the top side.

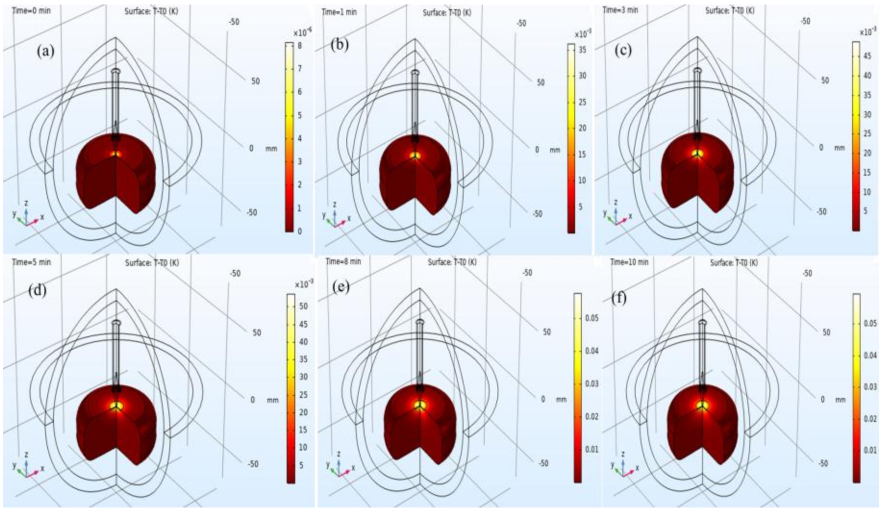

Fig. 8. The pattern of changes in temperature around the phantom in the presence of a tumor between 0 and 10 (0, 1, 3, 5, 8 and 10 minutes) minutes at 35 GHz.

CONCLUSION

The contribution of water content is important since normal skin and cancerous lesions differ in their water content as well as their salinity. Microwave signals are sensitive to both of these parameters, making these measurements ideal for skin cancer detection purposes. The results of this presented study indicate that using dielectric conical probes to measure the variation of skin properties holds promise for skin cancer tumor detection. Our work examined the input frequency variations applied and compared the obtained results, which are required for a better understanding of the heat change and necrotic properties. According to the microwave reflection characteristics, developed models and simulations, by increasing the frequency, the temperature change increases and the proportion of damaged tissue increases (not significantly) after 10 minutes of millimeter wave exposure.

REFERENCES

1. F. Töpfer and J. Oberhammer, in *Principles and Applications of RF/Microwave in Healthcare and Biosensing*, Elsevier, 2017, pp. 103.
2. F. Töpfer, S. Dudorov and J. Oberhammer, 2012.
3. M. K. Sharma, R. Kumari, A. Mittal, M. K. Upadhyay, A. Mittal and K. Singh, in *Flexible Electronics for Electric Vehicles*, Springer, 2023, pp. 47.
4. S. T. Sucharitha, I. Kannan and K. Varun Kumar, in *Intelligent Computing and Applications*, Springer, 2023, pp. 281.
5. S. Mumtaz, J. N. Rana, E. H. Choi and I. Han, Int. J. Mol. Sci., 2022, vol. 23, no. 16, 9288.
6. J. Boparai and M. Popović, *Sensors*, 2022, vol. 22, no. 5, pp. 1955.
7. E. V. Salomatina, B. Jiang, J. Novak and A. N. Yaroslavsky, *J Biomed Opt,* 2006, vol. 11, no. 6, pp. 064026.
8. V. Andreeva, E. Aksamentova, A. Muhachev, A. Solovey, I. Litvinov, A. Gusarov, N. N. Shevtsova, D. Kushkin and K. Litvinova, *Diagnostics*, 2022, vol. 12, no. 1, pp. 72.
9. H. Lui, J. Zhao, D. McLean and H. Zeng, *Cancer research*, 2012, vol. 72, no. 10, pp. 2491.
10. A. K. Gupta, P. K. Rao and R. Mishra, in *VLSI, Microwave and Wireless Technologies*, Springer, 2023, pp. p. 625.
11. M. Selmi, A. A. Bin Dukhyil and H. Belmabrouk, *Appl. Sci.*, 2019, vol. 10, no. 1, p. 211.
12. P. Keangin, P. Rattanadecho and T. Wessapan, *Int. Commun. Heat Mass Transf.*, 2011, vol. 38, no. 6, pp. 757.
13. P. Keangin and P. Rattanadecho, *Adv. Mech. Eng.*, 2018, vol. 10, no. 8, p. 1687814017734133.
14. P. Rattanadecho and P. Keangin, *Int. Commun. Heat Mass Transf.*, 2013, vol. 58, no. 1-2, pp. 457.
15. X. Wu, B. Liu and B. Xu, *Appl. Therm. Eng.*, 2016, vol. 107, pp. 501.
16. S. Kabiri and F. Rezaei, *Scientific Reports*, 2022, vol. 12, no.1, pp. 1.
17. A. Kabiri and M. R. Talaee, *Heat Mass Transf*, 2019, vol. 55, no. 8, pp. 2199.
18. G. Deshazer, P. Prakash, D. Merck and D. Haemmerich, *Int J Hyperthermia*2017, vol. 33, no. 1, pp. 74.
19. P. Mehta, K. Chand, D. Narayanswamy, D. G. Beetner, R. Zoughi and W. V. Stoecker, *IEEE Trans Instrum Meas*, 2006, vol. 55, no. 4, pp. 1309.
20. M. Gniadecka, P. A. Philipsen, S. Wessel, R. Gniadecki, H. C. Wulf, S. Sigurdsson, O. F. Nielsen, D. H. Christensen, J. Hercogova and K. Rossen, *J. Invest. Dermatol.*, 2004, vol. 122, no. 2, pp. 443.

J. Nanoanalysis., 11(1): 646-655, Winter 2024

Evaluation of physical, chemical and biological properties of silver nanoparticles and their synthesis and applications

Leila Soroudi[1]*, Seyed Ali Abtahi[2], Shahla Mahmoudi[3]

[1] Department of Environmental Engineering and Sciences, Islamic Azad University, West Tehran Branch, Tehran, Iran.
[2] Department of Soil Sciences of Faculty of Agriculture, Shiraz University, Shiraz,Iran.
[3] Department of Soil Sciences , Faculty of Agriculture and Natural Resources, University of Tehran, Tehran, Iran.

ABSTRACT

ARTICLE INFO

Article History:

Received 2023-10-04
Accepted 2025-01-05
Published 2024-02-15

Keywords:

Toxicity,

Silver nanoparticles,

Synthesis,

Properties,

Application.

Silver nanoparticles are one of the most famous and widely used nanotechnology products, it is estimated that nearly 320 tons of silver nanoparticles are used in the world every year and this widespread use causes it to eventually become a pollutant of the soil and the environment, this pollution can occur indirectly by entering the environment or directly by agricultural activities. A detailed study of the physical, chemical and biological properties of silver nanoparticles and their synthesis and applications is necessary, because the physicochemical properties of a particle can have a significant effect on its biological properties. The findings of the present study clearly showed that synthesize of silver nanoparticles with defined size and morphology under optimal conditions is possible via an eco-friendly approach. The findings revealed that silver nanoparticles produced by the green synthesis method, in spite of good antibacterial activity cause negligible cytotoxicity and the toxic effects of silver nanoparticles synthesized by physical and chemical methods are inevitable compared to biological synthesis methods. So far, a few studies have been done on the toxicity of silver nanoparticles and findings of the present study showed that the final studies on determining the toxicity of silver nanoparticles are not sufficient because their toxicity depends on many factors such as their concentration, size, shape and surface. Also sources, the route of entry, toxicological evaluation methods and dose units may vary significantly hence it is difficult to determine the exact range of toxicity of silver nanoparticles.

How to cite this article
Soroudi L., Abtahi S. A., Mahmoudi Sh., Evaluation of physical, chemical and biological properties of silver nanoparticles and their synthesis and applications. J. Nanoanalysis., 2024; 11(1): 646-655.

*Corresponding Author Email: *leilasoroudi@yahoo.com*

INTRODUCTION

Silver nanoparticles are one of the most famous and widely used nanotechnology products, it is estimated that nearly 320 tons of silver nanoparticles are used in the world every year (Nowack et al. 2011). This widespread use causes it to eventually become a pollutant of the soil and the environment, this pollution can occur indirectly by entering the environment or directly by agricultural activities (Zhang et al. 2012). Apart from primary medical applications, silver nanoparticles are also used in domestic, industrial and agricultural applications such as: water purification, plant growth and textile cleaning (Pareek et al. 2018; Hänsch and Emmerling, 2010). In the last decade, the volume of production and the fields of application of silver nanoparticles have increased due to its unique characteristics such as: high surface-to-volume ratio, high chemical reactivity and optical properties (Sun et al. 2017; Abbasi et al. 2016). Silver nanoparticles can undergo various physico-chemical transformations such as: oxidation, aggregation, dissolution, complex and secondary reactions. These developments, in turn, affect the mechanism as well as the bioavailability of silver nanoparticles and cause the toxicity of silver nanoparticles (Masrahi et al. 2014).

EXPERIMENTAL

Analysis of silver nanoparticles

Accurate description of silver nanoparticles is necessary, because the physicochemical properties of a particle can have a significant effect on its biological properties, the biological activity of silver nanoparticles depends on factors such as surface chemistry, size, size distribution, shape, particle morphology, particle composition, coverage, aggregation and dissolution rate, particle reactivity in solution, ion diffusion efficiency and cell type (Gliga et al. 2014). Therefore, the development of silver nanoparticles with controlled structures that are uniform in terms of size, morphology and performance is necessary for various applications (Sriram et al. 2010).

Properties of silver nanoparticles

Today, extensive strategies are available to modify the surface chemistry of various nanoparticles; these engineered silver nanoparticles have different optical, electrical, magnetic, chemical, and mechanical properties due to the higher surface-to-volume ratio of the material, while decreasing the size. They increase and ultimately lead to an increase in the absorption of environmental atoms and changes in the properties and behavior of materials, which begin to obey quantum mechanical laws as soon as the size of the particles decreases significantly (Carbone et al. 2014).

Physical properties of silver nanoparticles

Physical characteristics of silver nanoparticles such as size, shape, size distribution, surface area, etc. should be considered before evaluating toxicity or biocompatibility (Lin et al. 2014).

Smaller sized particles can cause more toxicity than larger particles because they have a larger surface area (Sriram et al. 2012). Shape is equally important in determining toxicity (Stoehr et al. 2011). For example, in the field of biomedicine, a variety of nanostructures have been used, including: nanocubes, nanoplates, nanorods, spherical, flower-like nanoparticles, etc. (Wei et al. 2015). The atomic density of silver affects its shape, rod or plate nanoparticles have more antibacterial activity compared to shapes (spherical, triangular, etc.) due to higher atomic density (Pareek et al. 2018). The toxicity of silver nanoparticles mainly depends on the coatings on the surface of the nanoparticles and its availability with chemical or biological substances. The surface charges of silver nanoparticles can determine their toxic effect in cells, for example: the positive surface charge of these nanoparticles makes them more suitable and allows them to be available for a long time compared to nano negatively charged particles (Schlinkert et al. 2015). What makes a toxic nanomaterial so far has not been simply defined, current knowledge shows that it largely depends on the physical properties of the nanoparticles, on the properties of the nanomaterials themselves, in particular their size, composition and surface function (Krug and Wick. 2011). As mentioned, silver nanoparticles exhibit their intrinsic antimicrobial activity through a variety of mechanisms they give (Dakal et al. 2016).

Chemical properties of silver nanoparticles

The chemical characteristics of silver nanoparticles include: the speed of dissolution of ions, oxidation potential, etc. It is silver particles, because the ionic form of silver has a greater toxic potential than silver nanoparticles (McQuillan and Shaw. 2014). It is predicted that the release of silver ions from the core of silver nanoparticles is the ultimate basis of the bactericidal activity of silver nanoparticles (Panáček et al. 2018). The surface coating also has a great effect on the kinetics of ion release from silver nanoparticles (Pareek et al. 2018).

When bacteria are exposed to silver nanoparticles, due to the formation of peroxide, superoxide and free hydroxyl ions, they experience a high level of oxidative stress, which ultimately leads to the inactivation of the bacterial cell (Reidy et al. 2013).

Biological properties of silver nanoparticles

Most studies have shown that different metals cause distinct damages to microbial cells, which include cell wall, and membrane damage, oxidative stress, protein dysfunction, and cell damage (Lemire et al. 2013). Nanomedicine is rapidly advancing, and there is a fine line between the use of innovative medical tools and the careless exposure to the use of nanomaterials that are potentially harmful to human health and the environment (Ebrahimzadeh et al. 2018). While enjoying silver nanoparticles as an option to deal with diseases, one should pay attention to the fact that the same treatment technique can also produce dangerous and unpleasant results, silver nanoparticles are toxic substances and there is still a device to determine nontoxicity. No, since silver nanoparticles have become a major drug to fight diseases such as cancer, anti-angiogenic effects in the retina, etc., researchers plan to develop silver nanoparticles that, in addition to reducing the adverse effects of toxicity include the main feature at a reasonable cost (Ebrahimzadeh et al. 2018). The biological activity of silver nanoparticles depends on the morphology and control of the size and shape of the structure of silver nanoparticles, as far as the size and shape of silver nanoparticles are concerned, the smaller the size and the shorter the triangular shape of the nanoparticles, the more effective it is and the superior properties (Zhang et al. 2016). Silver nanoparticles increase the bioavailability of therapeutic agents after systemic and local administration (Jo et al. 2015). On the other hand, it can affect cellular absorption, biological distribution, penetration into biological barriers and resulting therapeutic effects (Duan and Li. 2013). Therefore, the development of silver nanoparticles with controlled structures that are uniform in size, morphology, and functionality is essential for various biomedical applications (Zhang et al. 2016). Silver nanoparticles are one of the most widely used antimicrobial metal nanoparticles in today's era due to their inherent characteristics and extensive bactericidal effects against gram-negative and gram-positive bacteria (Shao et al. 2018). Currently, silver nanoparticles with their inherent anti-bacterial and anti-inflammatory effects are used in dressing wounds and burns, as well as in various pharmaceutical formulations such as: ointments, antibacterial clothing and medical equipment coatings (López-Esparza et al. 2016).

Synthesis methods of silver nanoparticles

The synthesis of silver nanoparticles is carried out by two methods (top-down) and (bottom-up), the term (top-down) refers to the synthesis of nanoparticles from bulk by physical processes, the (bottom-up) approach to the formation of nanoparticles refers to the constituent atoms by chemical processes, biological methods of silver nanoparticle syntheses are used as an alternative to physical and chemical methods and using microorganisms (algae, fungi, yeasts, bacteria and viruses), enzymes and plants (plant extracts) are done (Zhu et al. 2020).

Physical method of synthesis of silver nanoparticles

Evaporation, condensation and laser ablation are the most important physical approaches, the absence of solvent contamination in the prepared thin layers and the uniformity of the distribution of silver nanoparticles is one of the advantages of physical synthesis methods compared to chemical processes, high consumption of electrical energy, occupying space a lot and spending a lot of time to achieve thermal stability is one of the disadvantages of the physical synthesis method of silver nanoparticles (Iravani et al. 2014).

Chemical method of synthesis of silver nanoparticles

The most popular chemical methods for the synthesis of silver nanoparticles include: chemical reduction using a variety of organic and inorganic reducing agents, electrochemical techniques, physicochemical reduction and radiolysis, which are widely used, among the mentioned methods, the most common method for nano synthesis of silver particles are chemically reduced by organic and inorganic reducing agents, generally different reducing agents such as sodium citrate, ascorbate, sodium borohydride, hydrazine and hydroquinone are used in this method (Iravani et al. 2014). Most of these methods are still in the development stage and face practical problems such as stability and accumulation of nanoparticles, control of crystal growth, morphology, size and size distribution, extraction and purification of produced nanoparticles, the advantages of silver nanoparticles synthesis by chemical methods: ease of production, low cost and high efficiency (Gurunathan et al. 2015).

Biological method of synthesis of silver nanoparticles

To overcome the shortcomings of chemical methods, biological methods of silver nanoparticle synthesis have appeared as suitable options, recently, the synthesis of silver nanoparticles is a simple and cost-effective approach using different biological systems, including: bacteria, fungi and plants, therefore it is important to identify the biological properties of silver nanoparticles in order to evaluate the functional aspects of the synthesized particles, extracts and small biomolecules, such as vitamins and amino acids as an alternative method for chemicals are used not only for the synthesis of silver nanoparticles, but also for the synthesis of several other nanoparticles such as gold and graphene (Gurunathan et al. 2015). Gram-negative and gram-positive bacteria are indicators for the synthesis of silver nanoparticles, the main advantage of biological synthesis methods is the availability of amino acids, proteins or secondary metabolites, it seems that controlling the size and shape of the particles in the method of biological synthesis of silver nanoparticles is an important factor for various biomedical applications (Gurunathan et al. 2014). By using bacterial proteins or plant extracts as reducing agents, the shape, size and distribution of silver nanoparticles can be controlled (Zhang et al. 2016). Other advantages of the biological synthesis methods of silver nanoparticles include the availability of a wide range of biological sources, shortening of time, high density, stability and solubility of prepared silver nanoparticles in water (Zhang et al. 2016). In the method of biological synthesis of silver nanoparticles, extracts of biological agents such as: microbes and plants can be used as a reducing or protective agent to make silver nanoparticles, in these extracts there are various combinations of biological molecules that have reducing potential, such as: Amino acids, Vitamins, Proteins, Enzymes and Polysaccharides are found (Keat et al. 2015).

Applications of silver nanoparticles

Due to the unique properties of silver nanoparticles, they are used for several applications including antibacterial agents, in industrial, household and healthcare-related products, in consumer products, coating medical devices, optical sensors and cosmetics. They have been used in the pharmaceutical industry, in the food industry, in diagnostics, in orthopedics, drug delivery, as anti-cancer agents, and finally, they have increased the tumor-killing effects of anti-cancer drugs (Chernousova and Epple. 2013). Recently, silver nanoparticles have been repeatedly used in many textiles, keyboards, wound dressings and biomedical devices (Li et al. 2017). Silver nanoparticles can change the regulation of more than 1000 genes, among several genes, metallothionein, heat shock protein and H\histones were notable (Foldbjerg et al. 2012). Recently, autophagy-induced cell death has been another identified mechanism for the anticancer activity of silver nanoparticles. Nanoparticle-induced autophagy is a critical cellular degradation process, and increased autophagy can cause cell death (Lin et al. 2014). The ability of silver nanoparticles in cellular imaging can be used to study inflammation, tumors, immune response and the effects of stem cell therapy. Silver plays an important role in imaging systems due to its stronger and clearer plasmon resonance. Because of their smaller size, silver nanoparticles are mainly used in diagnosis, treatment, as well as combination therapy and diagnostic approaches, which ultimately lead to increased brightness and clearer imaging (Meyers and Cottone. 2013). Nano silver has been intensively used in several applications, including diagnosis, cancer treatment, and as a drug carrier (Ge et al. 2014). Silver nanoparticles in combination with vanadium oxide have been used in battery cell components to improve battery performance in implantable medical devices (Etheridge et al. 2013).

RESULTS AND DISCUSSIONS

RESULTS

Today, there is a need to develop eco-friendly processes, which do not use toxic chemicals in the synthesis. The biological synthesis methods of silver nanoparticles are an important field of modern research dealing with design and biosynthesis of particle structures ranging from approximately 1-100 nm. For the green synthesis of silver nanoparticles it is necessary to take plant extracts as a reducing agent and use plant extracts taken from the bark, stems, roots, leaves, flowers, oil, fruit peels and seeds, Table (1).

The findings of the present study clearly showed that can synthesize silver nanoparticles with defined size and morphology under optimal conditions and with an eco-friendly approach, Table (1). The findings revealed that silver nanoparticles produced by the green synthesis method, in spite of good antibacterial activity, cause negligible cytotoxicity. Create green the biological synthesis of silver nanoparticles does not require high temperature or toxic and dangerous additives, but the biological agents used must be carefully selected, Tables (2) and (3).

DISCUSSION

Although silver nanoparticles play an important role in clinical research, several factors such as: raw materials, synthesis method, stability, bio distribution, controlled release, and aggregation, cell-specific targeting and finally toxicological issues must be considered. A detailed study of the physical, chemical and biological properties of silver nanoparticles and their synthesis and applications is necessary, because the physicochemical properties of a particle can have a significant effect on its biological properties; this step is just as important as the synthesis approach. Nano-sized metal particles are unique and due to their surface-to-volume ratio, they can significantly change physical, chemical, and biological properties, for this reason, these nanoparticles have been exploited for various purposes (Zhang et al. 2016).

Metal nanoparticles based on their size and characteristics, have unique properties such as surface expansion, pore size, charge density on the surface, cylindrical and spherical shape, color, amorphous and crystalline structures. Environmental factors such as air, heat, sunlight and humidity affect the properties of nanoparticles. Energy sources such as light, heat, electricity, sound and short energy waves are used in the synthesis process of silver nanoparticles. In addition to the types of precursor salts, additives such as reducing agents, coating agents and stabilizers are used with the expected size and shape, and reaction parameters such as reaction temperature, time, pH and additional energy sources are used in the process. The production of silver nanoparticles is considered. Physical and chemical methods of silver nanoparticles synthesis seem very expensive and dangerous. Silver nanoparticles produced by biological synthesis method have high performance, solubility and stability (Gurunathan et al. 2015).

The green material or entity used for the production would substantially define the physical and chemical properties and as a consequence, the biological activities of the obtained nanomaterials (Rónavári et al. 2021). After the green material is selected, and its active ingredients have been regarded, all other chemicals required for nanoparticle synthesis should be attentively picked to preferentially utilize biocompatible substances and to avoid toxic chemicals (Rónavári et al. 2021).

CONCLUSION

The preferred synthesis method of silver nanoparticles is green synthesis, because it is eco-friendly, simple process, low cost, reproducible and requires a small amount of energy. In nanochemistry, the size of the particles is the most critical factor, and by using different plants, you can get nanoparticles of different sizes from the same metal. It has been clearly seen that different plants have different capabilities in reducing metal ions. Therefore, the only disadvantage of the green synthesis method is the production of smaller amounts of silver nanoparticles. The toxic effects of silver nanoparticles synthesized by physical and chemical methods are inevitable compared to biological synthesis methods. To ensure the biological safety of using silver nanoparticles in humans, studies related to the biocompatibility of silver nanoparticles and their interaction with cells and tissues should be done, and biological applications based on nanotechnology must be safe, reliable, and durable. So far, a few studies have been done on the toxicity of silver nanoparticles and the findings of the present study showed that the final studies on determining the toxicity of silver nanoparticles are not sufficient because their toxicity depends on many factors such as their concentration, size, shape and surface. Also sources, route of entry, toxicological evaluation methods and dosage units may vary considerably; hence it is difficult to determine the exact range of toxicity of silver nanoparticles.

Table (1). Synthesis of silver nanoparticles by intermediary plants

Precursor	Intermediary Plants	Size of Silver Nanoparticles (nm)
Silver Nitrate	Mentha peprita	90
Silver Nitrate	Tribulus terrestris	16–28
Silver Nitrate	Nyctanthes arbor-tristis	50–80
Silver Nitrate	Azadirachta indica	50–100
Silver Nitrate	Pelargonium sidoides	16–40
Silver Nitrate	Vigna unguiculata	24.35
Silver Nitrate	Cinnamomum camphora	55–80
Silver Nitrate	Aloe barbadensis miller	15.2 ± 4.2
Silver Nitrate	Amaranthus retroflexus	10–32
Silver Nitrate	Artocarpus heterophyllus lam	10.78
Silver Nitrate	Prunus yedoensis	20–70
Silver Nitrate	Morinda citrifolia	30–55
Silver Nitrate	Bunium persicum	20–50
Silver Nitrate	Justicia adhatoda	25
Silver Nitrate	Adenium obesum	10–30
Silver Nitrate	Coffee arabica	20–30
Silver Nitrate	Vigna radiata	5–30
Silver Nitrate	Jatropha curcas	10–20
Silver Nitrate	Lantana camara	14–27
Silver Nitrate	Sesuvium portulacastrum	5–20

Table (2). Synthesis of silver nanoparticles by intermediary bacteria

Precursor	Intermediary Bacteria for Green Synthesis	Size of Silver Nanoparticles (nm)
Silver Nitrate	Klebsiella pneumonia	1–6
Silver Nitrate	Deinococcus radiodurans	4–50
Silver Nitrate	Bacillus subtilis	20–50
Silver Nitrate	Serratia nematodiphila	10–31
Silver Nitrate	Nocardiopsis	45 ± 0.15
Silver Nitrate	Pseudomonas (proteolytic, meridiana)	6–13
Silver Nitrate	Bacillus licheniformis	18–63
Silver Nitrate	Bacillus pumilus	77–92
Silver Nitrate	Gluconacetobacter xylinus	40–100

Table (3). Synthesis of silver nanoparticles by intermediary fungi

Precursor	Intermediary Fungi for Green Synthesis	Size of Silver Nanoparticles (nm)
Silver Nitrate	Amylomyces rouxii	5–27
Silver Nitrate	Aspergillus niger	3–30
Silver Nitrate	Alternaria alternate	20–60
Silver Nitrate	Aspergillus fumigatus	5–25
Silver Nitrate	Rhizopus stolonifer	9.47
Silver Nitrate	Cladosporium sphaerospermum	15.1 ± 1.0
Silver Nitrate	Fusarium oxysporum	5–15
Silver Nitrate	Pestalotiopsis microspore	5–25
Silver Nitrate	Phanerochaete chrysosporium	50–200
Silver Nitrate	Cochliobolus lunatus	3–21
Silver Nitrate	Aspergillus terreus	6–100
Silver Nitrate	Penicillium expansum	14–76

ACKNOWLEDGEMENT

We would like to thank those who gave us the opportunity to publish this article.

CONFLICT OF INTEREST

The authors declare that they have no conflict of interest. The authors are responsible for the content and writing of this article

FUNDING

The financing of the present study was provided by the Ph.D thesis of Leila Soroudi, Islamic Azad University , West Tehran Branch , Tehran , Iran.

REFERENCES

1. Abbasi E, Milani M, Fekri Aval S, Kouhi M, Akbarzadeh A, Tayefi Nasrabadi H, Nikasa P, Joo SW, Hanifehpour Y, Nejati Koshki K. 2016. Silver nanoparticles: Synthesis methods, bio - applications and properties. Crit Rev Microbiol. 42, P. 173 – 180.
2. Carbone S, Vittori Antisari L, Gaggia F, Baffoni L, Di Gioia D, Vianello G, Nannipieri P. 2014. Bioavailability and biological effect of engineered silver nanoparticles in a forest soil. J Haz Mat. 280, P. 89 - 96.
3. Chernousova S, Epple M. 2013. Silver as antibacterial agent: Ion, nanoparticle and metal. Angew Chem Int. Ed. 52, P. 1636 - 1653.
4. Dakal TC, Kumar A, Majumdar RS, Yadav V. 2016. Mechanistic basis of antimicrobial actions of silver nanoparticles. Front Microbiol. 7, P. 1831.
5. Daun XP, Li YP. 2013. Physicochemical characteristics of nanoparticles affect circulation, biodistribution, cellular internalization, and trafficking. Small. 9, P. 1521 - 1532.
6. Ebrahimzadeh MA, Tafazoli A, Akhtari J, Biparva P, Eslami Sh. 2018. Engineered Silver Nanoparticles, A New Nanoweapon Against Cancer. J Anti-Cancer Agents in Medicinal Chemistry. 18, P. 1- 8.
7. Etheridge ML, Campbell SA, Erdman AG, Haynes CL, Wolf SM, Mc Cullough J. 2013. The big picture on small medicine: The state of nanomedicine products approved for use or in clinical trials. J Nanomedicine. 9, P. 1- 14.
8. Foldbjerg R, Irving ES, Hayashi Y, Sutherland DS, Thorsen K, Autrup H, Beer C. 2012. Global gene expression profiling of human lung epithelial cells after exposure to nanosilver. J Toxicol Sci. 130, P. 145 - 157. doi: 10.1093/toxsci/kfs225.
9. Ge LP, Li QT, Wang M, Yang JO, Li XJ, Xing MMQ. 2014. Nanosilver particles in medical applications: Synthesis, performance, and toxicity. Int J Nanomed. 9, P. 2399 - 2407.
10. Gliga AR, Skoglund S, Wallinder IO, Fadeel B, Karlsson HL. 2014. Size - dependent cytotoxicity of silver nanoparticles in human lung cells: The role of cellular uptake, agglomeration and Ag release. Part Fiber Toxicol. 11, P. 11.
11. Gurunathan S, Han JW, Kwon DN, Kim JH. 2014. Enhanced antibacterial and anti - biofilm activities of silver nanoparticles against gram - negative and gram - positive bacteria. Nanoscale Res Lett. 9(1), P. 373.
12. Gurunathan S, Han JW, Park JH, Kim E, Choi YJ, Kwon DN, Kim JH. 2015. Reduced graphene oxide - silver nanoparticle nanocomposite: A potential anticancer nanotherapy. Int J Nanomed. 10, P. 6257 - 6276.
13. Gurunathan S, Park JH, Han JW, Kim JH. 2015. Comparative assessment of the apoptotic potential of silver nanoparticles synthesized by Bacillus tequilensis and Calocybe indica in MDA-MB-231 human breast cancer cells: Targeting p53 for anticancer therapy. Int J Nanomed. 10, P. 4203 - 4222. doi: 10.2147/IJN.S83953.
14. Hänsch M, Emmerling C. 2010. Effects of silver nanoparticles on the microbiota and enzyme activity in soil. J Plant Nutr Soil Sci. 173, P. 554 - 558.
15. Iravani S, Korbekandi H, Mirmohammadi SV, Zolfaghari B. 2014. Synthesis of silver

nanoparticles : Chemical, physical and biological methods. J RPS. 9(6), P. 385 - 406.

16. Jo DH, Kim JH, Lee TG, Kim JH. 2015. Size, surface charge and shape determin therapeutic effects of nanoparticles on brain and retinal diseases. Nanomedicine. 11, P. 1603 - 1611.

17. Keat CL, Aziz A, Eid AM, Elmarzugi NA. 2015. Biosynthesis of nanoparticles and silver nanoparticles. Bioresource Bioprocess. 2, P. 47.

18. Krug HF, Wick P. 2011. Nanotoxicology: An interdisciplinary challenge. Angew Chem Int. Edit. 50(6), P. 1260 - 1278.

19. Lemire JA, Harrison JJ, Turner RJ. 2013. Antimicrobial activity of metals: mechanisms, molecular targets and applications. Nat Rev Microbiol. 11, P. 371 - 384.

20. Li WR, Sun TL, Zhou SL, Ma YK, Shi QS, Xie XB, Huang XM. 2017. A comparative analysis of antibacterial activity, dynamics and effects of silver ions and silver nanoparticles against four bacterial strains. Int Biodeterior Biodegrad. 123, P. 304 - 310.

21. Liaqat N, Jahan N, Khalil-Ur-Rahman, Anwar T, Qureshi H. 2022. Green synthesized silver nanoparticles: Optimization, characterization, antimicrobial activity and cytotoxicity study by hemolysis assay. Front Chem. 29(10), P. 952006. doi: 10.3389/fchem.2022.952006. PMID: 36105303 , PMCID: PMC9465387.

22. Lin PC, Lin S, Wang PC, Sridhar R. 2014. Techniques for physicochemical characterization of nanomaterials. Biotechnol Adv. 32, P. 711 - 726.

23. Lin J, Huang Z, Wu H, Zhou W, Jin P, Wei P, Zhang Y, Zheng F, Zhang J, Xu J. 2014. Inhibition of autophagy enhances the anticancer activity of silver nanoparticles. J Autophagy. 10, P. 2006 – 2020. doi: 10.4161/auto.36293.

24. López – Esparza J, Espinosa – cristóbal LF, Donohue – cornejo A, Reyes – López SY. 2016. Antimicrobial activity of silver nanoparticles in polycaprolactone nanofibers against gram - positive and gram - negative bacteria. Ind Eng Chem Res. 55, P. 12532 - 12538.

25. Masrahi A, Vandevoort AR, Arai Y. 2014. Effects of silver nanoparticle on soil-nitrification processes . Arch Environ Con Tox. 66, P. 504 - 513.

26. Mc Quillan JS, Shaw AM. 2014. Differential gene regulation in the Ag nanoparticle and Ag+ induced silver stress response in Escherichia coli: A full transcriptomic profile. Nanotoxicology. 8, P. 177 - 184.

27. Meyers DD, Cottone RR. 2013. Solution-focused therapy as a culturally acknowledging approach with america. J Multicult Couns Dev. 41, P. 47 - 55. doi: 10.1002/j.2161-1912.2013.00026.x.

28. Nowack B, Krug HF, Height M. 2011. 120 Years of Nanosilver History: Implications for Policy Makers. Environmental Science & Technology. 45, P. 1177 - 1183.

29. Panáček A, Kvitek L, Smékalová M, Večerová R, Kolář M, Röderová M, Dyčka F, Šebela M, Prucek R, Tomanec O, Zbořil R. 2018. Bacterial resistance to silver nanoparticles and how to overcome it. Nat Nanotechnol. 3, P. 65 - 71.

30. Pareek V, Gupta R, Panwar J. 2018. Do physico-chemical properties of silver nanoparticles decide their interaction with biological media and bactericidal action? A review. Mater Sci Eng C Mater Biol Appl. 90, P. 739 - 749.

31. Reidy B, Haase A, Luch A, Dawson KA, Lynch I. 2013. Mechanisms of silver nanoparticle release, transformation and toxicity: a critical review of current knowledge and recommendations for future studies and applications. Materials. 6, P. 2295 - 2350.

32. Rónavári A, Igaz N, Adamecz D, Szerencsés B, Molnar C, Kónya Z, Pfeiffer I, Kiricsi M. 2021. Green Silver and Gold Nanoparticles: Biological Synthesis Approaches and Potentials for Biomedical Applications. Molecules. 26, P. 844.

33. Schlinkert P, Casals E, Boyles M, Tischler U, Hornig E, Tran N, Zhao J, Himly M, Riediker M, Oostingh GJ. 2015. The oxidative potential of differently charged silver and gold nanoparticles on three human lung epithelial cell types. J Nanobiotechnol. 13(1),

P. 1 - 18.

34. Shao Y, Wu C, Wu T, Yuan C, Chen S, Ding T, Ye X, Hu Y. 2018. Green synthesis of sodium alginate-silver nanoparticles and their antibacterial activity. Int J Biol Macromol. 111, P. 1281 - 1292.

35. Sharma NK, Vishwakarma J, Rai S, Alomar TS, AlMasoud N, Bhattarai A. 2022. Green Route Synthesis and Characterization Techniques of Silver Nanoparticles and Their Biological Adeptness. ACS Omega. 7(31), P. 27004 - 27020. doi.org/10.1021/acsomega.2c01400

36. Soliman MKY, Salem SS, Abu-Elghait M, Azab MS. 2023. Biosynthesis of Silver and Gold Nanoparticles and Their Efficacy Towards Antibacterial, Antibiofilm, Cytotoxicity and Antioxidant Activities. Appl Biochem Biotechnol. 195(2), P. 1158 - 1183. Doi: 10.1007/s12010-022-04199-7. PMID: 36342621 ; PMCID: PMC9852169.

37. Sriram MI, Kalishwaralal K, Barathmanikanth S, Gurunathani S. 2012. Size - based cytotoxicity of silver nanoparticles in bovine retinal endothelial cells. Nanoscience Methods. 1(1), P. 56 - 77.

38. Sriram MI, Kanth SB, Kalishwaralal K, Gurunathan S. 2010. Antitumor activity of silver nanoparticles in Dalton's Lymphoma ascites tumor model. Int J Nanomed. 5, P. 753 - 762.

39. Stoehr LC, Gonzalez E, Stampfl A, Casals E, Duschl A, Puntes V, Oostingh GJ. 2011. Shape matters: Effects of silver nanospheres and wires on human alveolar epithelial cells. J Particle and Fibre Toxicology. P. 8. https://doi.org/10.1186/1743-8977-8-36

40. Sun TY, Mitrano DM, Bornhöft NA, Scheringer M, Hungerbühler K, Nowack B. 2017. Envisioning nano release dynamics in a changing world: Using dynamic probabilistic modeling to assess future environmental emissions of engineered nanomaterials. Environ Sci Technol. 51(5), P . 2854 - 2863.

41. Wei L, Lu J, Xu H, Patel A, Chen ZS, Chen G. 2015. Silver nanoparticles: Synthesis, properties and therapeutic applications. Drug Discov Today. 20(5), P. 595 - 601.

42. Zhang XF, Liu ZG, Shen W, Gurunathan S. 2016. Silver Nanoparticles: Synthesis, Characterization, Properties, Applications and Therapeutic Approaches. Int J Mol Sci. 17(9), P. 1534.

43. Zhang Z, Kong F, Vardhanabhuti B, Mustapha A, Lin M. 2012. Detection of engineered silver nanoparticle contamination in pears. J Agric Food Chem. 60, P. 10762 - 10767.

44. Zhu L, Gharib M, Becker C, Zeng Y, Ziefub AR, Chen L, Alkilany AM, Rehbock C, Barcikowski S, Parak WJ, Chakraborty I. 2020. Synthesis of Fluorescent Silver Nanoclusters: Introducing Bottom-Up and Top-Down Approaches to Nanochemistry in a Single Laboratory Class. J Chem Educ. 97(1), P. 239 – 243.

J. Nanoanalysis., 11(1): 656-661, Winter 2024

Comparison of the effect of Fe_3O_4 nanoparticles synthesized by green and chemical methods on liver function as well as oxidative stress and metal regulation genes expression in rats

Farzaneh Karimi[1], Kahin Shahanipour[1*], Nooshin Naghsh[2], Noosha Zia-Jahromi[3]

[1] *Department of Biochemistry, Falavarjan Branch, Islamic Azad University, Isfahan, Iran.*
[2] *Department of Biology, Falavarjan Branch, Islamic Azad University, Isfahan, Iran.*
[3] *Department of Biology, Shahrekord Branch, Islamic Azad University, Shahrekord, Iran.*

ABSTRACT

In biomedicine, magnetic nanoparticles (MNPs) have been used for the treatment of numerous disorders and targeted drug delivery. Among iron oxides, Fe_3O_4 can be useful in effective drug delivery to target tissues such as the liver. In this study, the side effects of Fe_3O_4 nanoparticles synthesized by the green method were compared to chemical methods in liver tissue. Gene expression analysis of metallothionein-1 and glutathione reductase-1, in addition to liver biochemical function was measured. Forty-two rats were studied in 7 groups. A control-l group with standard food (N = 6) and six treatment groups were administered 50, 100, and 150 mg/kg Fe_3O_4 nanoparticles synthesized by green and chemical methods, respectively (N = 6 for every treatment group). The destruction of liver tissue was more in the groups treated with chemicals compared to the groups treated with green synthesis nanoparticles. Also, biochemical analysis presented significant alterations in *SGPT* level in the treated groups, however, no significant finding was observed in the level of SGOT and ALK levels. Tea nanoparticles showed a significant increase in the expression level of MT1 and GR genes in the treated groups. The findings showed that the nanoparticles prepared by chemical method caused more damage to the liver tissue than the green nanoparticles, and the changes in the expression of genes involved in homeostasis in the groups treated with green synthetic nanoparticles were significantly positive.

ARTICLE INFO

Article History:

Received 2024-10-31
Accepted 2024-12-09
Published 2024-02-15

Keywords:

Fe_3O_4 nanoparticles,
MT1,
GR,
Gene expression,
Metabolism.

How to cite this article
Karimi F., Shahanipour K., Naghsh N., Zia-Jahromi N., Comparison of the effect of Fe_3O_4 nanoparticles synthesized by green and chemical methods on liver function as well as oxidative stress and metal regulation genes expression in rats. J. Nanoanalysis., 2024; 11(1): 656-661.

*Corresponding Author Email: *shahanipur_k@yahoo.com*

INTRODUCTION

Green synthesis nanotechnology refers to the production of nanomaterials or nanoparticles without using dangerous chemicals that emit poisonous byproducts. Green synthesized nanoparticles have many applications in medical science, drug delivery, and chemotherapy. Many strategies have been involved in the process of their synthesis to be safe and without side effects [1,2].

The goal of creating metal oxide nanoparticles is to change the properties of metals and increase their reactivity and efficiency. Iron oxide, aluminum oxide, cerium oxide, titanium oxide, and magnetite are examples of the several utilized metal oxide nanoparticles [3]. In biomedicine, magnetic nanoparticles (MNPs) have been used to induce heat to treat hyperthermia, provide contrast effects for magnetic resonance imaging, and control targeted drug delivery remotely. Numerous iron oxides are known, which usually categorized in to three types: Fe_3O_4 (magnetite), α-Fe_3O_4 (hematite), and γ-Fe_3O_4 (maghemite). Among all iron oxides, Fe_3O_4, due to superior magnetic properties, has attracted more attention [4]. Based on their employment, Fe_3O_4 nanoparticles appear to have more excellent capability and capacity than Fe_3O_4 nanoparticles [1].

Nanoparticle size and surface charge determine its biological properties, such as absorption by cells and distribution in the body [5]. The nanoparticles deposit in essential organs like the brain, liver, or kidneys after entering the body by ingestion, inhalation, contact with the skin, or interaction with the genitourinary tract. Nanoparticles impair cellular activities by crossing membranes and interacting with biomolecules, damaging DNA and proteins or crossing the blood-brain barrier, causing neurological damage. Therefore, the need for primary research on nanoparticles' effect on biochemical parameters is emphasized [6]. This study focused on *MT1* and *GSR* genes as two appropriate markers for analyzing oxidative stress and tissue resistance to metals. Invertebrates, plants, bacteria, and vertebrates all have low-molecular-weight, cysteine-rich intracellular proteins called metallothioneins (MTs). The metallothionein molecules' α and β binding domains are made up of cysteine clusters. The peptide N-terminal region, known as the β-domain, has three binding sites for two-valent ions. Also, the C-terminal area (α-domain) can bind to four two-valent metal ions. Many organs contain *MT1* and *MT2*, including the kidneys, liver, gastrointestinal tract, and pancreas. The brain, cardiovascular system, retina, kidneys, breasts, prostate, bladder, and genital organs contain *MT3*. On the other hand, *MT4* is mainly found in squamous epithelium stratified [7,8]. These molecules can also help modulate and improve immune responses by controlling the levels of toxic metals [9]. MTs elevate the tolerance of the cells to the radical species. The liver is the main organ of the body with antioxidant weapons. Liver cells use glutathione as the most critical antioxidant in mammals that directly eliminates various oxidants, including (superoxide anion, hydroxyl radical, nitric oxide, and carbon radicals) [10,11]. An NADPH-dependent oxidoreductase called glutathione reductase (GR) expedites the transformation of oxidized glutathione (GSSG) to reduced glutathione (GSH) [12,13]. Biochemically, oxidation products are widely used to measure oxidative stress [14]. Metalloenzymatic alkaline phosphatase (ALP) [EC 3.1.3.1] consists of several isoenzymes. It is said that each isozyme evolves from a common ancestral gene and is a membrane-bound glycoprotein encoded by particular locus genes. Chromosome 2 harbors three ALP genes, while chromosome 1 harbors the fourth [15]. Therefore, in this study, by synthesizing nanoparticles using the green method, its effects on liver enzymes, liver tissue, and antioxidant genes were investigated, and we compared the results with the effects of nanoparticles synthesized by chemical methods.

EXPERIMENTAL

Material and methods

Synthesis of green Fe_3O_4 nanoparticles

Green method

Green tea was utilized to make Fe_3O_4 nanoparticles. Green tea extract was added dropwise to a room-temperature 1:2 iron chloride solution. The creation of iron oxide nanoparticles was verified by developing a solid, black solution after the mixture had been agitated with a magnetic stirrer for 15 minutes. Centrifugation was used to separate the nanoparticles at 15,000 rpm for 10 minutes, followed by three to four rounds of washing with ethanol and water. The nanoparticles are dried in a 70 °C oven for 3 hours and kept in a covered container [16].

Chemical method

$FeCl_2\ 4H_2O$ (1.98 g), $FeCl_3\ 6H_2O$ (5.41 g), and NaOH (3.2 g) were dissolved in 100 ml of distilled water for the production of Fe_3O_4 nanoparticles. The reaction temperature was increased to 80°C and maintained there for two hours after stirring for 20 minutes. A magnetic decantation process was used to separate the resultant black precipitate, which was then washed three times with distilled water and ethanol. Magnetic nanoparticles were dried out under low pressure. The supplies were all purchased from Sigma Company (USA).

Chemical Fe_3O_4 coating with chitosan

To prepare chitosan solution, 1.74 ml of acetic acid (99%) was added to 300 ml of deionized distilled water. Then 0.125 g of chitosan powder was weighed and 300 ml of solution was added to it and stirred for 20 minutes with a magnetic stirrer until the powder was dissolved in the solution. 20 ml of this solution was removed and its pH was adjusted to 4.8 with NaCl (1 M). Then weigh 0.5 g of Fe_3O_4 that we produced by chemical method and add it to it and mix it for 30-45 minutes. With this method, we coated the Fe_3O_4 nanoparticle which was chemically synthesized with chitosan.

Particle size, PDI, and zeta potential

Dynamic light scattering (DLS) was used to gauge the size of nanoparticles. The magnetically created nanoparticles zeta potential, polydispersity index, and particle size were measured using the Zeta-sizer (Nano ZA, Malvern Instruments, UK). The temperature was 25 °C, the detecting angle was 135°, and the number of captured nanoparticles ranged from 1400 to 1930 kilo counts per second (KCPS). The Zetasizer used the same method to calculate zeta potential (Nano ZA, Malvern Instruments, and UK).

Animal treatments

In the present study, 42 male Wistar rats with an average weigh 250 ± 15.34 g and with ages of 8 to 9 weeks were involved in the study, including seven groups: 1-Control (sterile saline solution), 2- Fe_3O_4 nanoparticles made by green method at a dose of 50 mg/kg, 3- Fe_3O_4 nanoparticles made by the green way at a dose of 100 mg/kg, 4- Fe_3O_4 nanoparticles made by green method at a dose of 150 mg/kg, 5- Chemically synthesized Fe_3O_4 nanoparticles at a dose of 50 mg/kg, 6- Chemically synthesized Fe_3o_4 nanoparticles at a dose of 100 mg/kg and 7- Chemically synthesized Fe_3O_4 nanoparticles at a dose of 150 mg/kg. Animals were maintained on a 12-hour light cycle at room temperature and controlled humidity. Animals had unrestricted access to standard laboratory water and nutrition. Sterile saline-soluble iron nanoparticles were injected intraperitoneally (IP) daily for 30 days. Our study protocol was reviewed and approved by Najafabad Branch, Islamic Azad University Ethics and Laboratory Animal Rights Monitoring Committee with the ethics code IR.IAU.NAJAFABAD.REC.1400.070.

Liver tissue biopsy, staining, and blood sampling

24 hours after discontinuation of the last treatment, rats were anesthetized with 10% ketamine and 2% xylazine. Blood samples were taken by heart perforation in sterile centrifuge bottles and rotated for 5 minutes to separate the serum. A part of the liver of each animal was removed and saved at - 80 ° C for RNA extraction and gene expression analysis. H&E staining was utilized to assess the histological shifts of rat liver tissues by a microscopic analysis based on the vain and cells morphological maintenance.

Biochemical assays

Aspartate aminotransferase (AST) and Alanine aminotransferase (ALT) are determined using the Abcam commercial kits (Cat. No. ab105135 and ab105134 respectively. Abcam Co. USA). Alkaline phosphatase (ALP) was measured using a commercial kit from Randox.

Gene expression analysis

RNA extraction and cDNA synthesis

According to the manufacturer's instructions, RNA was extracted from liver tissues using RNXplus buffer (Cinaclon Co., Iran). The first strand of cDNA was then produced with 50 ng total RNA using oligo primers (dT) and random hexamer as directed by the manufacturer using a cDNA synthesis kit (SmoBio Co., South Korea).

Primer design and real time RT-PCR

Dedicated primers for *GR* and *MT1* genes were designed utilizing Generunner software version 6.5.52, 64-bit (Table 1). Also, *ActB* gene was selected as reference gene or internal control. Realtime-RT-PCR was performed using ABI system StepOne (Applied Biosystem, USA) in final reaction mixture volume 20 µl containing 1X Master Mix, 3.5 µl of DEPC water, 0.5 µl of each of the forward and reverse primers, and 0.5 µl of template cDNA. All reactions were performed in duplicate well in 40 cycles containing 95ºC for 15 sec, 55 ºC for 30 sec, and 72 ºC for 30 sec. Also, melting curve was calculated between 65 ºC and 95 ºC with ramping rate 0.3 ºC/1min.

Data analysis

Data were provided as mean ± SEM. SPSS V.21 software was utilized to perform a one-way analysis of variance (one-way ANOVA) on the data. At P <0.05, the mean values were considered statistically significant. For data normality analysis, the Kolmogorov-Smirnov test was used. Finally, Prism V.9.0.0 was utilized for graph preparation.

Table 1. Primer sequences and their properties.

Primer name	Sequence	Target length	Target gene	Accession no.
FACTBRat	5’- AGCCTTCCTTCCTGGGTATGG-3’	109bp	*ActB*	NM_031144.3
RACTBRat	5’ AGCACTGTGTTGGCATAGAGG-3’			

FMT1rat	5'-GCTCCAGCGGCTGCAAGAAC-3'	129bp	*MT1*	NM_138826.4
RMT1rat	5'-AGCACGTGCACTTGTCCGAG-3'			
FGSRrat	5'- CACTGAAGATGAAGCCGTC-3'	124bp	*GR*	NM_053906.2
RGSRrat	5'- ACAAACCATCTTCATCACGC-3'			

RESULTS AND DISCUSSIONS

Nanoparticle properties

Table 2 shows some specific properties of the produced nanoparticles. Results of the particle analysis confirmed the standard indexes for a nanoparticle. Figs. 1a and 1b shows SEM image of green and chemical nanoparticles respectively. Figs. 2a and 2b show FT-IR results on the synthesized nanoparticles.

Nanoparticles have special physical, chemical, mechanical, electrical and magnetic properties due to their small size; they easily enter the cell and interfere in its natural and vital process. The use and application of nanotechnology in various branches of science such as medicine, pharmaceuticals, imaging, environment and industry has attracted the attention of many scientists. Nanoparticles are spherical materials found in nanometer size and derivatives of iron oxide paramagnetic nanoparticles with different and variable coatings are used in drug delivery mechanism. Therefore, evaluating the bioavailability of these nanoparticles seems necessary to understand the mechanisms of action and toxicity resulting from their activity. Many researchers have used biological methods to synthesize metal nanoparticles or metal oxides from different parts of plants, especially leaves, stems, roots, and fruits. However, magnetite nanoparticles behave differently depending on how they are synthesized. In addition, the size and shape of the magnetite crystal affects its magnetic properties.

Table 2. Physical properties of the produced Fe_3O_4 nanoparticles.

Particle name	Color	Particle size Mean ± SD	Zeta potential (mV)	PDI (Polydispersity Index)
Green tea extract method	Green	21.51 ± 1.7	-25±0.87	0.4±0.45
Chemical method	Brown	13.19 ± 1.2	-19 ± 0.34	0.2 ± 0.91

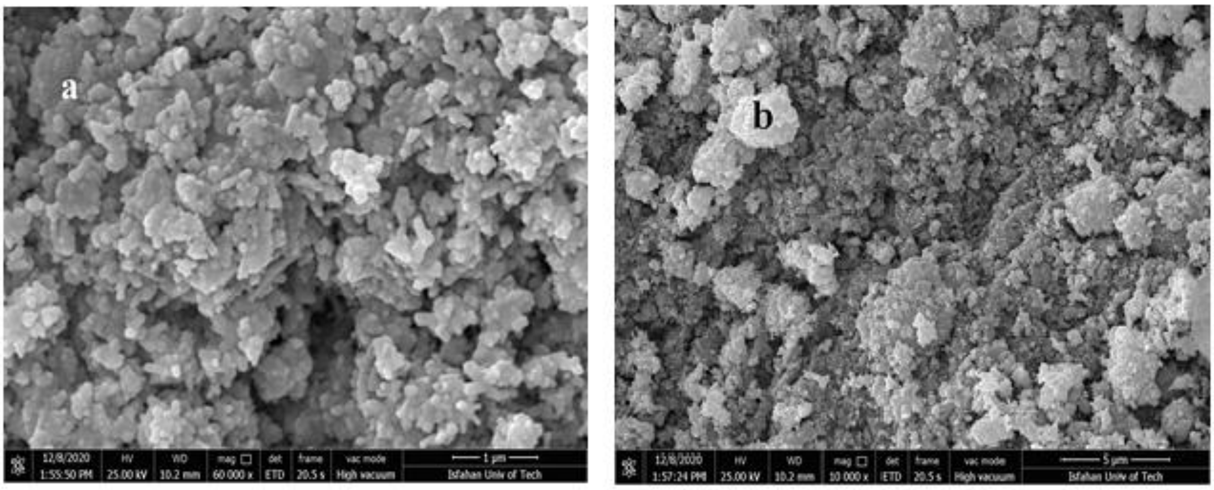

Fig. 1. a. SEM image of green tea extract method synthesized Fe_3O_4 nanoparticles. **b**. SEM image of chemical method synthesized Fe_3O_4 nanoparticles

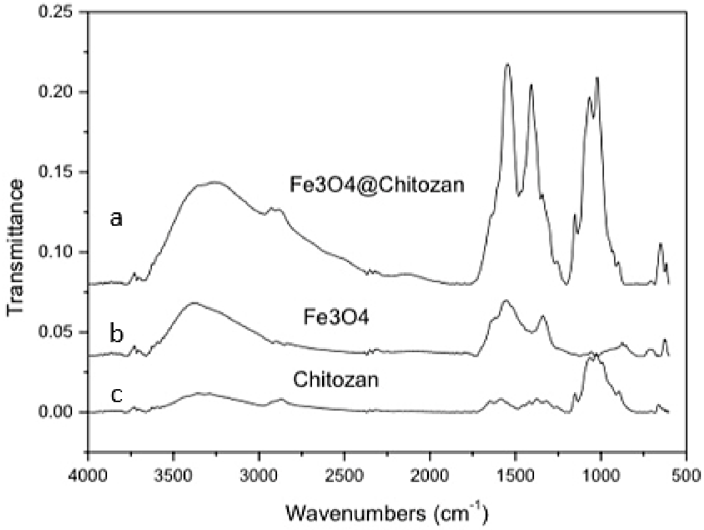

Fig. 2. FT-IR graph of the synthesized nanoparticles. a. Nanoparticle coated with chitosan and b. Fe_3O_4 nanoparticle and c. Chitosan

Pathological findings

Fig. 3 presents Hematoxylin-Eosin staining of the dissected tissue of the treated rats with the green nanoparticles compared with chemical nanoparticles.

In this study, Fe_3O_4 nanoparticles were synthesized by two chemical and green methods, and the effect of these synthetic nanoparticles as well as chitosan-coated nanoparticles in different concentrations on the activity of rat liver enzymes and gene expression was investigated. Yusefi et al. utilized Fe_3O_4 nanoparticles to destroy colon cancer cells. Fe_3O_4 nanoparticles were precipitated with the crude extract of *Garcinia mangostana* fruit in different weight percentages. HCT116 colon cancer cells were destroyed by the generated samples more than normal CCD112 colon cancer cells [17]. In the studies of Al-Karagoly et al., iron oxide nanoparticles (IONPs) were synthesized using black seed extract, and as a strong rejuvenating agent, their cytotoxic and antibacterial properties were investigated. In addition to the significant non-cytotoxic effect shown by MTT in Vero cell line, these biosynthetic nanoparticles (IONPs) showed excellent antibacterial activity against Escherichia coli and Staphylococcus aureus [18].

Biochemistry analysis

Serological analysis of the serum collected from the treated rat's blood showed some variance between the level of SGPT, SGOT and ALK enzymes between the control groups, the groups treated with the chemical synthesized nanoparticles and the groups treated with the green tea synthesized Fe_3O_4 nanoparticles (Figs. 4, 5, and 6).

No significant differences were observed between the chemical synthesized nanoparticles treated groups in comparison with the control and green tea synthesized Fe_3O_4 nanoparticle groups. C: control group, 1, 2, and 3 are 50, 100 and 150 mg dose of chemical synthesized Fe_3O_4 nanoparticle respectively. 4, 5, and 6 are 50, 100 and 150 mg dose of green tea synthesized Fe_3O_4 nanoparticle respectively.

Significant differences were observed between the chemical synthesized nanoparticle treated groups in comparison with the control and green tea synthesized Fe_3O_4 nanoparticle groups. C: control group, 1, 2 and 3 are 50, 100 and 150 mg dose of chemical synthesized Fe_3O_4 nanoparticle respectively. 4, 5 and 6 are 50, 100 and 150 mg dose of green tea synthesized Fe_3O_4 nanoparticle respectively.

No significant differences were observed between the chemical synthesized nanoparticle treated groups in comparison with the control and green tea synthesized Fe_3O_4 nanoparticle groups. However, there is significant difference in the ALK level between the ends of course analysis compared with the middle of the course. C: control group, 1, 2 and 3 are 50, 100 and 150 mg dose of chemical synthesized Fe_3O_4 nanoparticles respectively. 4, 5 and 6 are 50, 100 and 150 mg dose of green tea synthesized Fe_3O_4 nanoparticles respectively.

The effects of silver nanoparticles on the metabolism of Wistar rats were investigated in a study. Mice were treated daily with silver nanoparticles (AgNPs). AgNPs did not affect the amount of food eaten by mice or their weight. But when mice were exposed to AgNP, serum and tissue levels of AST, ALT and ALP changed significantly. After treatment with 100 mg/kg of silver nanoparticles, the level of AST and ALT in the blood and tissues of mice decreased significantly. On the other hand, when AgNPs were given to mice, ALP levels increased in their blood and tissues [6]. In the studies of Albukhaty et al. superparamagnetic iron oxide nanoparticles were coated with poly-L-lysine (SPIONs-PLL). These nanoparticles were used to evaluate the efficiency of gene expression for SPIONs-PLL as a non-viral carrier in NSCs. Histological analysis showed that the concentration of intracellular nanoparticles is higher than that of intercellular nanoparticles. Therefore, these results indicated that SPIONs-PLL can act as a new alternative for transfection of BDNF-NSCs, which is useful for gene therapy [19].

In the blood and tissues of male Wistar rats, the toxicity of molybdenum trioxide nanoparticles was investigated by Akhundipour et al. The findings showed that high concentrations are more harmful than low values for blood and serum parameters [20]. In a study on adult male Wistar rats, TiO_2 nanoparticles were administered orally. Data showed that oral administration of TiO_2 nanoparticles (<100 nm) may lead to hepatotoxicity in mice [21]. For 28 days, Wistar rats of both sexes were gavage with small silver nanoparticles (10 nm) coated with polyvinylpyrrolidone (PVP). Oxidative stress markers and blood parameters were changed in all animals, indicating the toxicity of AgNPs even at moderate doses. Gender differences are evident in all analyzed parameters. Compared to male mice, female rats receiving moderate amounts of AgNPs eliminated nanoparticles more efficiently from their liver and kidneys.

In this research by examining the effect of Fe_3O_4 nanoparticles on the activity of liver enzymes in rats after 30 days of treatment, it was found that nanoparticles synthesized by chemical method had the most destructive effect on hepatocytes at concentrations of 100 and 150 (mg/kg). As a result, the activity of liver enzymes increased and can lead to tissue destruction. Nanoparticles synthesized by the green method did not have a destructive effect on liver cells and did not show significant results after examining the activity of the studied enzymes compared to the control group and the group treated with chemically synthesized nanoparticles.

Chitosan is considered a polymer and is obtained by deacetylation of chitin. Chitin is found naturally in the exoskeleton of crustaceans and the cell wall of fungi, which is the second most abundant natural polymer after cellulose. The length and acetyl residues of the resulting chitosan polymers are different depending on the conditions used in the deacetylation method. It may be converted into molecules with weights between 300 and over 1000 kD In addition, the degree of chitosan acetylation, which ranges from 5 to 70%, significantly affects the physicochemical properties, including viscosity and solubility. Therefore, this non-toxic and biodegradable compound was used to coat iron oxide nanoparticles. [22].

The results showed that the coating of artificial nanoparticles with chitosan reduces the destructive effect of Fe_3O_4 nanoparticles on liver cells to such an extent that the activity of the enzymes studied in the control group decreased compared to the group treated with Fe_3O_4 nanoparticles synthesized by chemical method. Considering that the destructive effect of iron oxide nanoparticles on liver cells follows the use of magnetic fields, these magnetic fields activate processes in the body that conduct messages from the cell membrane to the nucleus and genetic content. It also affects the function of organs and changes the cell membrane potential and ion distribution in the cell. These changes affect biochemical processes and change the activity of serum enzymes and biochemical parameters [23].

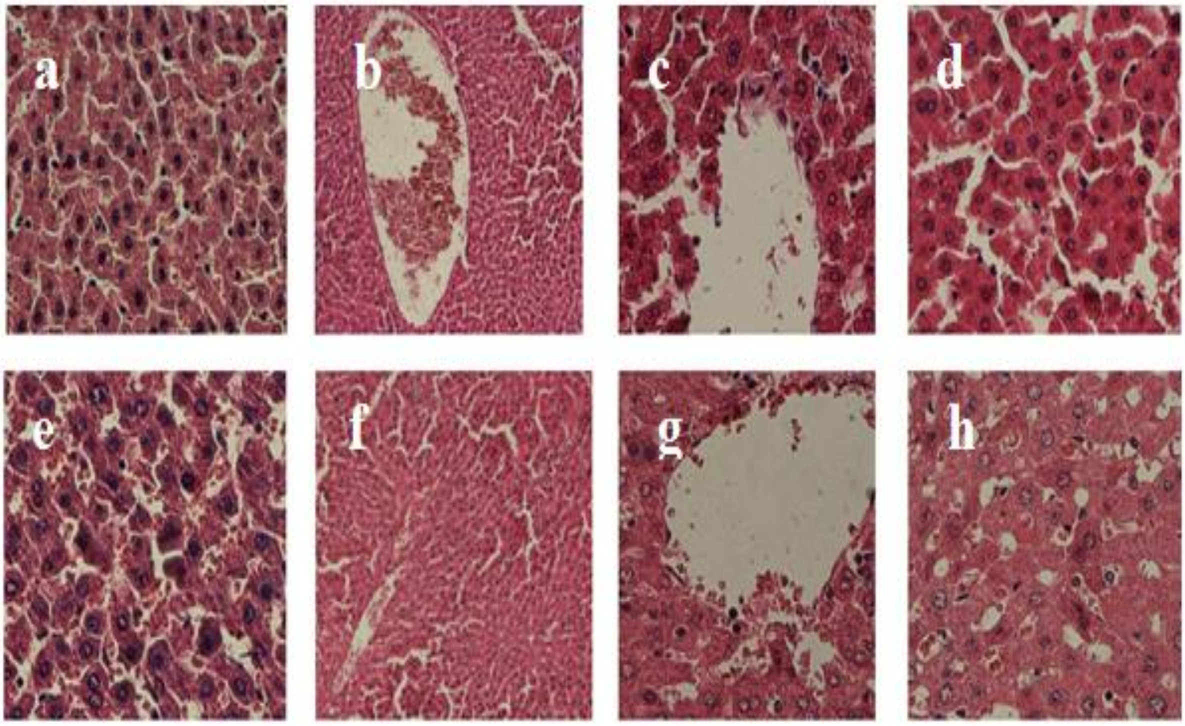

Fig. 3. Liver tissue sections treated with chemical (a, c, and d, X=400, b, X=100) compared with the rat's liver tissue sections treated green synthesized nanoparticles (e, g, and h, X=400, f, X=100) by hematoxylin-eosin staining (h, e, X=100). Lysis of hepatocytes and release of nuclei, nuclear atrophy, disorder and destruction of hepatocyte cords, disorder and dilation of sinusoids, venous congestion, and destruction of the venous wall is very intensive in treated groups treated with chemical nanoparticles relative to the green synthesized nanoparticles treatment groups.

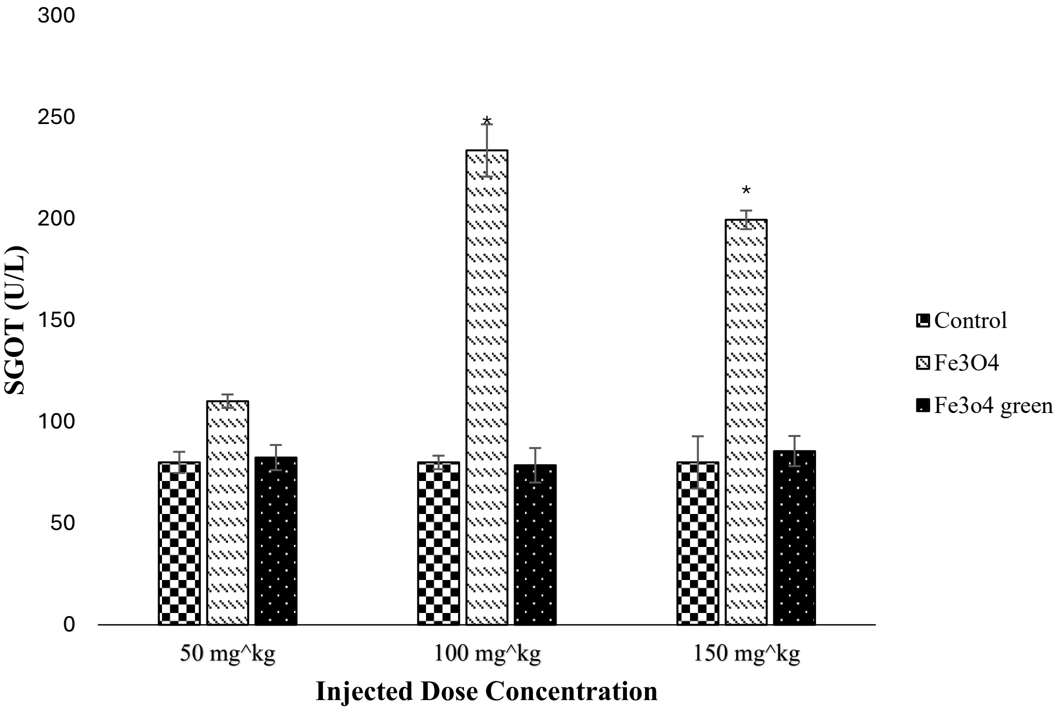

Fig. 4. SGOT levels in the treated rats.

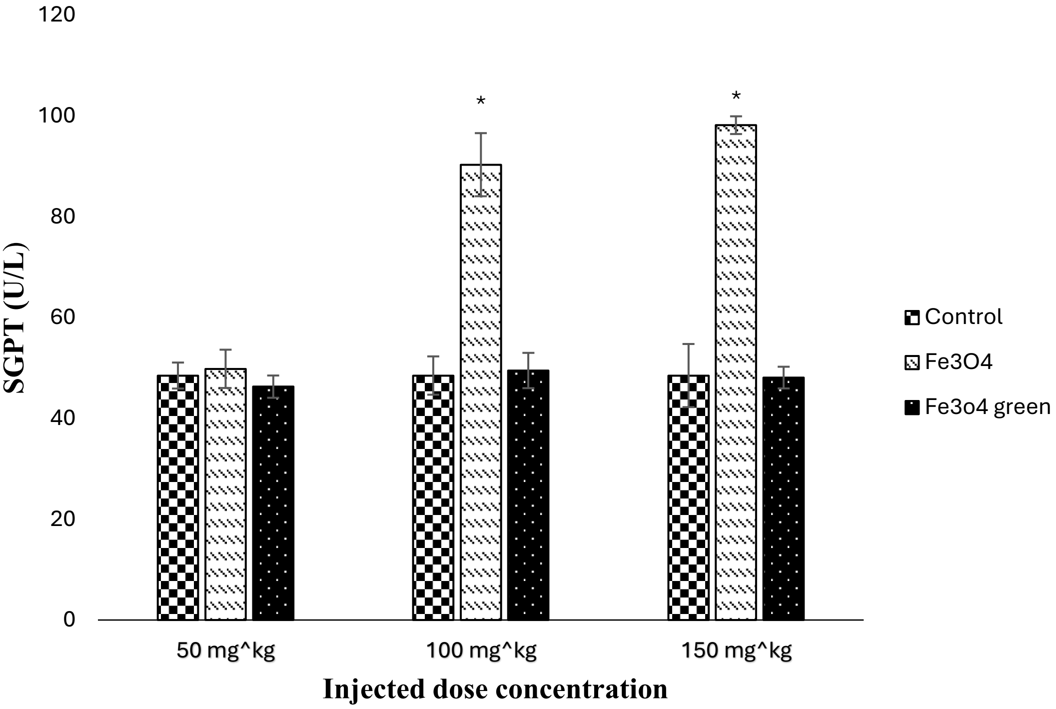

Fig. 5. SGPT levels in the treated rats.

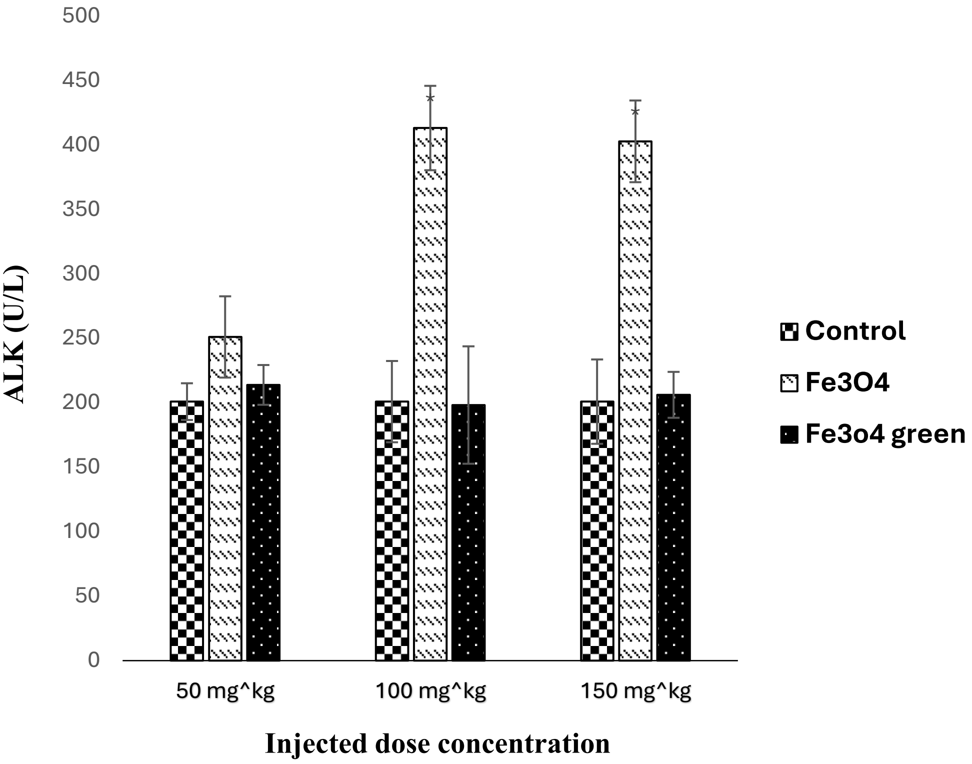

Fig. 6. ALK levels in the treated rats.

Gene expression

RNA extraction and real time RT-PCR analysis

Total RNA was extracted by using RNX plus solution and subjected to agarose gel electrophoresis (Fig. 7). 28S and 18S rRNAs show an optimal quality of the extracted RNA.

Figs. 8 and 9 is the statistical analysis of *GR* and *MT1* gene expression. As mentioned in this study, the expression changes of *Gr gene* as an antioxidant molecule and *MT1*gene as metal balance regulator in liver were measured by the $2^{-\Delta\Delta Ct}$ method. Using SPSS software ver. 18 and performing the statistical independent t-test, the research hypothesis was tested and the results are presented by GraphPad prism software. The distribution of data for the results of gene expression between control group and the rats treated with nanoparticles was performed by KS test.

Metallothioneins are essential in regulating metal homeostasis and controlling the physiological toxicity of heavy metals, DNA damage and oxidative stress [10, 11]. In living organisms, MT1 functions as an antioxidant protein and a metal carrier to maintain physiological balance and prevent damage from metal overload. Several agents, including heavy metals, antioxidants, alkylating agents, glucocorticoids, cytokines, and lipopolysaccharides, can stimulate MT1 expression to exert several immunomodulatory effects. MTs protect organisms against oxidative stress by scavenging hydroxyl radicals and superoxide radicals [24]. Glutathione synthesis occurs exclusively in liver cells. Micronutrients such as vitamin E and C and thiol-rich proteins such as metallothionein and ubiquinone are only some of the mechanisms that the liver uses to resist oxidative stress [12, 13]. Oxidative stress occurs when reactive oxygen species (ROS) are produced at a rate higher than the antioxidant capacity of living organisms. Measurement of oxidation products can be used to determine oxidative stress because most oxidants have very short half-lives [14]. Arial et al. found that the evaluation of the expression and function of metal binding to MTs may be important for analyzing the biodegradation of Me-NPs. MTs as highly reactive thiols can also play a role in inhibiting reactive oxygen species (ROS) caused by Me-NPs. Therefore, metal ion binding to metallothioneins leads to a change from an antioxidant function to a metal ion buffer/ chaperone [25]. Also, Dai et al showed that although metal ion regulation of MT expression has been reported in several studies, the expression of MT1 creates a high capacity to bind these heavy metal ions in vivo and in vitro, and thus the detoxification process begins [9].

In our research, the results showed that MT1 gene expression in mice treated with Fe_3O_4 nanoparticles synthesized by the green method was more significant compared to mice treated with chemical nanoparticles, and a high level of MT1 gene expression was observed in green tea nanoparticles groups. Also, low concentrations of green nanoparticles in treated mice reduced GR gene expression compared to groups treated with Fe_3O_4 chemical nanoparticles. The reason for these changes is probably due to the antioxidant property of green tea, which prevented the destructive effects of the magnetic fields of iron oxide nanoparticles and exerted its antiparamagnetic effects on the expression of the studied genes.

CONCLUSION

This study was conducted in order to compare the effect of iron oxide nanoparticles synthesized by green method and concentrated nanoparticles by chemical method on functional indices of rat liver. The results of this study showed that despite the increase in the size of the nanoparticles due to the coating, this increase in size is not enough to exceed the critical size limit (30 nm for iron oxide). Iron oxide nanoparticles synthesized by the green method prevented the increase in the activity of liver enzymes in mice and had a protective effect. Chitosan coating on iron oxide nanoparticles also helped to reduce the toxic effects of nanoparticles. In the group treated with nanoparticles coated with green tea, compared to the control group and the groups treated with uncoated nanoparticles, most of the changes were decreasing and sometimes increasing, but these changes were not statistically significant. Due to the antioxidant property of nanoparticles synthesized by the green method, MT1 gene expression was increased in the groups treated with this nanoparticle, and GR gene expression was decreased in the same groups compared to the control group and the group treated with chemical nanoparticles. Probably, the short-term use of chitosan-coated iron oxide nanoparticles in biological and medical cases does not cause special toxicity in the body. Therefore, the results obtained from the present research can be the basis for future research in the direction of using nanoparticles synthesized in a green way, with less toxicity for pharmaceutical and medical purposes.

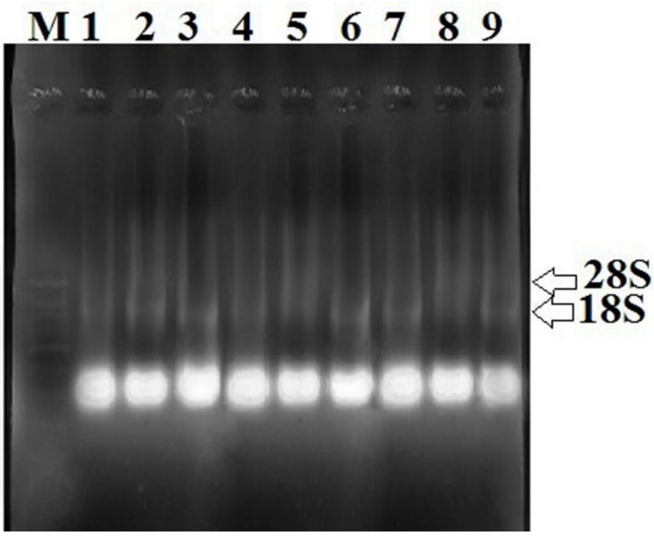

Fig. 7. Qualification of the extracted RNA. 28s and 18s rRNA shows an optimal quality of the extracted RNA. Green viewer-stained 1% agarose gel. M: 100bp DNA size marker.

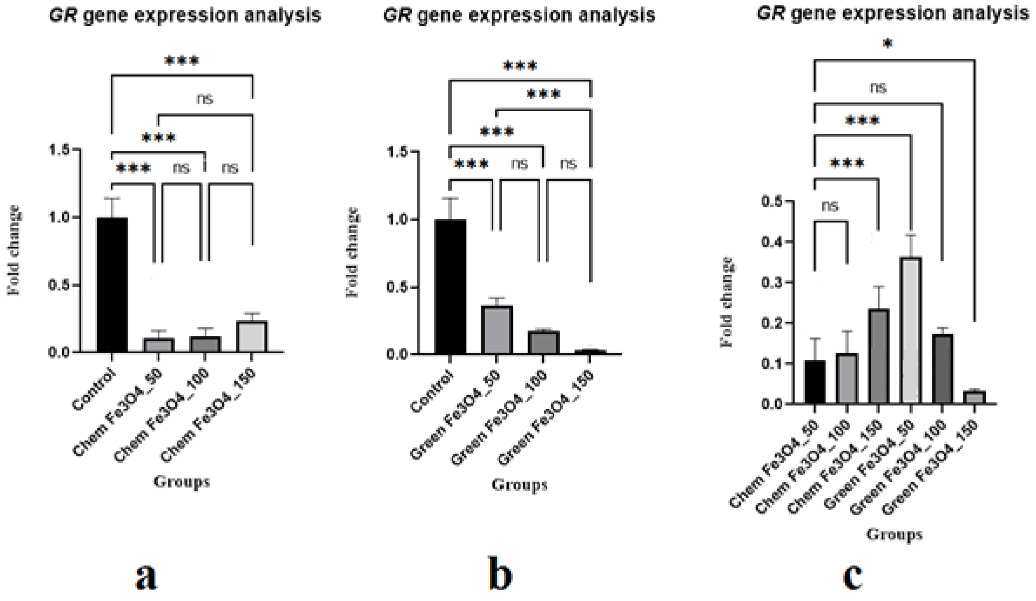

Fig. 8. One-way ANOVA analysis between the chemical Fe_3O_4 nanoparticles treated rat *GR* gene expression compared with the rat treated by green tea nanoparticles. a. *GR* gene expression changes between the treatment groups with different concentrations of chemical nanoparticles were not significant, but a significant decrease was observed between the treatment groups and the control group. b. significant decrease between the control group and green nanoparticle treated groups in the *GR* gene expression. Comparison between the chemical and green synthesized nanoparticle treated groups. Decrease in the *GR* gene expression in the green treated groups is more considerable ($P \leq 0.05$, CI: 95%).

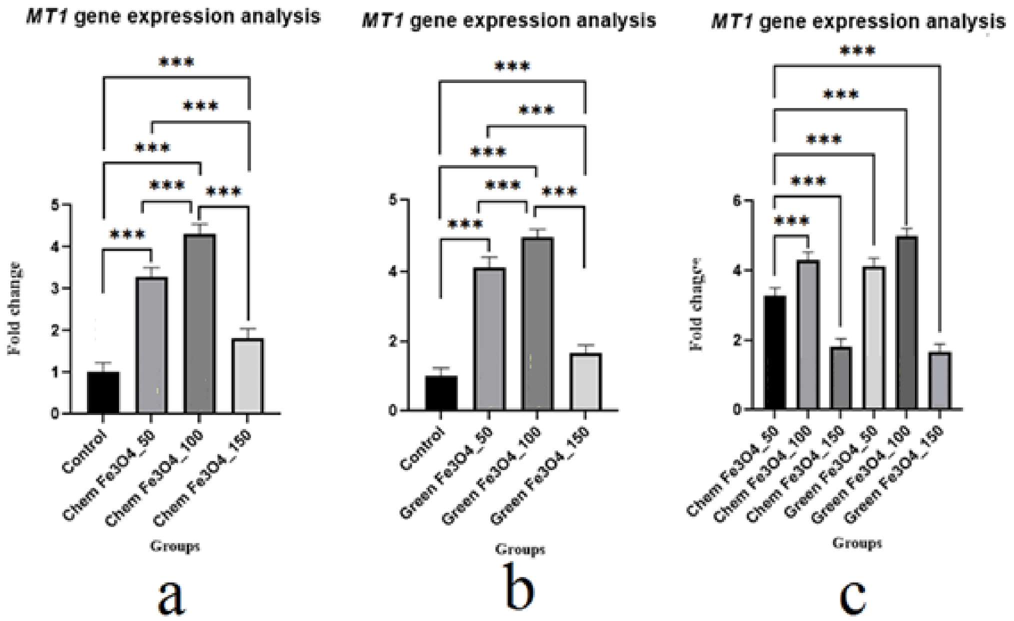

Fig. 9. One-way ANOVA analysis between the chemical Fe_3O_4 nanoparticles treated rat *MT1* gene expression compared with the rat treated by green tea nanoparticles. Significant variance was observed between the green group and the chemical ones. Elevated level of the *MT1* gene expression was observed in the green tea nanoparticle groups (P ≤ 0.05, CI=95%).

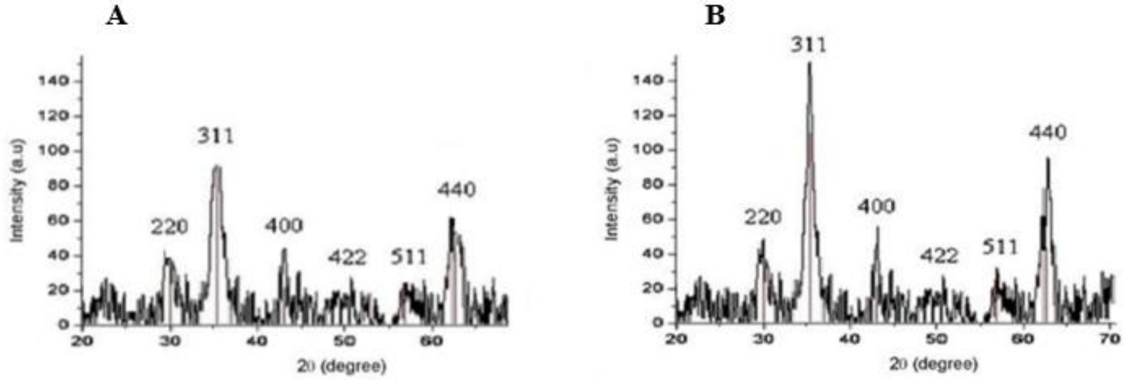

Fig. 10. XRD of Fe_3O_4 nanoparticles. A. X-ray diffraction image of chitosan coated, B. X-ray diffraction image of Fe_3O_4 nanoparticles

CONFLICT OF INTEREST

The authors declare that there is no conflict of interest regarding the publication of this manuscript.

REFERENCES

[1] Yew YP, Shameli K, Miyake M, Khairudin NB, Mohamad SE, Naiki T, Lee KX. Green biosynthesis of superparamagnetic magnetite Fe_3O_4 nanoparticles and biomedical applications in targeted anticancer drug delivery system: A review. Arabian Journal of Chemistry. 2020;13(1):2287-308.

[2] Singh J, Dutta T, Kim K-H, Rawat M, Samddar P, Kumar P. 'Green' synthesis of metals and their oxide nanoparticles: applications for environmental remediation. Journal of Nanobiotechnology. 2018;16:1-24.

[3] Ijaz I, Gilani E, Nazir A, Bukhari A. Detail review on chemical, physical and green synthesis, classification, characterizations and applications of nanoparticles. Green Chemistry Letters. 2020;13:223-45.

[4] Nguyen MD, Tran HV, Xu S, Lee TR. Fe_3O_4 nanoparticles: structures, synthesis, magnetic properties, surface functionalization, and emerging applications. Applied Sciences. 2021;11(23):11301.

[5] Saeed RM, Dmour I, Taha MO. Stable chitosan-based nanoparticles using polyphosphoric acid or hexametaphosphate for tandem ionotropic/covalent crosslinking and subsequent investigation as novel vehicles for drug delivery. Frontiers in Bioengineering and Biotechnology. 2020;8:4.

[6] Adeyemi OS, Adewumi I. Biochemical evaluation of silver nanoparticles in wistar rats. International Scholarly Research Notices. 2014;2014(1):196091.

[7] Ruttkay-Nedecky B, Nejdl L, Gumulec J, Zitka O, Masarik M, Eckschlager T, Stiborova M, Adam V, Kizek R. The role of metallothionein in oxidative stress. International Journal of Molecular Sciences. 2013;14(3):6044-66.

[8] Masiulionytė B, Valiulytė I, Tamašauskas A, Skiriutė D. Metallothionein genes are highly expressed in malignant astrocytomas and associated with patient survival. Scientific Reports. 2019;9:1-7.

[9] Dai H, Wang L, Li L, Huang Z, Ye L. Metallothionein 1: A New spotlight on inflammatory diseases. Frontiers in Immunology. 2021;12:739918.

[10] Wang W-C, Mao H, Ma D-D, Yang W-X. Characteristics, functions, and applications of metallothionein in aquatic vertebrates. Frontiers in Marine Science. 2014;1:34.

[11] Kedrowski BL, Gutow JH, Stock G, Smith M, Jordan C, Masterson DS. Glutathione reductase activity with an oxidized methylated glutathione analog. Journal of Enzyme Inhibition and Medicinal Chemistry. 2014;29(4):491-4.

[12] Vairetti M, Di Pasqua L.G, Cagna M, Richelmi P, Ferrigno A, Berardo C. Changes in glutathione content in liver diseases: An update. Antioxidants 2021;10:364.

[13] Pizzorno J. Glutathione!. Integrative Medicine: A Clinician's Journal. 2014;13(1):8.

[14] Csiszár J, Horváth E, Bela K, Gallé Á. Glutathione-related enzyme system: glutathione reductase (GR), glutathione transferases (GSTs) and glutathione peroxidases (GPXs). Redox state as a central regulator of plant-cell stress responses. 2016:137-58.

[15] Mao C, Yuan JQ, Lv YB, Gao X, Yin ZX, Kraus VB, Luo JS, Chei CL, Matchar DB, Zeng Y, Shi XM. Associations between superoxide dismutase, malondialdehyde and all-cause mortality in older adults: a community-based cohort study. BMC Geriatrics. 2019;19:1-9.

[16] Bhuiyan MS, Miah MY, Paul SC, Aka TD, Saha O, Rahaman MM, Sharif MJ, Habiba O, Ashaduzzaman M. Green synthesis of iron oxide nanoparticle using Carica papaya leaf extract: application for photocatalytic degradation of remazol yellow RR dye and antibacterial activity. Heliyon. 2020;6(8).

[17] Yusefi M, Shameli K, Su Yee O, Teow SY, Hedayatnasab Z, Jahangirian H, Webster TJ, Kuča K. Green synthesis of Fe3O4 nanoparticles stabilized by a

Garcinia mangostana fruit peel extract for hyperthermia and anticancer activities. International Journal of Nanomedicine. 2021;29:2515-32.

[18] Al-Karagoly H, Rhyaf A, Naji H, Albukhaty S, AlMalki FA, Alyamani AA, Albaqami J, Aloufi S. Green synthesis, characterization, cytotoxicity, and antimicrobial activity of iron oxide nanoparticles using Nigella sativa seed extract. Green Processing and Synthesis. 2022;11(1):254-65.

[19] Albukhaty S, Naderi-Manesh H, Tiraihi T, Sakhi Jabir M. Poly-l-lysine-coated superparamagnetic nanoparticles: a novel method for the transfection of pro-BDNF into neural stem cells. Artificial Cells, Nanomedicine, and Biotechnology. 2018;46(sup3):125-32.

[20] Akhondipour M, Faghihi Zarandi A, Amirri A, Gommnami N, Vazirinejad R. Studying the toxicity of molybdenum trioxide nanoparticles in male Wister rats. Journal of Occupational Health and Epidemiology. 2018;7(4):233-9.

[21] Vasantharaja D, Ramalingam V, Reddy GA. Oral toxic exposure of titanium dioxide nanoparticles on serum biochemical changes in adult male Wistar rats. Nanomedicine Journal. 2015;2(1).

[22] Ćurlin M, Barbir R, Dabelić S, Ljubojević M, Goessler W, Micek V, Žuntar I, Pavić M, Božičević L, Pavičić I, Vinković Vrček I. Sex affects the response of Wistar rats to polyvinyl pyrrolidone (PVP)-coated silver nanoparticles in an oral 28 days repeated dose toxicity study. Particle and Fibre Toxicology. 2021;18:1-6.

[23] Zare S, Hayatgeibi H, Alivandi S, Ebadi AG. Effects of whole-body magnetic field on changes of glucose and cortisol hormone in guinea pigs. American Journal of Biochemistry and Biotechnology. 2005;1(4):217-9.

[24] Sharifi-Rad J, Quispe C, Butnariu M, Rotariu LS, Sytar O, Sestito S, Rapposelli S, Akram M, Iqbal M, Krishna A, Kumar NV. Chitosan nanoparticles as a promising tool in nanomedicine with particular emphasis on oncological treatment. Cancer Cell International. 2021;21(1):318.

[25] Aryal BP, Neupane KP, Sandros MG, Benson DE. Metallothioneins initiate semiconducting nanoparticle cellular toxicity. Small. 2006;2(10):1159-63.

J. Nanoanalysis., 11(1): 662-667, Winter 2024

Investigation of the mechanical and thermo- electrical properties of nylon filaments reinforced with nanoparticle

Farshad Farahbod[1*], Abuzar Shakeri[2], Seyede Nasrin Hosseinimotlagh[3]

[1] *Department of Chemical Engineering, Fir.C., Islamic Azad University, Firoozabad, Iran*
[2,3] *Department of Physics, Shi.C., Islamic Azad University, Shiraz, Iran*

ARTICLE INFO

Article History:

Received 2024-12-13
Accepted 2025s-04-11
Published 2024-02-15

Keywords:

Thermal properties,

Stress properties,

Nylon,

ZnO nano particles.

ABSTRACT

Incorporating zinc oxide nanoparticles (ZnONPs) into nylon significantly alters its mechanical and thermal characteristics. Nanocomposites with 0, 1, and 2 wt% ZnONPs were created through a two-step process of dry mixing and single-screw extrusion. Tensile testing (at strain rates from 0.02 to 2) showed that both neat nylon and the nanocomposites exhibit strain rate hardening, with ultimate tensile strength (UTS), yield strength, and tensile modulus all influenced by strain rate. Critically, adding ZnONPs improved these mechanical properties, with the 2 wt% nanocomposite showing a 45% higher tensile modulus and a 26% higher UTS than neat nylon. Thermal stability was enhanced by the nanoparticles, as confirmed by thermogravimetric analysis (TGA), and differential scanning calorimetry (DSC) revealed a slight increase in glass transition temperature. A constitutive model effectively captured the nonlinear, strain rate-dependent behavior of both the base polymer and the nanocomposites. While thermal conductivity and diffusivity showed complex trends with increasing ZnONP content, the 2 wt% sample exhibited the highest conductivity and lowest diffusivity. Finally, the dielectric constant increased, and resistivity decreased, with higher ZnONP loadings.

How to cite this article
Farahbod F., Shakeri A., Hosseinimotlagh S. N., Investigation of the mechanical and thermo- electrical properties of nylon filaments reinforced with nanoparticle. J. Nanoanalysis., 2024; 11(1): 662-667.

*Corresponding Author Email: *Farshad.Farahbod@iau.ac.ir*

INTRODUCTION

Nylon 6, a versatile engineering thermoplastic, finds broad application due to its favorable combination of mechanical properties and chemical resistance [1]. However, conventional reinforcement strategies often require substantial filler content to achieve notable property enhancements, which can compromise the inherent advantages of the polymer [2]. Nanocomposites, leveraging small amounts of nanoparticles, offer a compelling alternative [3]. Zinc oxide nanoparticles (ZnONPs) are particularly attractive for reinforcing polymers due to their potential to improve mechanical performance [4]. This research investigates how incorporating ZnONPs affects the mechanical and thermal properties of nylon filaments [5]. Mechanical behavior is assessed through tensile testing, while Scanning Electron Microscopy (SEM) is employed to examine fracture surfaces and understand failure mechanisms [6]. Finally, experimental data informs the development of a constitutive model that describes the tensile behavior of the resulting nylon-ZnO nanocomposites [7]. Nanoparticle reinforcement offers a powerful method to tailor and enhance the properties of nylon fibers [8]. The following summarizes the primary impacts of incorporating nanoparticles into this material:

Incorporating nanoparticles into nylon fibers offers a pathway to significantly tailor and improve material performance [9]. These reinforcements impact mechanical, thermal, and other functional characteristics [10]. Mechanically, nanoparticles can increase strength and stiffness by acting as reinforcing agents within the nylon matrix, leading to improvements in tensile strength, yield strength, and modulus [11]. Some nanoparticles also enhance toughness, improving resistance to cracking and fracture, and reduce creep by hindering polymer chain movement under sustained stress [12]. Thermally, certain nanoparticles can improve thermal stability, increasing resistance to high-temperature degradation, and elevate the glass transition temperature (Tg), allowing the material to maintain stiffness and strength at higher temperatures [13]. Beyond these, nanoparticles can impart additional functionalities [14]. For example, titanium dioxide (TiO_2) or zinc oxide (ZnO) can provide UV protection, while silver nanoparticles (AgNPs) can introduce antimicrobial properties. Conductive nanoparticles, like carbon nanotubes or graphene, can even render nylon fibers electrically conductive. The degree of property modification is influenced by several key factors: the specific type of nanoparticle used, its concentration within the nylon matrix, the uniformity of nanoparticle dispersion (agglomeration can create weaknesses), and the processing technique employed (e.g., melt mixing, solution blending, or in-situ polymerization) [15]. This study focuses specifically on the tensile mechanical properties of nylon filaments reinforced with zinc oxide nanoparticles.

EXPERIMENTAL

Determining the novelty of a manuscript concerning the mechanical and tensile properties of nanoparticle-reinforced nylon filaments requires a thorough literature review. However, several potential areas of innovation can distinguish such work. These include developing a novel nanoparticle incorporation method (e.g., unique surface treatment, mixing/extrusion technique, or functionalization for enhanced nylon interaction), exploring less common nanoparticle types or combinations (with strong justification and investigation of synergistic effects), or focusing on a specific, under-studied mechanical property (e.g., fatigue, impact, creep, or wear) with detailed analysis as a function of concentration and processing. Critically, going beyond simply reporting property improvements and establishing detailed structure-property relationships via advanced characterization (e.g., TEM, SAXS) to analyze nanoparticle dispersion, interfacial bonding, and microstructural changes is essential for demonstrating originality. Other avenues for innovation include developing new theoretical models or employing advanced simulations (e.g., nanoscale finite element analysis) to understand deformation mechanisms, systematically optimizing processing parameters (e.g., extrusion temperature, screw speed, drawing ratio) using a design of experiments approach, or focusing on a specific application and demonstrating how nanoparticle incorporation enhances performance in that context. Ultimately, manuscript originality hinges on demonstrating something new and non-obvious in the materials, processing, characterization, modeling, or application, with a clear articulation of the research gap and the work's contribution.

ZnONP Characterization

Zinc oxide nanoparticles (ZnONPs) exhibited a hexagonal wurtzite structure (Figure 1). As a semiconductor with a bandgap of approximately 3.22 eV, ZnO interacts with UV-visible light through electronic excitation between its conduction and valence bands, a phenomenon observed in other ZnO-containing materials as well [32, 33]. While ZnONPs have been shown to exhibit some agglomeration within material matrices, this study also investigated the impact of ZnO addition on the mechanical and optical properties of LDPE thin films. Young's modulus, strength, and elongation at break were determined from stress-strain curves. The presence of ZnO significantly altered these properties. The improved strain at fracture, regardless of ZnO concentration, suggests a mechanism involving surface adhesion and interaction between the ZnONPs and the LDPE matrix [33].

Materials

High-purity, sub-50 nm spherical zinc oxide nanoparticles (ZnONPs) were synthesized via a sol-gel method. The matrix material was a high-performance polyamide. 6 resins (Nylon P1011F) specifically designed for stable high-speed extrusion. This resin, according to supplier specifications, has a melting temperature range of 215-225 °C, a density of 1.09-1.19 g/cm³, and typical mechanical properties including 70-80 MPa tensile strength, 100% tensile elongation at break, and 1-3 GPa tensile modulus.

Research process

Nylon powder and precisely weighed ZnONPs were dry-mixed for one hour using a high-speed mechanical blender (22,000 rpm), with 10-minute cooling intervals to prevent thermal degradation. A single-screw extruder (19 mm screw diameter, five heating zones) melted and mixed the nylon and ZnONPs. The barrel temperature profile consisted of three progressively increasing zones (222 °C, 232 °C, and 242 °C) followed by two zones at 242 °C near the die, ensuring gradual melting and effective mixing. The homogenized nylon-ZnO nanocomposite was then extruded through a die plate, heated steel tube, and die (Figure 2).

Composite filaments were produced via continuous extrusion under controlled tension. The extruded material then passed through a godet wheel and heating zone before being wound onto a rotating bobbin at 70 rpm (Figure 3).

Testing

A START data acquisition system was used for all experiments. Three sample groups were analyzed: neat nylon filaments, and composite filaments with 1 wt% and 2 wt% ZnO nanoparticles. At least ten replicates per group were tested for statistical significance. FE-SEM samples were sectioned and argon plasma etched (TEK Vac Industries, Inc.) for one hour at 600 mTorr and 2.5 W/cm² power density.

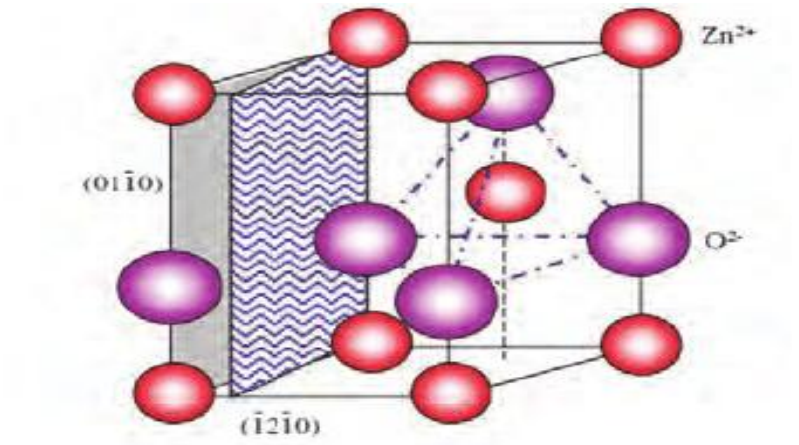

Figure 1. The wurtzite structure model of ZnO.

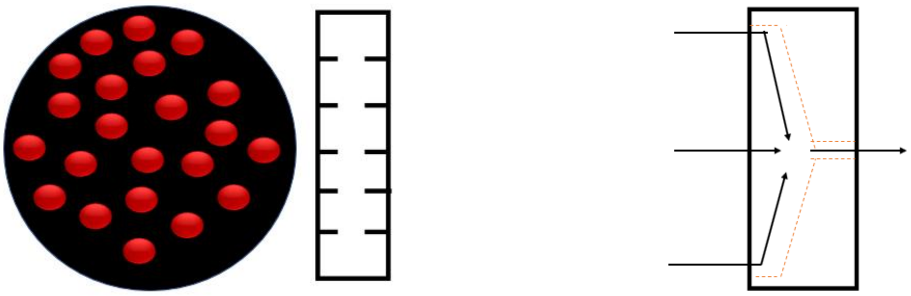

(a). (b).

Figure 2. Extruder die geometry. (a) Top view of circular die plate. (b) Side view of die profile.

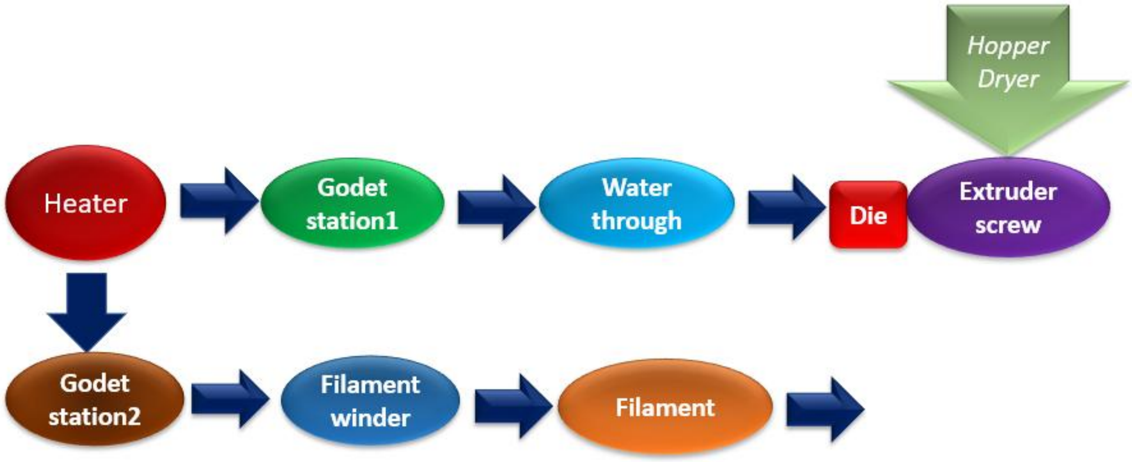

Figure 3. Schematic of the PAN-based carbon fiber spinning process.

RESULTS AND DISCUSSIONS

Thermal response

Thermogravimetric analysis (TGA) curves, shown in Figure 4a, depict the mass loss of neat nylon filaments and composite filaments with 1 wt% and 2 wt% ZnONP loadings as a function of temperature. Derivative thermogravimetric (DTG) curves (Figure 4b) were analyzed to determine the decomposition temperature. These curves, representing the rate of mass loss versus temperature, show peaks corresponding to the maximum degradation rates.

Derivative thermogravimetric (DTG) analysis (Figure 5b) revealed decomposition temperatures of 445°C for neat nylon, increasing to 455°C and 456°C with the addition of 1 wt% and 2 wt% ZnO nanoparticles, respectively. The glass transition temperature (Tg) (Figure 5a) also increased, from 49°C for neat nylon to 55°C and 56°C for the 1 wt% and 2 wt% nanocomposites, respectively. This elevation in Tg indicates that the incorporation of ZnO nanoparticles restricts the movement of nylon polymer chain segments.

Figure 5b shows that both 1 wt% and 2 wt% ZnO-nylon composites exhibit a higher crystallization temperature (Tc) of 193°C compared to 190°C for the neat nylon control. Crystallinity also increased from approximately 24% in the neat nylon to around 28% in both nanocomposites. These results indicate that the incorporated ZnO nanoparticles act as nucleating agents, promoting earlier crystallization and a higher degree of crystallinity. However, it is possible that higher nanoparticle concentrations could alter crystallization kinetics and potentially slow down the crystallization rate.

While the melting temperature (Tm) remained consistent at approximately 224°C across all samples (Table 1), the nanocomposite filaments exhibited significantly higher crystallinity and heat of fusion compared to the neat nylon control.

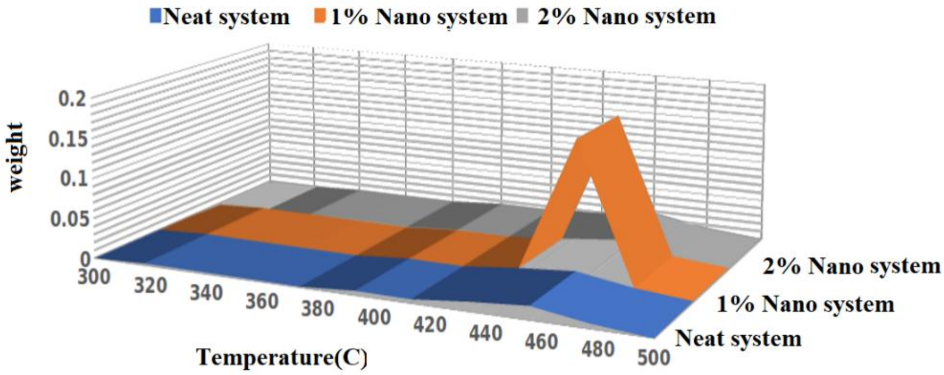

(a).

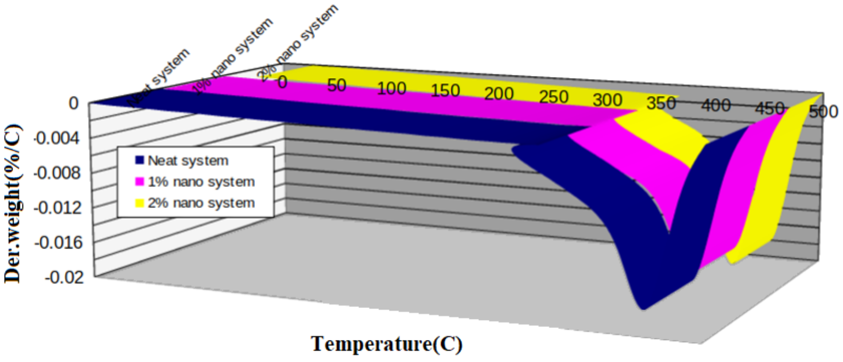

(b).

Figure 4. Thermogravimetric Analysis (TGA) Curves for neat nylon and nanocomposite filaments (a, b).

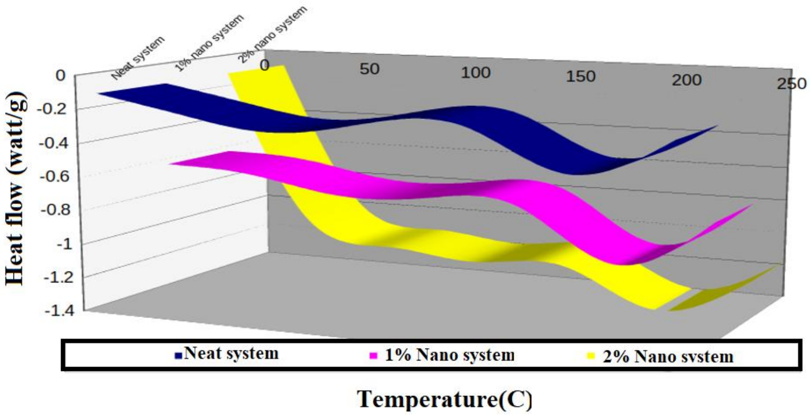

(a).

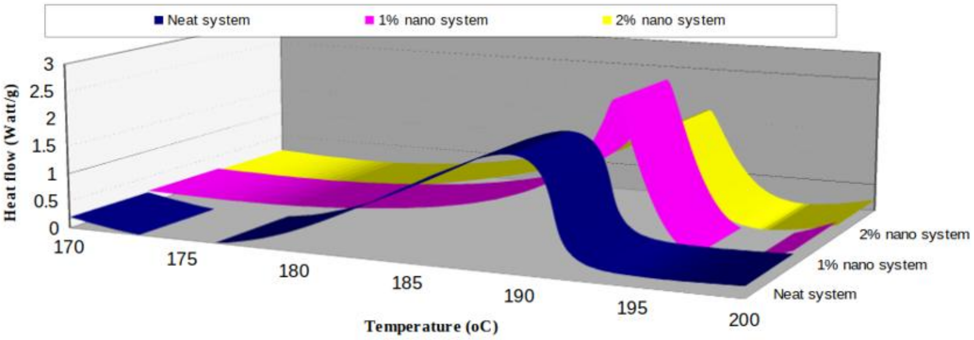

(b).

Figure 5. DSC curves for neat nylon and nanocomposite filaments (a, b).

Table 1. Differential scanning calorimetry.

Samples	T_g (°C)	T_m (°C)	ΔH_f (Joule/g)	**Crystallinity (%)**
Neat nylon	49	224	52.24	24
1%ZnO–nylon	55	222	62.15	27
2%ZnO–nylon	56	223	64.2	28

Stress–strain diagrams

Tensile stress-strain (TSS) curves for neat nylon and the nylon nanocomposites are shown in Figures 5-7. Both materials exhibit nonlinear stress-strain behavior, including strain hardening, even before yielding. Table 2 summarizes the tensile properties under the various test conditions.

The stress-strain behavior of the materials is presented in Figures 6-8. For all materials tested, modulus increased with increasing strain rate. The parallel curves in the strain hardening region indicated that the hardening modulus is relatively insensitive to strain rate within the tested range.

At a strain rate of 2 min^{-1}, the 2 wt% ZnO nanocomposite shows superior mechanical performance compared to neat nylon, exhibiting a 23.4% increase in tensile modulus (Figure 9). While ZnONP incorporation significantly improves nylon mechanical properties, its impact on ductility is minimal, with comparable strain at break observed across all samples.

Sensitivity of strain rate

Neat nylon and its nanocomposites both display strain rate-dependent mechanical behavior, as shown in Table 2 and Figures 5-7. This characteristic is often described as strain rate sensitivity. Figure 10 shows how tensile properties vary with strain rate. The linear relationship between strength and ln ($\acute{\varepsilon}$) suggests power-law dependence. The slopes of these linear fits quantify the strain rate sensitivity of each material. The following equations describe the observed correlations between yield strength, tensile strength, and strain rate.

$$\sigma_b = \sigma_{b0}\left(1 + \lambda_1 \ln \frac{\dot{\varepsilon}}{\dot{\varepsilon}_b}\right) \qquad (1)$$

$$\sigma_Y = \sigma_{Y0}\left(1 + \lambda_2 \ln \frac{\dot{\varepsilon}}{\dot{\varepsilon}_b}\right) \qquad (2)$$

In Equations (1) and (2), σb_0 and σY_0 represent the tensile strength and yield strength, respectively, at a reference strain rate, $\dot{\varepsilon}_0$. The coefficients λ_1 and λ_2 (defined in Equation (3)) quantify the strain rate sensitivity of each material.

$$\lambda_{12} = \frac{\partial(\sigma_b, \sigma_Y)}{\partial \ln \dot{\varepsilon}} \qquad (3)$$

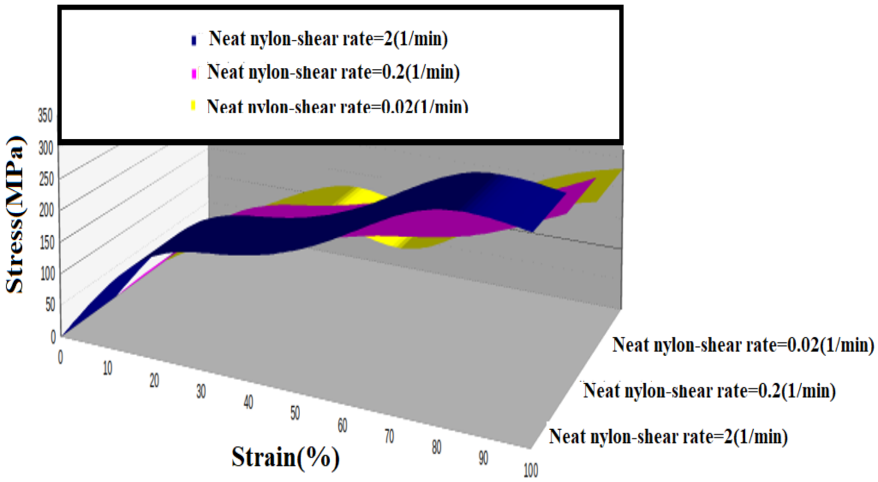

Figure 6. TSS curves for neat nylon at various strain rates.

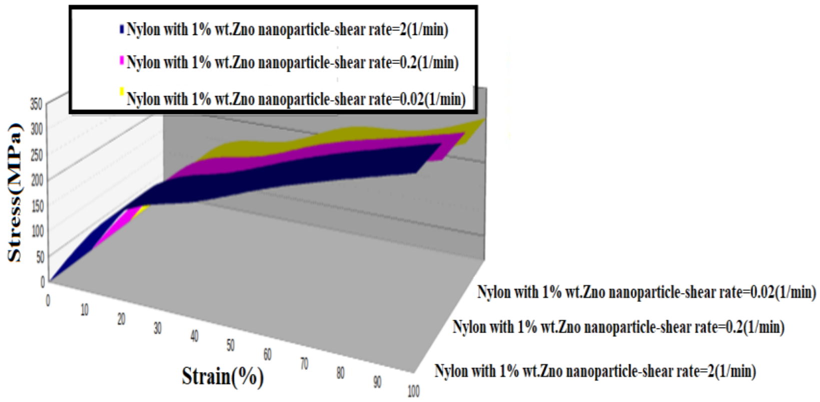

Figure 7. TSS curves for one wt.% ZnO/nylon Composite at various strain Rates.

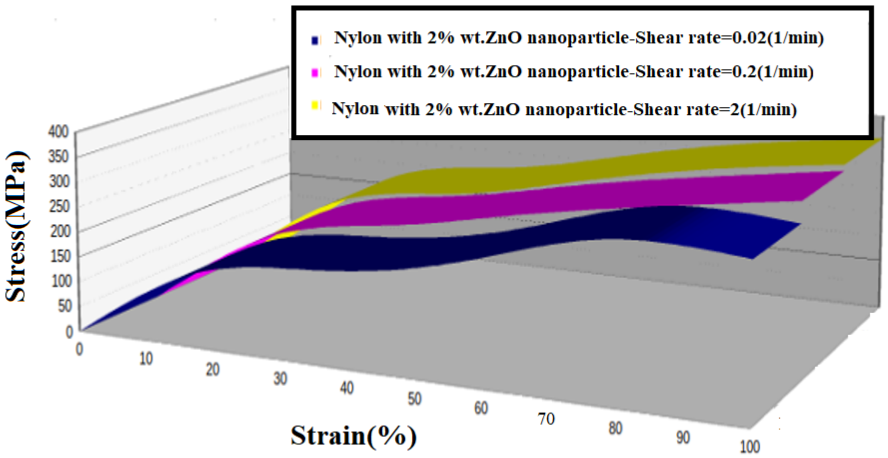

Figure 8. TSS curves for two wt. % ZnO/nylon composite at various strain rates.

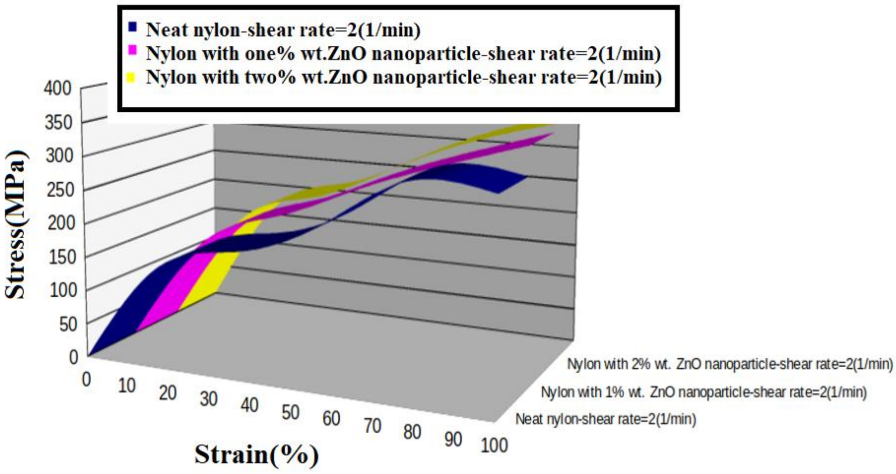

Figure 9. TSS curves for neat nylon and nanocomposite filaments.

Table 2. Mechanical characteristics of neat nylon and nanocomposites.

Material	Strain rate (1/min)	*E* (GPa)	σ_Y (MPa)	Hardening modulus (MPa)	UTS (MPa)
Neat Nylon	0.02	1.30	68.4	174	243
Neat Nylon	0.2	1.47	83.4	177	262
Neat Nylon	2	1.76	125	176	293
Nylon with 1 wt.% ZnO	0.02	1.65	96.7	206	287
Nylon with 1 wt.% nanoparticle	0.2	1.88	117	205	309
Nylon with 1 wt.% ZnO	2	2.08	129	204	311
Nylon with 2 wt.% ZnO	0.02	1.88	120	219	306

Nylon with 2 wt.% ZnO	0.2	1.95	125	215	313
Nylon with 2 wt.% ZnO	2	2.16	138	219	342

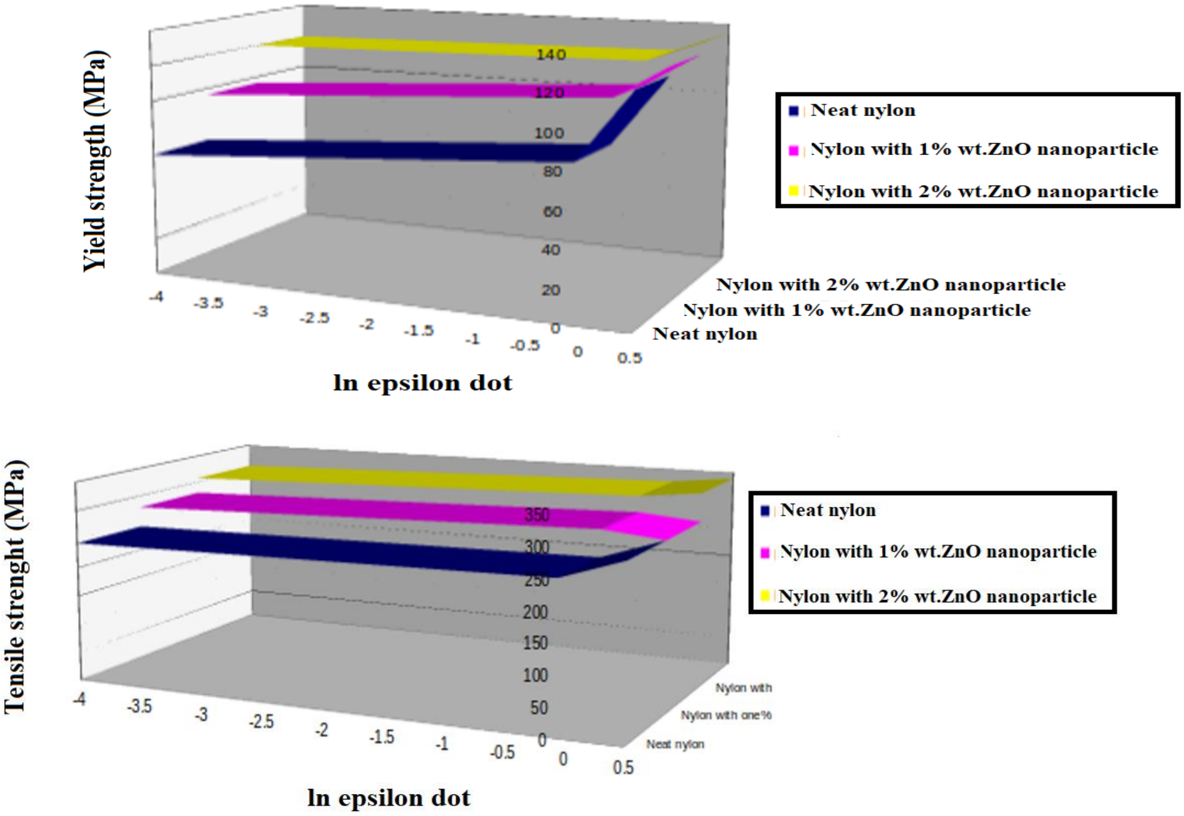

Figure 10. Yield and tensile strength variation with strain rate (ln $\dot{\varepsilon}$).

Least-squares regression analysis of the experimental data yielded the strain rate strengthening coefficients, λ_1 and λ_2, which are presented in Table 3. These results suggest that nanoparticles restrict polymer chain mobility at higher strain rates (Equation 4).

$$V = \frac{RT}{\lambda_2} \tag{4}$$

Activation volumes (ΔV), which reflect the energy barrier to atomic-level deformation, were calculated using Equation (4) and incorporating the gas constant (R), absolute temperature (T), and the strain rate sensitivity coefficient (λ). These calculated values for both neat nylon and the nanocomposites are presented in Table 3.

As shown, Figure 11 evaluates the effect of nanoparticle content and degree of tension on the viscosity coefficient. In Equation (5), E1 and E2 represent the elastic modulus of the spring in the Maxwell element and the spring in the Kelvin element, respectively, while η is the viscosity coefficient (stress × time). The initial slope of the stress-strain curve can be expressed as shown in Equations (6) and (7).

$$\sigma = \frac{E_1 E_2}{E_1 + E_2}\varepsilon + \frac{E_1^{\,2}\,\dot{\varepsilon}\eta}{(E_1 + E_2)^2}\left[1 - \frac{E_1 + E_2}{\varepsilon}\frac{\varepsilon}{\dot{\varepsilon}}\right] \tag{5}$$

$$\frac{d\sigma}{d\varepsilon} = E_1 \tag{6}$$

$$\frac{d\sigma}{d\varepsilon} = \frac{E_1 E_2}{E_1 + E_2} \tag{7}$$

The viscosity coefficient relationships for pure nylon and nylon containing 1 and 2 weight percent nanoparticles are presented in Table 4.

XRD patterns of ZnONPs were obtained using a Miniflex XRD machine (Rigaku, Japan). The crystalline domain dimension (D) was calculated using Scherrer's equation: $D = {}^{K\lambda}/_{\beta cos\theta}$

where ʎ represents the wavelength of the incident X-ray beam, θ is Bragg's diffraction angle, β is the width of the X-ray pattern line at half-peak height in radians, and the dimensionless shape factor (K) has a normal value of 0.89 but varies depending on the actual crystalline structure. SEM (FEI Company, USA) was used to study the morphology of the materials.

Density of nanocomposites

The theoretical density (ρth) of the nanocomposites is given by:

$\rho_{th} = \rho_f V_f + \rho_m V_m$

Where pf and pm are the density of Zno and matrix, respectively. V_f and V_m represent the volume fractions of ZnO and matrix, respectively. The experimental density (ρex) was calculated using Archimedes' principle and following eq.:

$P_{ex} = {}^{W_{air} p_{liq}}/_{W_{air} - W_{liq}}$

W_{liq} and W_{air} are the weights of samples in liquid medium (ethanol) and air, respectively.

Thermal conductivity test

A Lee's Disc device (George and Griffin™) can be used to calculate the thermal conductivity coefficients of test materials. In this device, heat flows from the heater into each sequentially stacked disc. The temperatures of the three discs (TA, TB, and TC) are determined using internally inserted thermometers. The sample (S) is placed between the discs A and B, while the heater is placed between discs B and C. It is essential to ensure that the surfaces of the copper are clean and in good contact to obtain the best heat transfer. The thermal conductivity value is determined using the following equation:

$$K\left(\frac{T_B - T_A}{d_s}\right) = e\{T_A + \frac{2}{r}\left(d_A + \frac{1}{4}d_s\right)T_A + \frac{1}{2r}d_s T_B\}$$

(8)

Where e denotes the amount of thermal energy that passes through the unit area of the disc material per second (W/m^2.k), and it is estimated from the following equation:

$$IV = \pi r^2 e(T_A + T_B) + 2\pi r e d_A T_A + d_s \frac{1}{2}(T_A + T_B) + d_B T_B + d_C$$

(9)

IV is the thermal energy that passes through the heating coil per unit time; TA, T B, and TC represent the respective disc temperatures; and d and r are the thickness and radius of the disc (mm), respectively. According to ASTM-D150, the specifications for measuring thermal conductivity were a thickness of 6.73 mm and a diameter of 40 mm.

Dielectric property

The device used for measuring the dielectric constant values of the composites was an electrical circuit (connected in series) consisting of a capacitor, a resistor, a coil, a frequency generator, and an ammeter. After placing the sample between the capacitor's plates, the frequency of the power supplier was adjusted until the maximum current value was obtained. The frequency, which reflects the resonance frequency value (fr), was recorded at this maximum value. The fr value was then calculated without a sample (i.e., in the presence of air only). From the relationship, the capacitor's capacity could be determined as: $C =$

$^1/_{4\pi^2 f_r^2 L}$ where L represents the inductance of the coil. The dielectric constant (εr) can be calculated from the equation,$\varepsilon_r = {}^{C}/_{C_0}$ in which Co represents the capacity of the capacitor in the existence of air, while C represents the capacity of the capacitor in the presence of a sample. (See Table.5)

Table 3. Model variables for neat nylon and nanocomposites.

Material	**$\lambda 1$**	**$\lambda 2$**	**V (nm)3**	**η, shear rate=2 (1/min)**	**η, shear rate=0.2 (1/min)**	**η, shear rate=0.02 (1/min)**
Nylon	10.7	12.4	12.4	80	550	4000
One wt.% ZnO	9.12	7.91	7.91	85	700	6000
One wt.% ZnO	7.82	3.78	3.78	90	800	7000

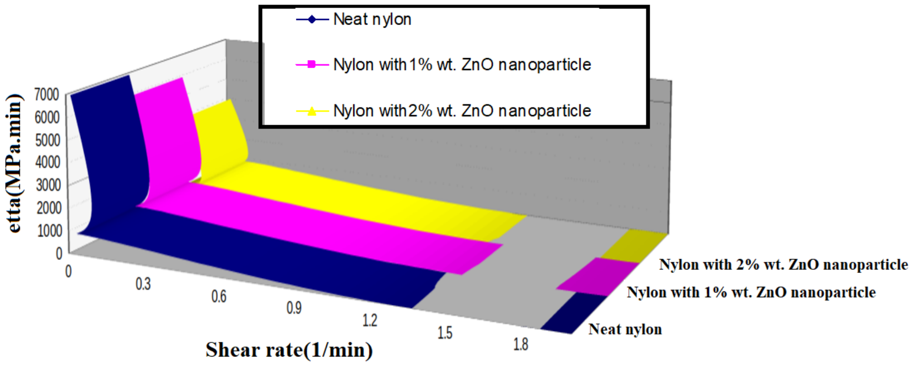

Figure 11. The effect of nanoparticle content and degree of tension on the viscosity coefficient, η.

Table 4. Viscosity coefficient relationships for pure nylon and nylon containing 1 and 2 weight percent nanoparticle

Nylon	$\eta = 143^{.=0.849}\ \varepsilon\ \ (\mathrm{MPa}\times\mathrm{min})$
Nylon containing 1% by weight of nanoparticles	$\eta = 160^{.=0.924}\ \varepsilon\ \ (\mathrm{MPa}\times\mathrm{min})$
Nylon containing 2% by weight of nanoparticles	$\eta = 173^{.=0.945}\ \varepsilon\ \ (\mathrm{MPa}\times\mathrm{min})$

Table5: Experimental values of dielectric constant, resistivity, thermal conductivity of nanocomposites, diffusivity and density of all samples.

Samples	**Dielectric constant**	**Resistivity (Ω.m)*10^{-11}**	**Thermal conductivity of nanocomposites (w/m.C)**	**Diffusivity (w/m^2.C)**	**Density (mg/cm)**

Neat nylon	2.6	3.8	0.31	6.41	1.395
1%ZnO–nylon	4.3	3.3	0.48	6.05	1.409
2%ZnO–nylon	5.4	1.9	0.46	5.78	1.415

CONCLUSION

This study examined the effects of ZnONP incorporation on nylon filament properties, with the following key findings: (1) both neat nylon and the nanocomposites exhibited strain rate-dependent mechanical behavior. (2) The nanocomposites showed significant improvements in mechanical properties compared to neat nylon, while maintaining similar failure strains. (3) DSC and TGA revealed enhanced thermal stability in the nanocomposites, evidenced by increased decomposition and glass transition temperatures, with no change in melting temperature. (4) A nonlinear constitutive model was developed to quantify the observed strain rate sensitivity, with simulations suggesting a decrease in the viscosity coefficient (η) with increasing strain rate. Nanoparticle incorporation appeared to increase the nylon matrix viscosity, potentially impacting high-strain-rate behavior. The 2% ZnONP sample exhibited higher density and fewer free spaces compared to the 1% ZnONP sample, which showed relative weakness and random masses potentially due to weak Van der Waals forces between the matrix and NPs. Characterization confirmed the smooth, spherical form and hexagonal wurtzite structure of the ZnONPs. Finally, the 2% ZnONP sample demonstrated the highest dielectric constant, a 65% increase compared to neat nylon.

Application of nanocomposites in real-world engineering problems

Nylon 6 nanocomposites offer a range of potential applications across various industries due to their enhanced properties. In the automotive sector, their light weight (resulting from increased strength and stiffness allowing for thinner parts) contributes to improved fuel efficiency and reduced emissions. Enhanced durability and noise reduction are additional benefits. Aerospace applications benefit from the reduced weight of nylon 6 nanocomposites, crucial for fuel-efficient aircraft components, and their improved performance due to high strength-to-weight ratio and fatigue resistance. Electronics and electrical applications can leverage the improved insulation, heat dissipation, and flame retardancy offered by these materials. Packaging applications can benefit from enhanced barrier properties, extending shelf life, and increased strength and durability, reducing damage during transport. Finally, in the biomedical field, with appropriate surface modifications, nylon 6 nanocomposites offer biocompatibility and enhanced mechanical properties suitable for applications like orthopedic implants, drug delivery systems, and tissue engineering scaffolds. These examples highlight the potential of nylon 6 nanocomposites to address real-world engineering challenges, and continued research promises further innovative applications with significant societal and economic impact.

REFERENCES

[1]. Wang Shuyu, Duan Shuaiyang, Yang Tianyu, Zhonghai He, Xia Zhichao, Zhao Yuliang, A self-powered strain sensor utilizing hydrogel-

nanosheet composites, Zn foil, and silver-coated nylon, Sensors and Actuators A: Physical, Volume 364, 1 December 2023, 114824.

[2]. Rana Kiran, Jassal Manjeet, Agrawal Ashwini K., Solution spun electrically conductive nylon 6/poly(pyrrole) nanotubes-based composite fibers, Synthetic Metals, Volume 303, April 2024, 117550.

[3]. Gavande Vishal, Nagappan Saravanan, Seo Bongkuk, Cho Young-Seok, Lee Won-Ki, Transparent nylon 6 nanofibers-reinforced epoxy matrix composites with superior mechanical and thermal properties, Polymer Testing, Volume 122, May 2023, 108002.

[4]. Yilmaz Musa, Ekrem Mürsel, Avci Ahmet, Impact resistance of composite to aluminum single lap joints reinforced with graphene doped nylon 6.6 nanofibers, International Journal of Adhesion and Adhesives, Volume 128, January 2024, 103565.

[5]. Atir Salman, S. Ali Hasan, Nimra S.Sadia, Zhao Tingkai, Shakir HM Fayzan, Rehan ZA, Achieving enhanced EMI shielding with novel non-woven fabric using nylon fiber coated with polyaniline via in situ polymerization, Synthetic Metals, Volume 293, March 2023, 117250.

[6]. Mishra Kushal, Singh Aparna, Effect of graphene nano-platelets coating on carbon fibers on the hygrothermal ageing driven degradation of carbon-fiber epoxy laminates, Composites Part B: Engineering, Volume 269, 15 January 2024, 111106.

[7]. Zeynali Yasaman, Niroumand Hamed, Ziaie Moayed Reza, Stabilizing cohesive soils with Micro- and Nano- fly ash as Eco-friendly Materials: An experimental study, Construction and Building Materials, Volume 399, 5 October 2023, 132490.

[8]. Hazarika Ankita, Deka Biplab K., Park Hyunmin, Hwang Yun Jae,Jaiswal Anand P., Park Young-Bin, Park Hyung Wook, Hierarchically designed 3-D printed porous nylon fabric-based personal thermoregulatory for radiative and directional wick-evaporative cooling, Chemical Engineering Journal, Volume 471, 1 September 2023, 144536.

[9]. Liu Kan, Su Yishi, Wang Xiaozhen, Cai Yunpeng, Cao He, Ouyang Qiubao, Zhang Di, Achieving simultaneous enhancement of strength and ductility in Al matrix composites by employing the synergetic strengthening effect of micro- and nano-SiCps, Composites Part B: Engineering, Volume 248, 1 January 2023, 110350.

[10]. Liu Yan-Jun, Yang He-Yun, Hu Yan-Yun, Li Zheng-Hao, Yin Hao, He Yun-Tian, Zhong Keng-Qiang, Yuan Li, Zheng Xing, Sheng Guo-Ping, Face mask derived micro(nano)plastics and organic compounds potentially induce threat to aquatic ecosystem security revealed by toxicogenomics-based assay, Water Research, Volume 242, 15 August 2023, 120251.

[11]. Lin Huiping, Kehinde Olonisakin, Lin Chengwei, Fei Mingen, Li Ran, Zhang Xinxiang, Yang Wenbin, Li Jian, Mechanically strong micro-nano fibrillated cellulose paper with improved barrier and water-resistant properties for replacing plastic, International Journal of Biological Macromolecules, Volume 263, Part 1, April 2024, 130102.

[12]. Dehghanian Zahra, Lajayer Behnam Asgari, Atigh Zahra Biglari Quchan, Nayeri Shahnoush, Ahmadabadi Mohammad, Taghipour Leila, Senapathi Venkatramanan, Astatkie Tess, Price G.W., Micro (nano) plastics uptake, toxicity and detoxification in plants: Challenges and prospects, Ecotoxicology and Environmental Safety, Volume 268, December 2023, 115676.

[13]. Cui Qian, Wang Feilong, Wang Xiaoxiao, Chen Tao, Guo Xuetao, Environmental toxicity and ecological effects of micro(nano)plastics: A huge challenge posed by biodegradability, TrAC Trends in Analytical Chemistry, Volume 164, July 2023, 117092.

[14]. Zhao Yonghuan, Meng Yang, Yu Pengxiang, Hu Xiaoxiao, Su Juanjuan, Han Jian, Modified reduced graphene oxide-LDH/WPU nanohybrid coated nylon 6 fabrics for durable photothermal conversion performance, Applied Surface Science, Volume 622, 15 June 2023, 156900.

[15]. Le Van-Giang, Nguyen Minh-Ky, Nguyen Hoang-Lam, Lin Chitsan, Hadi Mohammed, Hung Nguyen Tri Quang, Hoang Hong-Giang, Nguyen Khoi Nghia, Tran Huu-Tuan, Hou Deyi, Zhang Tao, Bolan Nanthi S., A comprehensive review of micro- and nano-plastics in the atmosphere: Occurrence, fate, toxicity, and strategies for risk reduction, Science of The Total Environment, Volume 904, 15 December 2023, 166649.

J. Nanoanalysis., 11(1): 668-674, Winter 2024

The application of Spirulina platensis based green synthesized silver nanoparticles demonstrated potent anti Shigella flexneri effects by specifically targeting pathogenic gene expressions

Sahar Karami,[1] Zahra Heidary,[1] Sepideh Khaleghi,[2] Sarvenaz Falsafi,[3] Mohammad karim Rahimi[4], Shadi Hajrasouliha[5,*]

[1] *Department of Biology, School of Basic Sciences, Science and Research Branch, Islamic Azad University, Tehran, Iran*
[2] *Department of Biotechnology, Faculty of Advanced Science and Technology, Tehran Medical Sciences, Islamic Azad University, Tehran, Iran*
[3] *Department of Microbiology, Faculty of Advenced Science and Technology, Tehran Medical Sciences, Islamic Azad University, Tehran, Iran.*
[4] *Department of Microbiology, Faculty of Medicine, Tehran Medical Sciences, Islamic Azad University, Tehran, Iran*
[5,*] *Herbal Pharmacology Research Center, Tehran Medical Sciences, Islamic Azad University, Tehran, Iran*

ABSTRACT

ARTICLE INFO

Article History:

Received 2024-09-11
Accepted 2025-09-13
Published 2024-02-15

Keywords:

Gene expression,
Nanoparticles,
Shigella,
Silver.

Background: The emergence of antibiotic-resistant strains of *Shigella flexneri*, an important cause of shigellosis, has led to extensive research to find alternative treatment approaches. Therefore, in the current study, the antibacterial effects of the green synthesized silver nanoparticles (AgNPs) using *Spirulina platensis* on *S. flexneri* and also the expression of pathogenic genes *ipaB*, *ipaD*, *ipaH* and *qnrS* were studied.

Methods: After the synthesis of AgNPs using *S. platensis*, its antibacterial effects on *S. flexneri* were studied using microdilution method with 96-well plate. Also, in order to determine the minimum bactericidal concentration (MBC), 10 µL of the contents of the MIC well and so on was swapped on nutrient agar medium. After RNA extraction, cDNA synthesis and primer design, expression levels of *ipaB*, *ipaD*, *ipaH* and *qnrS* genes were studied using Real-Time PCR technique. Data analysis was done in GraphPad Prism V.8 software.

Results: The MIC of the green synthesized AgNPs was measured as 0.0625 µg/ml and its MBC was 0.125 µg/ml. The results of RT-PCR analysis indicated a significant decrease in the expression levels of pathogenic genes *ipaB*, *ipaD*, *ipaH* and *qnrS* in AgNPs-treated *S. flexneri*.

Conclusion: The green synthesized AgNPs using *Spirulina platensis* has strong antibacterial effects on *S. flexneri* and the action mechanism was attributed to the downregulations of *ipaB*, *ipaD*, *ipaH* and *qnrS* genes. The in vivo and clinical studied are needed.

How to cite this article
Karami S., Heidary Z., Khaleghi S., Falsafi S., Rahimi M. K., Hajrasouliha Sh.,The application of Spirulina platensis based green synthesized silver nanoparticles demonstrated potent anti Shigella flexneri effects by specifically targeting pathogenic gene expressions. J. Nanoanalysis., 2024; 11(1): 668-674.

*Corresponding Author Email: *Sh.Hajrasouliha@iautmu.ac.ir*

INTRODUCTION

Infectious diseases are of the most important and common diseases in the world, which cause many problems to the health system of most countries, especially developing countries (1). One of these kinds of diseases is shigellosis, which is caused by *Shigella* sp. bacteria, especially *Shigella flexneri* (2*)*, and is an important cause of bacterial gastroenteritis and dysentery (3). 12.5% of deaths caused by diarrheal diseases are due to *Shigella* and its mortality rate is higher in children under 5 years of age (4). Clinical manifestations include diarrhea, dysentery, high fever, abdominal cramps, myalgia, and rectal tenesmus or spasm (5).

The ability of *S. flexneri* to penetrate into epithelial cells is due to the presence of its large invasive plasmid whose genes are responsible for the coding of invasive proteins (IPs) (6). These invasive proteins include *ipaA*, *ipaB*, *ipaC*, *ipaD*, and *ipaH* (7). After the bacteria contact the host cells, IpaB and IpaC inject inosines into the cytoplasm of the cell by creating a pore on the plasma membrane (8). IpaD provides bacteria with the ability to phagocytize (9), and IpaA causes depolymerization of F-actin by binding to vinculin (10). On the other hand, ipaH protects *Shigella* from macrophages (11), which can move to the nucleus of the host cell and stimulate the secretion of *Shigella* proteins (12). One of the acquired genes involved in creating relative resistance to quinolones in *Shigella* is *qnrS* which protects bacterial DNA by inhibiting the binding of quinolones to DNA gyrase and topoisomerase 4 (13).

The administration of water and electrolytes as well as prescribing antibiotics such as ampicillin, tetracycline, erythromycin, trimethoprim/sulfamethoxazole, and in severe cases ciprofloxacin are among the treatment approaches (14). However, the emergence of antibiotic-resistant strains of *S. flexneri* has reduced the effectiveness of treatments (15, 16). Therefore, there is a need for new approaches to the treatment of shigellosis.

Nanoparticles (NPs) have many applications in medicine due to their unique physicochemical and biological properties (17). The synthesis of NPs using chemical approaches is associated with side effects and environmental harms, which limit their application (18). To overcome these problems, NPs green synthesis methods using plant extracts have been introduced, which are cost-effective and environmentally friendly (18). One of the widely used NPs is silver nanoparticles (AgNPs), whose anticancer and antimicrobial properties have been studied in many studies (19-21). AgNPs have antibacterial properties against gram-positive and gram-negative bacteria, and this compound has shown antimicrobial effects against antibiotic-resistant bacteria (22). For example, AgNPs have shown antibacterial effects on *E. coli*, *S. Typhimurium*, *S. aureus* and *B. subtilis*, and it seems that the smaller size of this nanoparticle is associated with increased antimicrobial activity (23).

Therefore, the current research was aimed to investigate the antibacterial effects of green synthesized silver nanoparticles on *S. flexneri* and evaluate the pathogenic ipaA, ipaD, ipaH and qnrS genes' expressions.

EXPERIMENTAL

AgNPs synthesis

Ethanol extract of spirulina algae (Spirulife, Esfahan, Iran) was used for the synthesis of AgNPs. For this purpose, 20 g of dry spirulina powder was dissolved in 200 ml of 96% ethanol and placed on a shaker at 140 rpm for 35 min. Then, with Whatman filter paper, the solution was filtered and the obtained extract was centrifuged at 13000 rpm for 20 minutes. 340 mg of $AgNO_3$ (Merck, Germany) was mixed in 100 ml of distilled water and 100 ml of spirulina extract and placed on a shaker for 24 hours. After observing the color change of the solution and ensuring the complete reduction of silver ions to silver nanoparticles, the sediment was washed three times using a centrifuge at 13000 rpm for 20 minutes. Finally, the final sediment was collected after drying at 40°C for 120 min.

Shigella flexneri culture

S. flexneri (ATCC 12022) was obtained from the Microbiology Department of Pasteur Institute of Iran and cultured in nutrient broth at 32°C for 24 hours. Then, the bacteria were separated by centrifugation at 4000 rpm and the McFarland method was used to determine the microbial population. The initial turbidity of the microbial suspension was determined using 0.5 McFarland solution. In order to prepare a microbial population equal to 1.5×10^6 bacteria/mL, physiological serum was used .

Minimum inhibition and bactericidal concentration

Microdilution method based on CLSI 2017 standard was used to measure minimum inhibition concentration (MIC) of $AgNO_3$-NPs (19). Briefly, successive dilutions of $AgNO_3$-NPs in the concentration range of 0.063 to 32 mg/ml were poured into the wells of 96-well plates, and then 1 mL of nutrient broth was added to it along with 1 mL of microbial inoculum (1.5×10^6 bacteria). The plates were incubated for 24 hours at 37°C. The well containing nutrient broth culture medium with bacteria and the well containing culture medium without bacteria were considered as positive and negative control, respectively.

To determine the minimum bactericidal concentration (MBC), 10 µL from the last well that did not show any bacterial growth were taken and cultured in MH agar medium. The plates were incubated for 24 hours at 37°C.

Gene expression

RNA was extracted using the RNX-PLUS method. Briefly, bacteria were trypsinized and separated by centrifugation for 48 hours after treatment with AgNPs. Then 500 µL of RNX-PLUS solution was added to the samples. Then, 200 µL of chloroform was added and incubated at 4 °C for 5 min and centrifuged at 12000 rpm for 15 min. cDNA synthesis was performed using a kit (BioFact, South Korea) according to the manufacturer's instructions.

Primer design was done using NCBI database and Primer 3 software. The sequences of the primers of *ipaD*, *ipaB*, *ipaH* and *qnrS* genes are given in Table 1. The expression levels of the studied genes were determined by RT-PCR technique using the Cyber green method (Q Rotor Gene, Qiagen). 16s rRNA gene was used as control. The reaction mixture included 7 µL of master mix, 0.5 µL of forward and reverse primers, 5 µL of deionized water, and 1 µL of cDNA. The time-temperature schedule of the RT-PCR machine is given in Table 2.

Statistical analysis

$2^{-\Delta\Delta Ct}$ method was used to analyze the expression levels of *ipaD*, *ipaB*, *ipaH* and *qnrS* genes. Also, the gene expressions between groups were analyzed by unpaired Pearson T-Test at probability levels of $P<0.05$.

RESULTS AND DISCUSSIONS

Results

MIC and MBC

Microdilution method was used to determine the AgNPs MIC against *S. flexneri* and the results showed that the growth of bacteria decreased with increasing concentration of AgNPs and no bacterial growth was observed at the concentration of 0.0625 μg/ml. Therefore, this concentration was considered as the MIC of AgNPs. Next, 10 μL of the wells containing 0.0312 μg/ml AgNPs and so on were removed and cultured in the nutrient agar medium, and after 48 hours, it was observed that the bacteria did not grow in the medium containing 0.125 μg/ml AgNPs and so on. Therefore, the MBC of AgNPs against *S. flexneri* was considered 0.125 μg/ml.

Table 1. The sequences of primers used for measuring the expression levels of *ipaD*, *ipaB*, *ipaH* and *qnrS* genes by RT-PCR technique

Gens	Sequence [5'-3']	GC%	TM (°C)
ipaB	Forward: ACGACTGCTGCAACTAGGAC Reverse: GGAACAAGCCCTGAATCCGA	55	60
ipaD	Forward: ACGGAGTTTCCGTCGTTACC Reverse: GAAGCCGAGCTTGATGGAGA	55	60
ipaH	Forward: ACGACTGCTGCAACTAGGAC Reverse: TGAGATGCTGGAGAATGAGTACC	50	59.6
qnrS	Forward: TCACACATATCGGCACCACA Reverse: TCGCAAGTTGGCATTGTTGG	55	59.97

Table 2. The time- temperature schedule of the RT-PCR

Steps	Temp. (°C)	Time
Denaturation & enzyme activation	95	10 min
Step 1: Denaturation	95	15s
Step 2: Annealing	59	25s
Step 3: Extension & Floresence acquiring	72	30s
Melting curve analysis	65-95	1°C each step

Gene expression analysis

ipaB & ipaH

Both *ipaB* (P=0.006) and *ipaH* (P=0.004) genes expressions in AgNPs-treated *S. flexneri* were decreased significantly compared to the control. The expression level of *ipaH* in control was measured 1.18±0.3, however, in AgNPs-treated *S. flexneri* was measured 0.33±0.08, indicating downregulation of *ipaH* in AgNPs-treated *S. flexneri*. The same was seen for *ipaB* gene, and the expression level was decreased ~3 times compared untreated *S. flexneri* (Control).

ipaD & qnrS

Significant differences in terms of *ipaD* (P=0.005) and *qnrS* (P=0005) gene expression were observed in *S. flexneri* treated with MIC concentration of AgNPs compared to untreated bacteria (Figure 2). The expressions of both genes decreased in AgNPs-treated *S. flexneri*, which indicates the effect of AgNPs on reducing the expression of *S. flexneri* pathogenic genes.

Discussion

The results of the present study showed that green synthesized silver nanoparticles have antibacterial effects against *S. flexneri* and the mechanism of antibacterial effects was attributed to the downregulation of pathogenic genes *ipaB*, *ipaD*, *ipaH* and *qnrS*.

We used *Spirulina platensis* to synthesize green AgNPs. Green synthesis of nanoparticles can reduce its side effects on organisms and the environment (24). This algae shows good anti-inflammatory and antioxidant properties due to having various beneficial compounds such as vitamins and amino acids (25) and is widely used in the synthesis of most metal nanoparticles (26, 27). For example, Gunasundari et al. (2017) used ultrasonic-assisted *S. platensis* to synthesize metal nanoparticles including Zn, Fe, and Ag and reported antimicrobial effects on Gram-positive and negative bacteria as well as *Aspergillus niger* (28). Also, Mahdieh et al. (2012) used this algae for the synthesis of crystallized silver nanoparticles (SNPs) (29). Therefore, the *S. platensis* has great potential in the green synthesis of metal nanoparticles due to convenient to handle, low toxicity and reduction of harmful effects on the environment (30), and the results of the present study confirm that this algae can be used in the green synthesis of AgNPs.

The synthesized green AgNPs showed antibacterial effects on *S. flexneri*, which showed the potential of its application in the treatment of diseases caused by this pathogen. Its MIC was calculated as 0.0625 µg/ml, which is lower than other studies investigating the anti-*Shigella* effects of silver nanoparticles. This difference can be attributed to the nanoparticle synthesis method and bacterial species. For example, Angamuthu et al. (2023) estimated the MIC of *M. indica* silver nanoparticles on the multi-drug-resistant strain *S. flexneri* to be 20 µg/ml (31), which is much higher than the present study. This difference can be attributed to the different strain and the method for AgNPs synthesis. In the study of Bagherzade et al. (2017), the MIC of green AgNPs synthesized by the aqueous extract of saffron plant on pathogenic bacteria was reported to be 250 µg/mL, which shows a very high value (32). It seems that synthesis factors, bacterial strains and toxicity criteria are important factors in this difference. In another study, Muthukrishnan et al. (2015) reported the highest inhibitory concentration of pathogenic bacteria by AgNPs synthesized with *Ceropegia thwaitesii* as 100 µg/mL (33). They used the disk diffusion method to investigate the antimicrobial effects of AgNPs, while in the present study, the microdilution method was used, which can explain the reason for this difference in the antibacterial concentration of this nanoparticle.

In the present study, it was observed that green synthesized AgNPs using spirulina caused changes in the expression of pathogenic genes such as *ipaB*, *ipaD*, *ipaH* and *qnrS* in *S. flexneri* bacteria and reduced their expressions. Therefore, in this research, it was found that the anti-*Shigella* mechanism of AgNPs is the effect on the expression of pathogenic genes. These genes play an important role in the penetration of bacteria to the epithelial cells and also protect the DNA against destructive factors (12). Therefore, the synthesized green AgNPs increase the sensitivity of Shigella flexneri to protective agents by reducing the expressions of *ipaB*, *ipaD*, *ipaH* and *qnrS* genes, thus exerting anti-*Shigella* effects.

CONCLUSION

The green synthesized AgNPs using *Spirulina platensis* has strong antibacterial effects on *S. flexneri* and the action mechanism was attributed to the downregulations of *ipaB*, *ipaD*, *ipaH* and *qnrS* genes. The *in vivo* and clinical studied are needed.

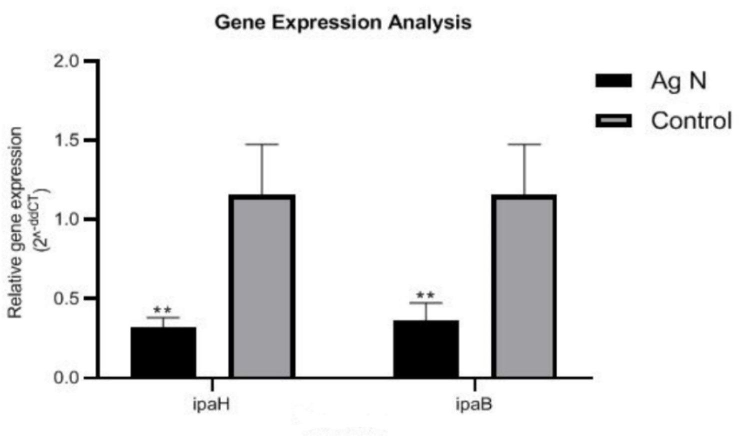

Figure 1. *ipaB* and *ipaH* genes expressions in AgNPs treated and untreated (control) *S. flexneri*. ** shows significant differences at probability level of P<0.01.

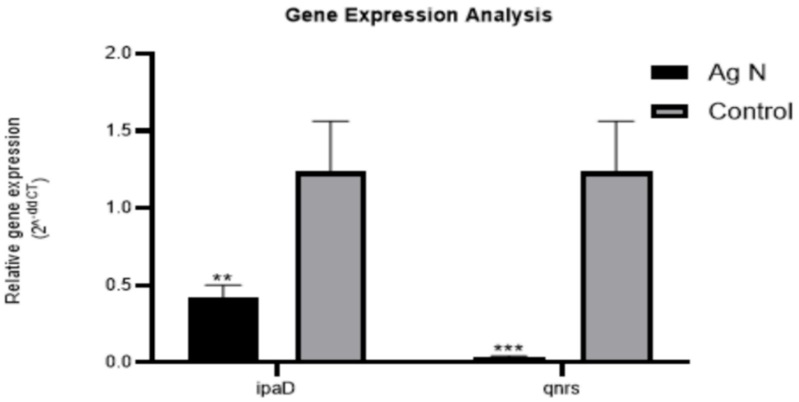

Figure 2. *ipaD* and *qnrS* genes expressions in AgNPs treated and untreated (control) *S. flexneri*. ** and *** show significant differences at probability level of P<0.01 and P<0.001, respectively.

REFERENCES

1. Barreto ML, Teixeira MG, Carmo EH. Infectious diseases epidemiology. Journal of Epidemiology & Community Health. 2006;60(3):192-5.

2. Kotloff KL, Riddle MS, Platts-Mills JA, Pavlinac P, Zaidi AK. Shigellosis. The Lancet. 2018;391(10122):801-12.

3. Barrett J, Fhogartaigh CN. Bacterial gastroenteritis. Medicine. 2017;45(11):683-9.

4. Feigin VL, Abajobir AA, Abate KH, Abd-Allah F, Abdulle AM, Abera SF, et al. Global, regional, and national burden of neurological disorders during 1990–2015: a systematic analysis for the Global Burden of Disease Study 2015. The Lancet Neurology. 2017;16(11):877-97.

5. Von Seidlein L, Kim DR, Ali M, Lee H, Wang X, Thiem VD, et al. A multicentre study of Shigella diarrhoea in six Asian countries: disease burden, clinical manifestations, and microbiology. PLoS medicine. 2006;3(9):e353.

6. Watarai M, Funato S, Sasakawa C. Interaction of Ipa proteins of Shigella flexneri with alpha5beta1

integrin promotes entry of the bacteria into mammalian cells. The Journal of experimental medicine. 1996;183(3):991-9.

7. Buysse JM, Stover CK, Oaks EV, Venkatesan M, Kopecko DJ. Molecular cloning of invasion plasmid antigen (ipa) genes from Shigella flexneri: analysis of ipa gene products and genetic mapping. Journal of bacteriology. 1987;169(6):2561-9.

8. Kotloff KL, Pasetti MF, Barry EM, Nataro JP, Wasserman SS, Sztein MB, et al. Deletion in the Shigella enterotoxin genes further attenuates Shigella flexneri 2a bearing guanine auxotrophy in a phase 1 trial of CVD 1204 and CVD 1208. The Journal of infectious diseases. 2004;190(10):1745-54.

9. Dickenson NE, Zhang L, Epler CR, Adam PR, Picking WL, Picking WD. Conformational changes in IpaD from Shigella flexneri upon binding bile salts provide insight into the second step of type III secretion. Biochemistry. 2011;50(2):172-80.

10. Bourdet-Sicard R, Rüdiger M, Jockusch BM, Gounon P, Sansonetti PJ, Van Nhieu GT. Binding of the Shigella protein IpaA to vinculin induces F-actin depolymerization. The EMBO journal. 1999;18(21):5853-62.

11. Fernandez-Prada CM, Hoover DL, Tall BD, Hartman AB, Kopelowitz J, Venkatesan MM. Shigella flexneri IpaH7. 8 facilitates escape of virulent bacteria from the endocytic vacuoles of mouse and human macrophages. Infection and immunity. 2000;68(6):3608-19.

12. Sethuvel DPM, Perumalla S, Anandan S, Michael JS, Ragupathi NKD, Gajendran R, et al. Antimicrobial resistance, virulence & plasmid profiles among clinical isolates of Shigella serogroups. Indian J Med Res. 2019;149(2):247-56.

13. Pu X-Y, Pan J-C, Wang H-Q, Zhang W, Huang Z-C, Gu Y-M. Characterization of fluoroquinolone-resistant Shigella flexneri in Hangzhou area of China. Journal of antimicrobial chemotherapy. 2009;63(5):917-20.

14. Williams PCM, Berkley JA. Guidelines for the treatment of dysentery (shigellosis): a systematic review of the evidence. Paediatrics and International Child Health. 2018;38(sup1):S50-S65.

15. Shen H, Chen J, Xu Y, Lai Z, Zhang J, Yang H, et al. An outbreak of shigellosis in a Children Welfare Institute caused by a multiple-antibiotic-resistant strain of Shigella flexneri 2a. Journal of Infection and Public Health. 2017;10(6):814-8.

16. Puzari M, Sharma M, Chetia P. Emergence of antibiotic resistant Shigella species: A matter of concern. Journal of Infection and Public Health. 2018;11(4):451-4.

17. Zhang L, Gu FX, Chan JM, Wang AZ, Langer RS, Farokhzad OC. Nanoparticles in Medicine: Therapeutic Applications and Developments. Clinical Pharmacology & Therapeutics. 2008;83(5):761-9.

18. Kharissova OV, Dias HVR, Kharisov BI, Pérez BO, Pérez VMJ. The greener synthesis of nanoparticles. Trends in Biotechnology. 2013;31(4):240-8.

19. Abass Sofi M, Sunitha S, Ashaq Sofi M, Khadheer Pasha SK, Choi D. An overview of antimicrobial and anticancer potential of silver nanoparticles. Journal of King Saud University - Science. 2022;34(2):101791.

20. Hembram KC, Kumar R, Kandha L, Parhi PK, Kundu CN, Bindhani BK. Therapeutic prospective of plant-induced silver nanoparticles: application as antimicrobial and anticancer agent. Artificial Cells, Nanomedicine, and Biotechnology. 2018;46(sup3):38-51.

21. Ghramh HA, Ibrahim EH, Kilany M. Study of anticancer, antimicrobial, immunomodulatory, and

silver nanoparticles production by Sidr honey from three different sources. Food science & nutrition. 2020;8(1):445-55.

22. Rai MK, Deshmukh SD, Ingle AP, Gade AK. Silver nanoparticles: the powerful nanoweapon against multidrug-resistant bacteria. Journal of Applied Microbiology. 2012;112(5):841-52.

23. Cheon JY, Kim SJ, Rhee YH, Kwon OH, Park WH. Shape-dependent antimicrobial activities of silver nanoparticles. International Journal of Nanomedicine. 2019;14:2773-80.

24. Gour A, Jain NK. Advances in green synthesis of nanoparticles. Artificial cells, nanomedicine, and biotechnology. 2019;47(1):844-51.

25. Wu Q, Liu L, Miron A, Klímová B, Wan D, Kuča K. The antioxidant, immunomodulatory, and anti-inflammatory activities of Spirulina: an overview. Archives of Toxicology. 2016;90(8):1817-40.

26. Kalabegishvili T, Kirkesali E, Rcheulishvili A. Synthesis of gold nanoparticles by blue-green algae Spirulina platensis. Frank Lab. of Neutron Physics; 2012.

27. Muthusamy G, Thangasamy S, Raja M, Chinnappan S, Kandasamy S. Biosynthesis of silver nanoparticles from Spirulina microalgae and its antibacterial activity. Environmental Science and Pollution Research. 2017;24(23):19459-64.

28. Gunasundari E, Senthil Kumar P, Christopher FC, Arumugam T, Saravanan A. Green synthesis of metal nanoparticles loaded ultrasonic-assisted Spirulina platensis using algal extract and their antimicrobial activity: IET Nanobiotechnol. 2017 Jul 26;11(6):754-8. doi: 10.1049/iet-nbt.2016.0223. eCollection 2017 Sep.

29. Mahdieh M, Zolanvari A, Azimee AS, Mahdieh M. Green biosynthesis of silver nanoparticles by Spirulina platensis. Scientia Iranica. 2012;19(3):926-9.

30. Mukherjee A, Sarkar D, Sasmal S. A Review of Green Synthesis of Metal Nanoparticles Using Algae. Frontiers in Microbiology. 2021;12.

31. Angamuthu S, Thangaswamy S, Raju A, Husain FM, Ahmed B, Al-Shabib NA, et al. Biogenic Preparation and Characterization of Silver Nanoparticles from Seed Kernel of Mangifera indica and Their Antibacterial Potential against Shigella spp. Molecules [Internet]. 2023; 28(6).

32. Bagherzade G, Tavakoli MM, Namaei MH. Green synthesis of silver nanoparticles using aqueous extract of saffron (Crocus sativus L.) wastages and its antibacterial activity against six bacteria. Asian Pacific Journal of Tropical Biomedicine. 2017;7(3):227-33.

33. Muthukrishnan S, Bhakya S, Senthil Kumar T, Rao MV. Biosynthesis, characterization and antibacterial effect of plant-mediated silver nanoparticles using Ceropegia thwaitesii – An endemic species. Industrial Crops and Products. 2015;63:119-24.